Gd-PSMA Neutron Capture Therapy

A computational feasibility and method development study

by

D. B. Feilzer

to obtain the degree of Master of Science
at the Delft University of Technology,
to be defended publicly on Monday September 24th, 2018 at 10:00 AM.

Student number:	4251296	
Project duration:	September 1, 2017 – Augustus 29, 2018	
Thesis committee:	dr. Z. Perkó,	TU Delft, supervisor
	dr. D. Schaart,	TU Delft, 3ME
	prof.dr.ir. J. L. Kloosterman,	TU Delft, RS&T
	prof.dr.ir. M. van Gijzen,	TU Delft, EWI
	dr. W.V. Vogel	NKI-AvL

Preface

After a course at the Reactor Institute Delft I always thought it was an interesting place. Having done my masters thesis here has been so as well.

This thesis caters an audience having some experience in physics, linear algebra and a basic knowledge of radiation therapy. I hope the thesis reads as a linear story, although not many ideas like to be squeezed into one dimension like that. Some topics that I liked most in retrospect were the neutron filtering for its mathematical cleanliness and the calculated dose boost obtained when properly accounting for the granularity of tumour tissue in chemically targeted radiotherapy.

Thank you Zoltán for the interesting talks and guidance, and the ink factory for providing Zoltán with plenty of red ink.

D. B. Feilzer
Delft, August 2018

Contents

1

Introduction

1.1. Prostate cancer

The prostate gland is a vital organ in males, where it plays an important part in the reproductive system. The prostate is located under the bladder, close to the rectum, and the urethra tube (transporting urine and semen) passes through its centre. With age, the prostate grows in size. With growth, cell-division takes place as it does everywhere in the body. Errors in this division can set this process out of control. Such out of control division can yield a large cluster of malignant cells called a tumour.

According to the American Cancer Society [3], prostate cancer is the most prevalent cancer in men after skin cancer. Most of these prostate tumours are adenocarcinomas originating from malignant prostate gland cells. Other types also exist but are rare. If such cells reach blood vessels or the lymph system they can spread out. Cells transported in the lymph system often accumulate in lymph nodes. This spread to other parts of the body could result in metastases. Subcategories exists for staging these tumours that help improving statistical reporting on patient outcomes and choosing the best treatment.

1.2. Conventional treatments for prostate cancer

To treat prostate cancer, many treatments are available depending on the size of the tumour, the number of infected lymph nodes and the occurrence of other metastasis.

When no spreading of the primary tumour is suspected, surgical treatment is an option. The most common surgical treatment is radical prostatectomy. Here the prostate, including a margin, is completely removed surgically [3]. This treatment could be curative although in many cases it is not [26]. If during the surgery metastisation to the lymph nodes is seen, the surgery is often stopped since the expected gain at that point no longer outweighs the side effects of the operation.

Radiotherapy in the form of external beam therapy or brachytherapy can also be used in treating such primary tumours with comparable cure rates to prostatectomy [3, 26]. External beam radiation therapy can also be used as additional treatment after prostatectomy in a precautionary manner or after the first evidence of recurrence [3, 6]. When after a primary treatment such additional treatment is performed, this additional treatment is called *adjuvant*. Radiation therapy can also be employed for non-curative palliative treatment in late stages of prostate tumours to improve quality of life.

If neither surgery nor radiotherapy can be used in a curative manner, hormone therapy is an option to slow down growth or even shrink the tumour. It can also be applied after radiation therapy, in a precautionary manner as an adjuvant treatment or later after first evidence of recurrence [3, 6]. It is still unknown if delaying these treatments till the first signs of recurrence has any negative effect on the outcome or not [9].

A promising newer type of radiotherapy is radioligand therapy. In radioligand therapy, radioisotopes are either injected locally or intravenously. When this is done intravenously, the radioisotopes are most often attached to molecules which have a high uptake from the bloodstream in specific tissue types, preferably only in tumorous tissue. Whenever the placement of these isotopes is aided by such molecules we speak of *chemical targeting*. In chemical targeting a *tumour-selective* uptake is desired where the concentration

associated with the tumour cells relative to that in healthy cells is preferably high. The advantage of chemical targeting is that it is more robust against movement of the patient and other geometrical errors compared to external beam radiotherapy. It is also less dependent on knowing the location of the tumour cells and has the potential of sparing healthy tissues almost perfectly. However, it is heavily dependent on the degree of the drug's selectivity towards the tumour cells and the time window in which that selectivity is maintained.

Any treatment or combinations thereof are tailored to the specifics of the patient and the tumour stage. Accordingly, many more treatment combinations are possible than listed here. There is, however, room for improvement in the curative treatments available for prostate cancer.

1.3. Neutron capture therapy

Neutron Capture Therapy (NCT) combines radioligand therapy and external neutron beam therapy. In NCT the radioactive isotope - that would be used in radioligand therapy - is replaced with an isotope that has a high affinity for capturing neutrons and consequently releasing the reaction energy locally, and an external neutron beam delivers the required neutron flux at the position of the target volume.

Like in radioligand therapy, the neutron capture isotope is either locally injected at the target volume [20] or chemically targeted to the tumour using a tumour-selective compound [4]. In addition to the aforementioned benefits of chemically targeted radiotherapy, the irradiation in chemically targeted NCT due to the neutron capture products is spatially confined to both the neutron irradiated area and the neutron capture agent containing cells (and potentially their neighbouring cells). Thus, any undesired build up of the isotope in for example the kidneys or liver does not cause toxicity as long as they don't experience a significant neutron flux.

An additional benefit to NCT is that the irradiation from the external neutron beam can be timed to coincide with the optimal biological distribution of the chemical target agent. This better timing has the potential to enhance the sparing of organs compared to radioligand therapy where irradiation takes place outside this optimal window as it starts right from the injection time and lasts for a few effective half-lives.

1.4. Neutron interactions and dose deposition in tissue

To deliver the necessary neutrons to the tumour for NCT, these neutrons first need to travel through the body. Therefore, understanding all the reactions that these neutrons undergo in the body is important in the further development of NCT.

In nuclear reactions with neutrons, energy is released. The total amount of energy that is released in such a reaction is called the *Q-value*. A part of this energy is carried by short range charged particles. These short range particles deposit their energy close to the reaction site and cause biological damage. This locally deposited energy from charged particles is called *kerma*. The rest of the energy can be carried away further by for example photons. The energy deposited by these longer range particles is spread out over a much larger volume and could even leak out of the patient.

The affinity of neutron capture agents to capture neutrons is often higher for lower energy (thermal) neutrons. Consequently, this requires the neutrons arriving at the tumour to have a low energy as we want to maximise the number of neutron captures in the tumour. However, neutron capture is not confined exclusively to the tumour.

Outside the tumour neutron capture is also possible in isotopes such as nitrogen. The $^{14}\text{N}(\text{n},\text{p})^{14}\text{C}$ neutron capture reaction contributes 96% of the thermal neutron kerma in healthy tissue with its 620 keV short range protons [2]. Although these isotopes have less affinity for capturing neutrons than the neutron capture agent, their concentration is higher. The neutron capture reactions outside the tumour cause unwanted tissue damage and cause the number of thermal neutrons to diminish over the path to the deep seated prostate tumour.

To partially overcome this, higher energy (epi-thermal / fast) neutrons are used to irradiate the patient. As neutrons travel through the body, they are slowed down making these unwanted neutron captures less likely until deeper in the body and more likely after slowing down. Consequently, this yields less neutron captures outside the tumour and more neutrons that arrive at the tumour. The process of slowing down neutrons is called moderation and occurs mostly by elastic neutron collisions with light weight nuclei, primarily hydrogen.

Since high energy neutrons are used for irradiation, less neutron captures occur. However, other reactions for these high energetic neutrons are also possible. When a fast neutron collides with hydrogen, the proton can be knocked out, losing its electron. In these reactions, about half the energy of the neutron is transferred to the short range proton [21]. This single reaction is responsible for about 90% of the total kerma in healthy tissue due to neutrons between 600 eV and 3 MeV [2]. Another possible reaction capable of causing damage to healthy tissue is the ^{1}H(n, γ)^{2}H reaction. Although the kerma of this reaction is relatively low, its 2.224 MeV photons are the main contributors to the photon dose in healthy tissue. However, part of these photons could leave the body [2].

The combined effect of these reactions due to a high energetic incident neutron beam is that the thermal neutron flux increases in the first 3 to 4 cm into the body as more high energy neutrons lower in energy [7]. But, since thermal neutrons are more likely to undergo reactions, the thermal flux decreases exponentially from that point on as they travel deeper into the body. Furthermore, due to scattering of thermal neutrons the beam widens substantially, making exact aiming of the neutron beam less important when compared to photon therapy.

1.5. Biophysics of neutron capture in boron

There are several options available for isotopes to be used as neutron capture agent in NCT. The oldest isotope used for this is boron-10 (^{10}B). NCT performed using this isotope is called Boron NCT (BNCT).

In BNCT, the reaction that causes the most damage to the tumour is the ^{10}B(n,α)^{7}Li neutron capture reaction with a high cross section of 3838 barn for capturing thermal neutrons [21, 29]. Directly after neutron capture, the excited ^{11*}B nucleus undergoes nuclear fission producing a 1.47 MeV alpha particle with an extremely short range of 5 μm. The energy of the remaining ^{7}Li recoil nucleus, can either be found in its kinetic energy or part of it can be emitted as a 0.48 MeV gamma particle, which happens 96% of the time, leaving 0.84 MeV for the recoil nucleus itself. The range of this recoil nucleus is 9 μm, which is comparable to that of the alpha particle. When comparing the ranges of the alpha particle and recoil nucleus to a typical cell diameter of 10 μm, it indicates that only cells containing or directly neighbouring the compound will receive dose from these particles created in the neutron capture reaction, thus potentially sparing healthy tissue.

The amount of energy deposited per unit length has influence on the complexity of the biological damage, and consequently the probability of cell death. This amount of energy deposition per unit length is called the *Linear Energy Transfer (LET)*. Due to the short spatial intervals between damaging interactions high LET particles cause more complex damage.

Both the alpha particle and the recoil nucleus have a short range combined with a high energy and consequently a high LET. This gives the neutron capture reaction with ^{10}B the potential of being very effective for causing cell death. However, the inherit difficulty with BNCT is that it highly depends on the availability of tumour specific drugs capable of bringing these short range reaction products within range of the targets.

1.6. Biophysics of neutron capture in gadolinium

An element that is being researched more recently for its potential use in NCT is gadolinium (Gd), where the most promising isotopes are ^{155}Gd and ^{157}Gd. Such treatment is called Gadolinium NCT (GdNCT).

For GdNCT the reaction responsible for tumour damage is the ^{157}Gd(n,γ)^{158*}Gd reaction which has a 66 times higher cross section of 255000 barns [2] relative to the ^{10}B(n,α)^{7}Li reaction in BNCT. After capturing the neutron, the ^{158*}Gd nucleus is left in an exited state. The nucleus releases its extra energy by emitting prompt gammas ranging from 0.079 to 7.88 MeV, averaging at 2.2 MeV [2]. The remainder of the nucleus' excitation energy can be transferred to an orbital electron via electro magnetic interactions. This is most likely for the nearby K-shell electrons as their wave function is more likely to overlap with that of the nucleus.

If the energy transferred to the orbital electron from an exited nucleus exceeds its binding energy, this electron will then be ejected from the atom as an internal conversion electron. In the ^{157}Gd(n,γ)^{158*}Gd reaction, the produced internal conversion electrons have a high LET and on average carry a total energy of 45 to 66 keV per neutron capture [2, 19, 31].

The vacancy left by the emission of the internal conversion electron is filled by electrons from higher energy levels, which are in turn replaced by other higher energy electrons causing a cascade of electrons filling each others vacancies. Each of these electrons emit energy either by emitting characteristic x-rays or by transferring their energy to one of the electrons in a higher electron shell where the binding energy is less.

If the energy transferred to an electron during the filling of an inner-shell vacancy is larger than its binding energy, this electron is emitted from the atom as an Auger electron. For $^{157}Gd(n,\gamma)^{158*}Gd$ cascade of Auger electrons on average carry a total energy of 5 to 9 keV per neutron capture [2, 31]. The total energy released in the form of x-rays lies between 10.7 and 38.4 keV per neutron capture [2, 31].

For smaller geometries the gamma component in GdNCT can leave the body. In larger tumours the gammas and x-rays can help increasing the tumour dose as tumour cells have more and more neighbours from which they can receive these gammas.

The local kerma component of the $^{157}Gd(n,\gamma)^{158*}Gd$ reaction is made up by the internal conversion electrons and the following high LET complex Auger electron cascade. Due to the extreme short nanometer ranges of the Auger electrons in particular, it is important to look at the micro distribution of these Auger sources since their biological effectiveness depends heavily on their distance to biological targets. The internal conversion electrons have a larger range, extending multiple cell layers, which could provide cross fire from gadolinium positioned outside the cell or in neighbouring cells.

Gadolinium also has a high affinity for photon interactions and, for neutrons above 6 MeV, it can also undergo neutron capture reactions were alpha particles or protons are produced. These other reactions, however, have a very low Q-value and neutrons above 6 MeV will have many orders of magnitude lower flux, especially at deeper sites [13]. This makes these other reactions not of importance in the assessment of GdNCT.

1.7. Tumour selective gadolinium compound targeting PSMA

Gadolinium is traditionally used as a contrast agent in Magnetic Resonance Imaging (MRI) [4]. Since the actual injected ion Gd^{3+} is toxic, it is shielded from the body by wrapping it in other molecules covering the ion and inhibiting it from causing damage. An example of a Gd^{3+} holding MRI contrast agent is named Gd-DOTA, of which many alterations exist [4].

Recently, such gadolinium-containing agents were bound to a ligand which has a high affinity for the Prostate Specific Membrane Antigen (PSMA) as presented on the membranes of prostate cells by Banerjee et al. [4]. PSMA is mostly presented on the cell membrane of active prostate cells and the expression of this antigen increases when the cell becomes malignant. Therefore, this PSMA targeting ligand is a promising candidate for chemical targeting, especially since it also targets metastasis originating from the prostate, as they present PSMA as well.

After binding to the PSMA on the membrane, the cell engulfs a significant fraction of the gadolinium containing compound and internalises it [11]. Most of this internalised compound will move towards the vicinity of the nucleus [4, 11].

1.8. GdNCT as a possible method to treat prostate cancer

Since prostate cancers and metastasis present PSMA on their membranes proportional to their cell activity, PSMA targeting molecules could be very useful in delivering treatments to these cancerous cells.

There is not yet a PSMA targeting boron complex available, making BNCT not yet viable for prostate cancer. However, with the recent discovery of this PSMA targeting gadolinium containing compound, it is possible to deliver gadolinium right to the cancerous cells, and potentially into the cells [4]. Although, the development was not intended to be used as an NCT delivery agent, the tumour-selective uptake and the gadolinium contained in the compound make it an excellent candidate for a gadolinium delivery agent in GdNCT. Thus, GdNCT is then possible to treat these types of cancer.

As this is a novel approach, no literature is available on the matter. Consequently, the main goal of this thesis is to study the efficacy and feasibility of using Gadolinium PSMA (Gd-PSMA) NCT as a possible adjuvant or secondary therapy for post treatment prostate cancer patients and to develop the methods needed for this assessment.

2

Details of Monte Carlo dose calculations

2.1. Monte Carlo particle transport and dose deposition

Particles in Monte Carlo simulations are transported from their source till their disappearance using random numbers. First their starting energy and direction are sampled based on provided distributions. Subsequently, in each computational volume, the Monte Carlo code uses information about the material in the volume to calculate interaction probabilities to randomly sample interactions. Such an interaction could change the direction and energy of the particle, produce secondary particles to transport, as well as result in the end of the particle being transported. If these secondary particles are not transported by the code for any reason, their kinetic energy should be deposited locally thus satisfying energy conservation.

To calculate the path of a particle, as well as the probability and location of any interactions along it, the Monte Carlo code needs a description of the exact geometry and material composition. This is typically achieved by the use of simple geometric volumes in which homogeneous distribution of materials is assumed, which allows for fast and efficient calculation of paths in those volumes.

For our purposes, the end goal is computational dosimetry i.e. to calculate the actual dose deposition. One way to acquire the dose deposition in a volume is to count all energy depositions within the volume during the Monte Carlo simulation[1]. This direct counting of the sampled energy depositions is formally expressed as:

$$D \text{ per source particle} \approx \frac{1}{\# \text{ source particles}} \cdot \sum_{\text{event}} \frac{q_{\text{event}}}{V \rho_m}. \tag{2.1}$$

Here, the dose D per source particle is calculated by averaging the deposited energy of the event q_{event} per unit mass (expressed as the volume V times the mass density ρ_m) over the total number of source particles. With enough transported particles, the average deposition of energy per source particle in each of the different volumes converges. However, these events are discrete and randomly sampled with variance in energy and the total event-count. This means that a Monte Carlo sampling variance is present. If the interaction probability is very low for a given flux through the material, the resulting small number of sampled events increases this variance, making results less precise.

2.2. Dose from Monte Carlo track-length estimated flux

To reduce variance, one can implicitly force interactions to happen. This can be done without affecting the particle transport behaviour. In general, the absorbed dose D can be expressed, depending on the particle flux $\Phi(\vec{r}, E, t)$, by

$$D = (\rho_a / V \rho_m) \int_{\vec{r}} \int_t \int_E H(E) \sigma(E) \Phi(\vec{r}, E, t) \, dE \, dt \, d\vec{r} \text{ from [18].} \tag{2.2}$$

In Equation 2.2 the average absorbed dose D in a volume is calculated by the product of the energy dependent microscopic cross-section $\sigma(E)$ for every possible reaction in the material, the atomic density ρ_a, the flux Φ

---

[1]Counting these distinct interaction energies can be done in MCNP using the F8 tally.

and the average energy deposition depending on energy $H(E)$. This product is then integrated over the time t, energy E and position $\vec{r}$.

To simplify Equation 2.2 one can assume that the flux is in steady state and therefore does not dependent on time. In addition, the integral over $\vec{r}$ could be moved inside resulting in

$$D = (\rho_a/V\rho_m) \int_E H(E)\sigma(E) \left(\int_{\vec{r}} \Phi(\vec{r}, E)d\vec{r} \right) dE \tag{2.3}$$

which can be approximated by means of Monte Carlo integration.

Monte Carlo integration works by summing randomly sampled points in the integration domain. However, there is no analytical expression available for the flux $\Phi(\vec{r}, E, t)$, making evaluation of the inner part of the integral for sampled parameters impossible.

To overcome this, instead of randomly sampling the parameters which the flux depends upon to evaluate Φ, the parameters can be taken from each random event in the volume during a Monte Carlo particle transport simulation. For the case of a single particle track in a volume, the volume integrated flux comes down to the track-length of that particle within the volume. This allows the dose per source particle from Equation 2.3 to be converted to a track-length estimated flux to dose conversion given by

$$D = (\rho_a/V\rho_m) \int_{E_{\text{track}}} H(E_{\text{track}})\sigma(E_{\text{track}})L_{\text{track}}dE_{\text{track}}. \tag{2.4}$$

The added track subscripts in Equation 2.4, denote that the variable is taken from a simulated particle track. A track is seen as the straight path between two events or volume boundaries where the energy and the material traveled in is constant along the track. The length of this track is denoted by L_{track}. Equation 2.4 can then easily be approximated using Monte Carlo integration using the sampled tracks as dependent variable. This is formalised by

$$D \text{ per source particle} \approx \frac{1}{\# \text{ source particles}} \sum_{\text{tracks}} (\rho_a/V\rho_g)H(E_{\text{track}})\sigma(E_{\text{track}})L_{\text{track}}. \tag{2.5}$$

Since this method allows to extract information also from tracks that did not lead to a sampled energy deposition, more samples are obtained, resulting in a lower variance overall. Additionally, here only average energy deposition (heating) numbers are used instead of sampled ones, further decreasing the overall variance[2]. However, this introduces a slight bias when particles under a certain energy are no longer transported, i.e. when a cut-off energy is used. Instead of depositing the energy locally as would be done in event based dose estimation, the path length of zero does not contribute to energy deposition in track-length based dose estimation. Nevertheless, for typical energy cut-off values this error is small.

If a particle loses all its energy in its first interaction, only one track needs to be simulated and counted. For uncharged particles like photons, this can be the case. Since when particles traveling trough various volumes, at each interface a new track must be started, the number of tracks outnumber the number of energy deposition events. Consequently, summing over the tracks is typically favourable to summing over the energy deposition events.

Charged particles continuously interact with electric fields, losing their energy in a more continues manner. This continues loss of energy is approximated by making many small sub-steps. When the charged particle is transported without colliding during that short track, the average energy loss per unit length due to electric interactions is used to decrease the energy of the charged particle, after which a new sub-step is started as a track. This causes the number of tracks for charged particles to be similar to the number of energy deposition events. Therefore no significant variance reduction can be achieved when summing over the track as supposed to summing over the energy deposition events. Thus, enabling the transport of charged particle could become computationally expensive.

2.3. Implementing track-length based dose calculations in MCNP6

In simulating the dose distributions of GdNCT for this thesis, a Monte Carlo particle transport code was used. This code was the Monte Carlo N Particle (MCNP) version 6 by the Los Alamos National Laboratory [15] which is capable of performing coupled neutron, photon and electron transport.

---

[2]Track lengths estimators for flux are available in MCNP as F4 tallies. Their results can be converted to a absorbed doses by multiplying them by the total cross-section and average heating numbers on a tally multiplier (FM4) card or by directly using an F6 tally.

Usually MCNP is not used for medical purposes, but its use in the field is steadily growing. Several updates to MCNP have made it more suitable for medial dose calculations. However, documentation on these newer methods is often hard to find.

The local dose deposition from neutron and photon interactions have been part of the mainstream applications of MCNP and are well documented. Additionally, for the typical application of MCNP, the photon kerma approximation is accurate enough and secondary electron transport is therefore not needed. Their implementation pertaining to this thesis can be found in Appendix A. The implementation of flux-based electron dose calculations in MCNP is, however, much less straight forward and less well documented.

Charged particles are treated differently in Monte Carlo particle transport codes. In photon and neutron tallies, MCNP allows the user to convert track-length based flux estimator tallies to dose tallies. In such case MCNP will use its internal cross-sections and heating numbers to calculate the resulting dose. However, MCNP does not allow this simple conversion for electron tallies[3]. To overcome this short coming, the flux-to-dose tables based on the electron collision stopping powers, which are calculated by MCNP itself, have been added manually to the dose calculation algorithm[4]. Those stopping powers are then used to convert the track-lengths to their average energy deposition which could then be converted to dose.

Electron stopping powers are known or can be calculated for a range of materials. These stopping powers include the energy loss to the medium per unit length due to collisions and radiative effects such as bremsstrahlung. The collision stopping power includes both energy loss by excitation of nuclei and, if the bounding energy is surpassed, ionisations of those nuclei. Since the collision stopping power used in the flux-to-dose table already includes the energy of the ionisation electrons, those electrons should not be transported to avoid counting them again later on[5]. This is in agreement with the method briefly described by Hélio Yoriyaz et al. [32]. This implementation of electron flux based dose tallies has been validated in both mesh and normal tallies together with all other tallies used in this thesis. The exact implementation of this tally and validation thereof is included in Appendix A.

The track-length electron dose calculation method used in this thesis still has some shortcomings. The electron stopping powers are only available above 1 keV, and energies of non-transported particles are no longer counted towards the total dose as they have zero track length. Both these shortcomings make the track-length estimator of dose for electrons slightly biased. Additionally, not transporting the energy of knock-on electrons results in a slight error as well although their ranges are very short. In MCNP however, it is impractical to obtain 3D dose distributions for electrons any other way, thus the developed method still formed the best approach.

---

[3]Special multipliers are not allowed in the `FM` card for electron tallies, although MCNP does have the necessary cross-section and heating numbers.

[4]The flux-to-dose table for the specific material is obtained by running MCNP with the `print 85` command which triggers the stopping power tables for all materials specified in the problem. One can increase the resolution of this table by adjusting the `efac` attribute on the `phys:e` card. The table is then placed manually on the `DE` and `DF` cards.

[5]In MCNP, the ionisation (knock-on) electron production by electrons is disabled by setting `rnok` to `0` on the `phys:e` card (`phys:e 7j 0`).

<div style="text-align: right; font-size: 3em;">3</div>

Monte Carlo simulated neutron capture benchmark

3.1. Monte Carlo neutron capture models

The isotopes of interest for GdNCT and BNCT are ^{155}Gd, ^{157}Gd and ^{10}B. Data files specifying the reaction cross-sections of these materials with respect to neutron capture is typically delivered along with the transport code in most Monte Carlo particle transport programs or can be provided by the user. In addition, these data files also need to specify the secondary particles produced in such a reaction such that they can be transported by the transport code. This includes their energy and direction distribution, which can be given in the form of models or tables.

Typically the user can specify which data files to use. The newest version of the tables that MCNP itself encourages to use are based on the ENDF/B-VII.1 Evaluated Nuclear Data Library from 2011. For neutron interactions, this database includes evaluations made at room temperature which is the best match available for body temperature. The tables used in this thesis for photons and electrons[1] are based on older evaluations which are still the recommended choice [17].

3.2. Benchmarking neutron capture models to literature

To evaluate whether the models and tables used to simulate the neutron capture reactions in MCNP6 are correct and adhere to basic expectations, a computer experiment was performed using different neutron capture materials.

3.2.1. Setup of the evaluations

A pure thermal neutron beam of 0.0253 eV was aimed perpendicular at a 1 μm thick foil of the material under evaluation. The area of the foil was chosen to be 1 m^2 to yield a 1 cm^3 volume. The density of the foil was chosen to be 1 g / cm^3 such that the mass of the foil was 1 g. These unit mass, volume and mass density allow for effortless switching between dose and energy. The experiment was repeated with a ^{155}Gd foil, a ^{157}Gd foil and a ^{10}B foil.

To evaluate the neutron capture reaction products and their energy this setup was simulated in MCNP. The simulations were performed with coupled neutron and photon transport. For gadolinium, an additional simulation was performed with coupled neutron, photon and electron transport. The kinetic energies of particles other than those transported were deposited locally at the site they were created.

Calculating the total energy of the secondary particles was done by tallying the energy flux through the front and back of the foils. Although the foil is thin, a small fraction of particles with short enough ranges could remain inside the foil. Dose deposition tallies were added to account for that fraction of the energy. The total created energy per particle type was then estimated as the sum of the outgoing energy and the

---

[1]Implemented by using `nlib=.80c plib=.12p elib=.03e` and specifying the correct `xsdir` to "xsdir_mcnp6.1_endfb".

deposited energy. To relate the total produced energy per particle type with the number of reactions in the foil, several types of neutron capture reactions were also tallied. Since a pure material was used, all neutron collisions in the foil must have been with that material.

Due to the high density of these foils, a particle transport program can decide to treat these foils as conductors. MCNP was obstructed to treat the materials as conductors in these experiments[2]. This ensures that MCNP treats the materials as it would do in treatment simulations.

Since the expected secondary particles can have very low energy, special attention was paid to the MNCP settings. For photons the energy cut-off was set to 1 eV. For electrons, working at energies below 15 eV can cause problems. In MCNP electrons around 10 eV could undergo elastic scattering without lossing energy. This happens over very short steps, orders of magnitude shorter than the geometry. Tracking those electrons would greatly increase the number of simulated steps for this single particle history before the electron escapes the geometry, effectively halting the simulation. To avoid this the electron lower bound cut-off energy was set to 15 eV instead of the minimally allowed 10 eV. Additionally, the Single event mode was used more often by increasing the energy threshold under which it was applied from 1 keV to 10 keV. This mode is considered more accurate and takes more time. These extra options are advocated for in the MCNP publication, "Low-Energy Photon/Electron Transport in MCNP6" [17]. The simulation settings are summarised in Table 3.1.

If a secondary particle falls below the energy cut-off the program does not transport the particle but instead deposits all of the energy locally. A basic expectation of Monte Carlo particle transport programs is therefore that the total Q-value of a reaction is properly accounted for, either in the kinetic energy of the transported secondary particles or in the locally deposited energy.

Table 3.1: Simulation settings overview specific to particle transport and geometry

Description of setting	value
Transported particles	neutrons, photons and electrons[a]
Incident neutron energy	0.0253 eV
Single event mode threshold energy	10 keV
Electron cut-off energy	15 eV
Photon cut-off energy	1 eV
Foil material	^{10}B, ^{155}Gd, ^{157}Gd or ^{155}Gd + ^{157}Gd
Foil area	1 m^2
Foil thickness	1 µm
Foil volume	1 cm^3
Foil density	1 g/cm^3
Foil mass	1 g
Foil conductivity	0

[a] Electrons were only transported in gadolinium foils. For these foils an additional
simulation was performed without transporting electrons as well.

3.2.2. ^{10}B neutron capture simulation results

The foil material in this simulation was specified as pure ^{10}B. The reactions as result of the incident thermal neutrons are stated in Table 3.2, along with the total released energies per particle type. As seen in the results, reactions other than ^{10}B(n,α)^{7}Li have very low incidence. Therefore, we can assume that the total released energy per reaction is close to the Q-value of the ^{10}B(n,α) reaction. The literature value for this Q-value is 2.79 MeV [29]. Here MCNP produces the correct energy within statistical error. In addition, the photon energy present suggests that MCNP correctly performs the decay of the ^{7}Li nucleus produced in the reaction by emitting gammas.

---

[2]This was done by setting the COND flag to -1.

Table 3.2: ^{10}B foil neutron capture energy balance as calculated by MCNP showing correct energy balance compared to literature.

Description	per ^{10}B(n,α) reaction
^{10}B(n,γ) reactions	1.30094E-4
^{10}B(n,p) reactions	1.47301E-7
^{10}B(n,α) reactions	$\equiv 1$
Created photon energy	4.47149E-1 MeV ($\pm$0.22%)
Non transported energy from neutron collisions	2.34195 MeV ($\pm$0.00%)
Total released energy in simulation	2.78910 MeV ($\pm$0.035%)
Literature Q-value of ^{10}B(n,α)	2.79 MeV [29]

3.2.3. ^{157}Gd neutron capture simulation results

In this simulation the foil material was specified as pure ^{157}Gd. In Table 3.3 all tallied reactions and the total energies of each particle type are displayed. The ^{157}Gd(n,γ)^{158*}Gd reaction by far dominated the reactions for thermal neutrons, therefore it can be assume that the total released energy as stated in Table 3.3 is close to the Q-value of just the ^{157}Gd(n,γ) reaction. Since the actual literature value for the Q-value of this reaction is 7.937 MeV [14], we see a discrepancy of 86 keV that is not present in the simulated data. This does not lie within the confidence bounds of the MCNP estimation.

After emission of prompt gammas, the nucleus of the ^{158*}Gd atom is still excited. That energy is mostly emitted in the form of internal conversion and Auger electrons totalling at 50-65 keV and x-rays totalling at 10.7-38.4 keV[2, 14, 19, 31]. The lack of electron energy in the simulation, even though the electrons have energies higher than the energy cut-off threshold, suggests that this de-excitation of the ^{158*}Gd atom is not completely performed by MCNP. If that is the case, the missing electrons and x-rays would explain the missing energy since they total between 60.7 and 103.4 keV [3].

Table 3.3: ^{157}Gd foil neutron capture energy balance as calculated by MCNP showing missing energy compared to literature Q-value.

Description	per ^{157}Gd(n,γ) reaction
^{157}Gd(n,γ) reactions	$\equiv 1$
^{157}Gd(n,p) reactions	0
^{157}Gd(n,α) reactions	1.87342E-9 ($\pm$0.01%)
Created photon energy	7.85057 MeV ($\pm$0.12%)
Created electron energy[a]	1.3912E-4 MeV ($\pm$24.49%)
Non transported energy from neutron collisions	2.44748E-6 MeV ($\pm$0.014%)
Total released energy in simulation	7.85060 MeV ($\pm$0.12%)
Literature Q-value of ^{157}Gd(n,γ)	7.937 MeV [14]

[a] This value was calculated in an additional run where the electrons were transported as well.

3.2.4. ^{155}Gd neutron capture simulation results

The foil material in this simulation was specified as pure ^{155}Gd. The results of this simulation are shown in Table 3.4. Again due to the low incidence of reactions other than (n,γ) we can assume that all energy came from the ^{155}Gd(n,γ) reaction. According to Abdullaeva et al. [2], the Q-value of the ^{155}Gd(n,γ) reaction is 8.54 MeV. As was the case with ^{157}Gd, nearly 80 keV is missing from our result compared to the literature. Since the electron configuration of ^{155}Gd is the same as ^{157}Gd, it seems likely that this is a similar problem to that of ^{157}Gd, were a similar amount of energy was missing.

---

[3] Cherry picking data from Stepanek et al. [31] and Abdullaeva et al. [2] does yield exactly 86 keV for the x-rays and electrons combined which matches the missing energy.

Table 3.4: ^{155}Gd foil neutron capture energy balance as calculated by MCNP showing missing energy compared to literature Q-value.

Description	per ^{155}Gd(n,γ) reaction
^{155}Gd(n,γ) reactions	$\equiv 1$
^{155}Gd(n,p) reactions	0
^{155}Gd(n,α) reactions	1.09618E-9 ($\pm$0.00%)
Created photon energy	8.46047 MeV ($\pm$0.24%)
Created electron energy[a]	7.93134E-5 MeV ($\pm$43%)
Non transported energy from neutron collisions	2.20898E-5 MeV ($\pm$0.00%)
Total released energy in simulation	8.46049 MeV ($\pm$0.24%)
Literature Q-value of ^{155}Gd(n,γ)	8.54 MeV [2]

[a] This value was calculated in an additional run where the electrons were transported as well.

3.2.5. Natural Gd neutron capture simulation results

The foil material in this simulation was specified as natural gadolinium with natural abundances of their isotopes. Since the importances to neutron capture are negligible for most isotopes, only ^{155}Gd and ^{157}Gd were used according to their natural abundances. The energies of secondary particles produced in neutron collisions with natural gadolinium are shown in Table 3.5. If both reaction rates are multiplied by their literature Q-values the relative importance of the two isotopes becomes: ^{155}Gd (19.84%) and ^{157}Gd (80.16%). This matches what Abdulleva et al. [2] reported, respectively 20 and 80%.

Table 3.5: Natural gadolinium foil neutron capture energy balance as calculated by MCNP showing relative importance of the two main isotopes in natural gadolinium.

| Description	per Gd(n,γ) reaction
^{155}Gd(n,γ) reactions	18.70%
^{157}Gd(n,γ) reactions	81.30%
Created photon energy	7.98616 MeV ($\pm$0.15%)
Non transported energy from neutron collisions	2.56325E-5 MeV ($\pm$0.00%)
Total released energy in simulation	7.98619 MeV ($\pm$0.15%)
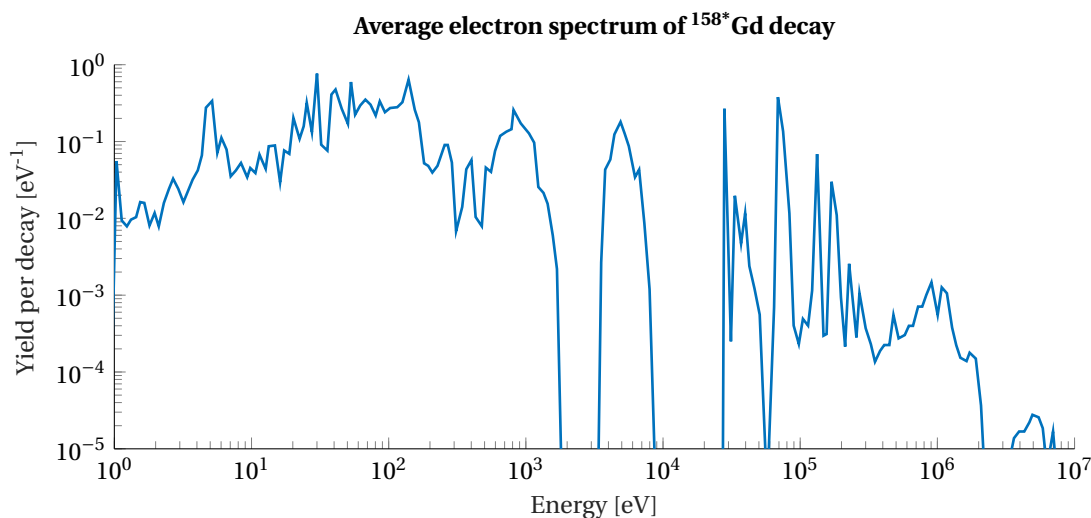
Figure 3.1: Digitised electron emission spectrum of ^{158*}Gd decay. This graph is a digitised version of the original as published by Stepanek et al. [31].

3.3. Supplementing incomplete neutron capture models

If energy is missing in Monte Carlo neutron capture models, it could be due to incorrect or missing data, or the incomplete decay of exited reaction products. The latter was the suspected reason for the apparent missing energy in the MCNP tables regarding gadolinium, suggesting that energy was conserved in the form of potential (not yet deposited) energy. However, we are interested in the time integrated energy deposition, therefore, we want to let all exited states fall back to their ground state as long as their half-life is short compared to the treatment time. This is the case for half-life of the neutron capture reaction product, ^{158*}Gd. However, no data on the decay of ^{158*}Gd is available in MCNP compatible format or in the ENDV libraries.

To overcome this, the missing particles can be added manually at the site of a neutron capture in the first simulation and then transported in a secondary simulation (similarly to Gierga et al. [12]). The publication from Stepanek et al. [31] describes the emission spectra of ^{158*}Gd decay for both the electrons (internal conversion and Auger combined) and the soft x-rays. The resulting emission spectrum of the electrons, totalling at 50 keV, is shown in Figure 3.1. For the x-ray spectrum, the average energies and yields of all shell transitions have been taken as input spectrum. Since there is no consensus about the total energy carried by these x-rays, the x-ray spectrum is scaled to have 36 keV [2], to completely match the 86 keV missing energy in ^{157}Gd neutron captures. This is also used for the energy missing in ^{155}Gd neutron captures as it falls within its sampling error.

The location of the added particles was chosen to be homogeneously distributed in all volumes where neutron capture took place. The quantity of the added particles was set proportional to the number of neutron captures in that volume. The angular distributions were assumed to be isotropic and the energies were sampled based on the emission spectra from Stepanek et al. [31].

<div style="text-align: right; font-size: 3em;">4</div>

Therapeutic GdNCT dose calculations

4.1. Using voxels for dose deposition

Absorbed dose is defined as deposited energy per unit mass. In Monte Carlo simulations, the sampled events and tracks are spread out over the whole available space. To achieve convergence, the sampled events have to be averaged. Since no two events have the exact same position, finite volumes need to be assigned in which all events or tracks and their energy can be averaged. For simplicity such volumes are chosen as cubes at steady intervals each bordering one another in each direction. The volumes in such a grid are named voxels, as the 3D equivalent of pixels in 2 dimensional grids.[1]

The size of these voxels has an effect on the variance and convergence time of the simulations. Smaller volumes lead to lower number of samples and higher variance, while larger volumes provide less spatial information. Another practical limitation is the resolution with which tissue composition can be determined using MRI or Computed Tomography (CT) data. Therefore in this thesis the voxel size was chosen to equal that of typical CT and MRI images, i.e. $1 \times 1 \times 2.5$ mm with the long axis in the Caudal-Cranial direction.

4.2. Geometry and material composition description (Phantom)

A Monte Carlo particle transport program needs a description of the geometry to use for calculations. The materials and geometry of the patient are typically known or can be approximated on a voxel level and could therefore also be specified at that level. However, the description can also be defined by separate larger independent geometrical shapes. Due to the implementation of most transport codes, particle tracks through less complicated geometries can be simulated faster. In addition, since these codes often can handle arbitrary geometries, they are typically not optimised for the much simpler voxel based description.

The speed-up acquired by the use of simple geometric shapes instead of voxels of the description was clearly shown in MCNP as well. The computation time per source particle on a phantom described by $5 \cdot 10^5$ cubic voxels was about 60 ms, whereas this was about 0.3 ms for a similar phantom described by a few simple geometric shapes. This difference of a factor of 200 was mainly due to the lack of optimisation in MCNP for voxel based geometry description.

For these reasons, in this thesis research the simplified phantom was used in which the geometry and materials are described by large geometric shapes rather then at the voxel level. In Figure 4.1, a projection of this geometry is shown on top of a reference CT image slice at the hight of the prostate. Two phantoms were used through out this thesis for legacy reasons.

Phantom A was defined as an oval cylinder with the long and short axes being 37.7 cm and 22.3 cm in diameter respectively. The height of the cylinder extended 20 cm above and below the centre plane beyond which little neutron flux was expected. In addition phantom A included two spherical metastasis with radii of 2.5 mm placed at various depths. The first centred 4 cm away from both central axes and the second centred 5 cm from both axes in the opposite direction, both at a 2 cm elevation compared to the main tumour. The

---

[1]Voxelised dose tallies are implemented in MCNP by `FMESH4:p` with `FM4 -1 0 -5 -6` for the photon dose, `FMESH4:n` with `FM4 -1 0 1 -4` for the neutron dose and `FMESH4:e` with the `DE` and `DF` cards for the electron dose as is specified in Appendix A.

main tumour was a sphere of 2 cm radius centred in the phantom. It was assumed that half the prostate cells were malignant and had taken up 700 ppm gadolinium. This was approximated by adding 350 ppm gadolinium to the whole of the prostate.

Phantom B was defined with slightly larger dimensions of 38 cm for the long axis and 26 cm for the short axis. It did not include metastasis and the central bulk tumour was thought to be 100% malignant, thus having an average gadolinium concentration of 700 ppm in the prostate.

Only materials descriptions are needed to perform the calculations. As the organs at risk were assumed to be of the same material as their surroundings they were not defined in both phantoms. Later on, for the use in the treatment planning, the location of these organs at risk do become important to evaluate what dose they receive. The method with which the organs at risk are handled is explained in Chapter 7.

The differences in tissue composition between, for example, bone and soft tissue, is less of importance to neutrons than for photons, especially in these early stages of evaluating this modality. The addition of the neutron capture agent does alter the total cross section of the material significantly. Therefore the only differentiation is made on the gadolinium concentration, allowing for fewer geometric shapes, speeding up the calculations. In a real-life application much higher quality patient specific descriptions will have to be implemented, but this is out of the scope of this thesis.

Even when using a description of the material composition and geometry on the voxel level, detail is lost. The underlying assumption is that the material in the voxel is homogeneous throughout the voxel. In Chapter 5, the consequences of this assumption of homogeneity for GdNCT are studied.

Up till now no time dependence has been discussed in the description of the geometry. Partially this is because movement of the patient will have very little effect due to the smooth neutron flux and chemical targeting. On the other hand, the concentration of ^{157}Gd can change in time due to burn up and the biological half-life of Gd-PSMA. However, the burn up of gadolinium is less than one percent for a 1000 ppm concentration delivering a typical therapeutic dose, and the biological half-life is expected to be several times larger than the treatment time. Therefore, these aspects are not taken into account, making the full geometry description time independent.

Another part of the geometry is the placement of the patient relative to the neutron beam. In practice the neutron beam is fixed and the patient is moved to obtain the wanted setup. To achieve a time independent geometry and to limit the calculation time, eight distinct patient positions relative to the beam ware implemented by fixing the patient instead of the neutron beam and defining eight separate neutron beams around the patient. These 8 different neutron beam were positioned in the xy-plane pointed to the centre of the patient's prostate. The beam tube exit is taken to be 5 cm in radius with a homogeneous neutron flux parallel to the tube. In Figure 4.1, these beams in the xy-plane are shown.

4.3. Absorbed dose simulations and post-processing pipeline

To simulate the dose distribution due to neutrons from a neutron beam, Monte Carlo simulations are performed in MCNP. To be used in a treatment planning system, these dose calculations have to be performed on the order of 300 times or more for a single treatment. This requires an efficient pipeline for performing the simulations and the necessary post-processing.

Transporting electrons adds a lot of complexity to the Monte Carlo particle transport due to the inherently different treatment of charged particles. Although the computation time per source neutron does not increase drastically (both about 300 μs per source neutron), the number of source particles necessary to obtain adequate statistics in the electron dose is about hundred times larger than the number of particles necessary to obtain similar statistics for the photon dose.

Therefore, in an effort to obtain a fast method to perform such simulations, the explicit transport of electrons has been disabled. Since almost all interactions that photons undergo in the body will produce electrons, be it the photo-electric effect, Compton scattering or pair production; disabling electron transport does effect the outcome. By not transporting these electrons, the dose deposition due to photons is less spread out than when electrons would have carried energy further away. The obtained speed-up, however, is necessary for the overal dose calculation to be suitable for a treatment planning system. In this chapter it is described how some of the errors from disabling electron transport have been corrected for during a post-prepossessing step of the MCNP output using kernels.

To denote the dose due to the various contributing particles, the letter D is used where a distinction is made between the dose due to electrons after electron transport D_{e} (only available with electron transport
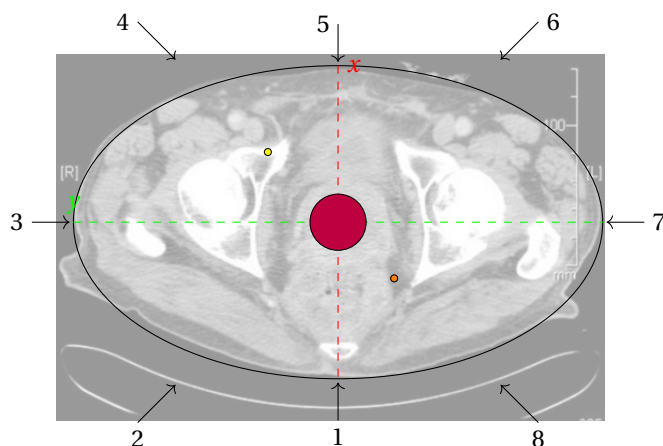
Figure 4.1: Top view of the phantom, overlaid on a CT scan[1]. The arrows indicate the possible orientations of the neutron beam, assumed to have a homogeneous neutron flux and a radius of 5 cm. Phantom A (displayed in this figure) was defined as an oval cylinder with the long and short axes being 37.7 cm and 22.3 cm in diameter respectively with the metastasis. Phantom B was defined with slightly larger dimensions of 38 cm and 26 cm without metastasis. The height of the cylinder extended 20 cm above and below the centre plane beyond which little neutron flux was expected.

enabled) and the photon dose D_p. In addition, the neutron dose D_n represents the energy from the secondary particles in neutron interactions other than the transported photons. Since all electrons in this problem are produced in photon interactions due to electrons not being produced in neutron interactions in MCNP, the electron dose D_e is essentially a better approximation of the photon dose D_p where the photon dose D_p correlates with the creation of electrons and the electron dose D_e correlates with their energy deposition.

Moreover, the subscript can also include the particle from which the energy originates, like the secondary particles from gadolinium neutron captures such as the x-rays ($D_{e, Gd\,x\text{-ray}}$), the electrons ($D_{e, Gd\text{-}e}$) and the gammas ($D_{e, Gd\text{-}\gamma}$). To denote the reaction densities the letter R is used, and in this thesis only the Gd(n,γ) reaction density $R_{Gd(n,\gamma)}$ is of interest.

When simulating an incident neutron beam of a specific energy group in MCNP with both coupled neutron and photon transport, MCNP can provide the average dose from all photon interactions D_p and the remaining dose from neutron interactions D_n in each voxel. The photon dose D_p contains all energy depositions from any photons, x-rays or gammas, including the gammas produced in the gadolinium neutron capture reaction. The neutron dose D_n contains the energy of all non-transported particles produced in neutron interactions, which is the complement of the photon dose as photons and neutrons are the only transported particles. Not present in both the photon dose D_p and neutron dose D_n are the missing secondary particles from the gadolinium neutron capture.

In Figure 4.2 the simulation result of an incident neutron beam of 764 eV to 1305 eV is shown for our phantom using beam 1 as shown in Figure 4.1. The dose distribution for the gammas is shown, in addition to the dose when electron transport would have been enabled. We see that assuming local deposition of photon interaction energies yields a different result than actually transporting the energy by electrons.

In Figure 4.2, an over estimation is made in the tumour when neglecting electron transport which suggests that the electrons produced by the gamma from the decay of ^{158*}Gd have too large of a range for them to be well approximated as being locally deposited. However, this is not certain since of all photon components, only their combined contribution is known. Therefore a post-processing method is needed to split the photon dose into that due to the gammas from ^{158*}Gd decay and that due to other photons after which both doses can be further processed separately. Additionally, during post-processing, an approximation of the dose deposition due to the missing particles from the ^{158*}Gd de-exitation is added as well. A full flow chart of the post-processing steps on the voxel scale is displayed in Figure 4.3. Each step in the flow chart is explained in the remainder of this chapter.
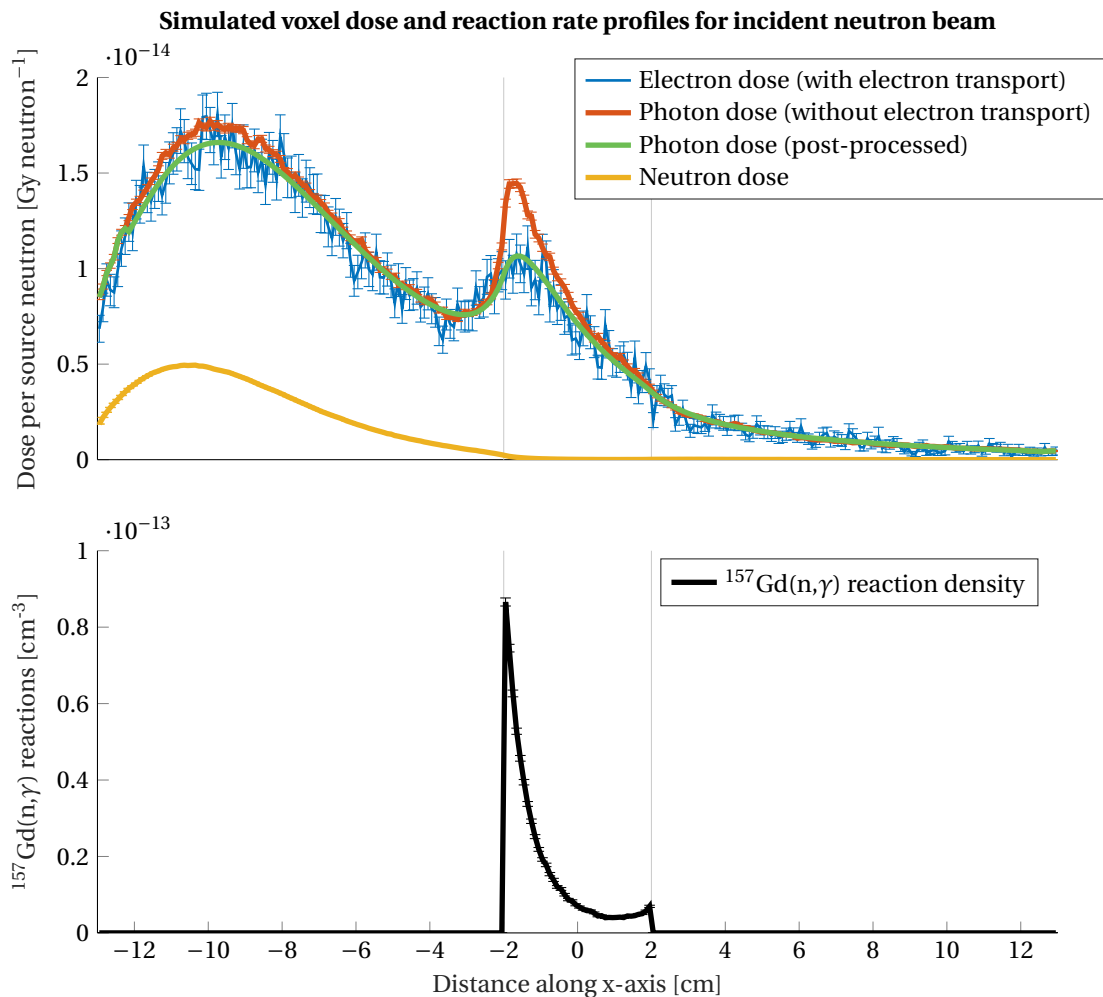
Figure 4.2: Profile of the neutron and photon doses (without electron transport) as simulated by MCNP for an incident neutron beam of 764 eV to 1305 eV in phantom B along the center profile of beam 1. The dose from the electrons generated in photon interactions, obtained with electron transport enabled, is shown as well. This shows that disabling electron transport requires additional processing to compensate for the deviations visible here. The post-processed total photon dose is depicted as well, showing a good agreement with the dose from photons after electron transport. Unfortunately, uncertainties are lost in post-processing. During the post-processing use is made of the calculated reaction rate profile shown in the lower half of the image.
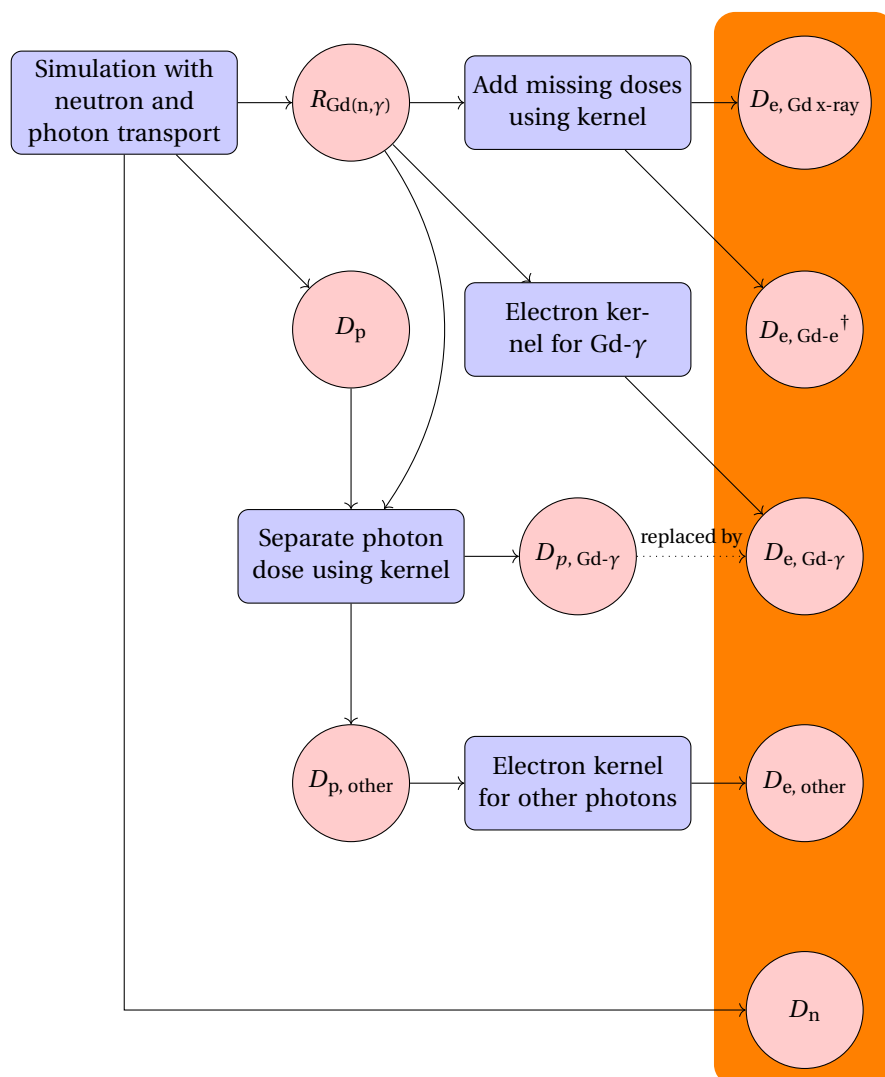
Figure 4.3: A flow chart displaying the post-processing steps taking the Gd(n,γ) reaction density $R_{\mathrm{Gd(n,\gamma)}}$, the photon dose D_{p} and the neutron dose D_{n} from the n-γ simulation results as input and producing the electron doses from the missing secondary x-rays $D_{\mathrm{e, Gd\,x\text{-}ray}}$, the missing secondary electrons $D_{\mathrm{e, Gd\text{-}e}}$, the missing secondary gammas $D_{\mathrm{e, Gd\text{-}\gamma}}$ and from the photons other than those from gadolinium $D_{\mathrm{e, other}}$. The electron dose due to the gammas from ^{158*}Gd decay $D_{\mathrm{e, Gd\text{-}\gamma}}$ replaces its photon variant $D_{\mathrm{p, Gd\text{-}\gamma}}$. The sum of all doses in the most right column represent the total absorbed dose. †The electron dose from gadolinium electrons is later split into the dose from neighbouring voxels and the dose from electrons produced in gadolinium neutron captures within the voxel. This is used for reconstruction of doses on the sub-voxel scale, which is explained further in Chapter 5.

4.4. Approximating doses due to gadolinium neutron captures

4.4.1. Kernel based dose deposition

As stated in Chapter 3, the neutron capture reaction is not completely described in the data files available in MCNP. The number of neutron captures in each voxel is known after the initial simulation, therefore it is possible to manually add the missing secondary particles from the ^{158*}Gd decay following the method specified in Section 3.3.

To achieve reasonable statistics, the method outlined in Section 3.3 requires a large amount of computational time. To overcome this, we apply a kernel based approximation. Here the average dose deposition per particle type from a neutron capture in a voxel is represented in a 3D grid that aligns with the voxel. This 3D dose distribution can be used as a kernel. By convolving the kernel describing the energy distribution per neutron capture with a matrix containing the number neutron captures per unit mass in all voxels the total dose contribution of those particles can be estimated.
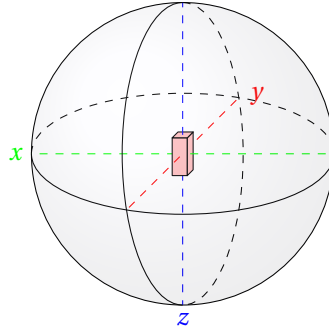
Figure 4.4: A large spherical volume of tissue equivalent material with at its centre a rectangular box containing 700 ppm gadolinium with size equal to a voxel ($1 \times 1 \times 2.5$ mm). For each missing secondary particle, a homogeneous source of that missing secondary particle is added to the central voxel. The dose depositions of the secondary particle originating from the center voxel is calculated for in a voxel mesh independent to the geometry that aligns perfectly with the center voxel.

To obtain the different kernels an experiment is designed. A large spherical volume of tissue equivalent material with at its centre a rectangular box containing 700 ppm gadolinium with size equal to a voxel ($1 \times 1 \times 2.5$ mm) is simulated in MCNP (see Figure 4.4). For each missing secondary particle, a homogeneous source of that missing secondary particle is added to the central voxel in a separate simulation. The dose depositions of the secondary particle originating from the center voxel is counted in a voxel mesh independent to the geometry that aligns perfectly with the center voxel. The dose deposition of each of the missing particles in that voxel mesh could then be seen as a kernel after the appropriate normalisations. The kernels for the missing electrons and x-rays are calculated in Section 4.4.2 and Section 4.4.3 respectively.

For calculating the electron kernel for the gammas produced in the gadolinium neutron captures, the source is not chosen to be a homogenous photon source within the voxel but rather a homogenous neutron source over the whole geometry. The neutron flux in turn produces the correct gammas in the voxel with the gadolinium along with other side effects. The extend of these side effects are separately measured in a similar experiment without the presence of the gadolinium (see Figure 4.7) and is used to negate the side effects in the dose deposition such that only the dose due to the gadolinium photons is tracked. The number of neutron captures in the voxel is counted as well for the correct normalisation of the dose deposition, providing us with a kernel. The electron kernel for the gadolinium gammas is calculated in Section 4.4.4.

However, such a kernel approximation is only valid for homogeneous mass densities, electron stopping powers and photon attenuation. For this thesis it is assumed that this is a reasonable approximation, in part because the presence of gadolinium minimally affects the electron stopping powers and photon attenuation.

4.4.2. Electron dose kernel of internal conversion and Auger electrons to calculate $D_{e, \, Gd-e}$

As previously stated in Chapter 3, the internal conversion and Auger electrons are missing from the secondary particles produced by MCNP, therefore they must be added. To obtain the kernel $K_{e, \, Gd-e}$ describing the dose

Electron dose profile in voxels due to secondary electrons following ^{158*}Gd decay, i.e. $K_{\text{e, Gd-e}}$.
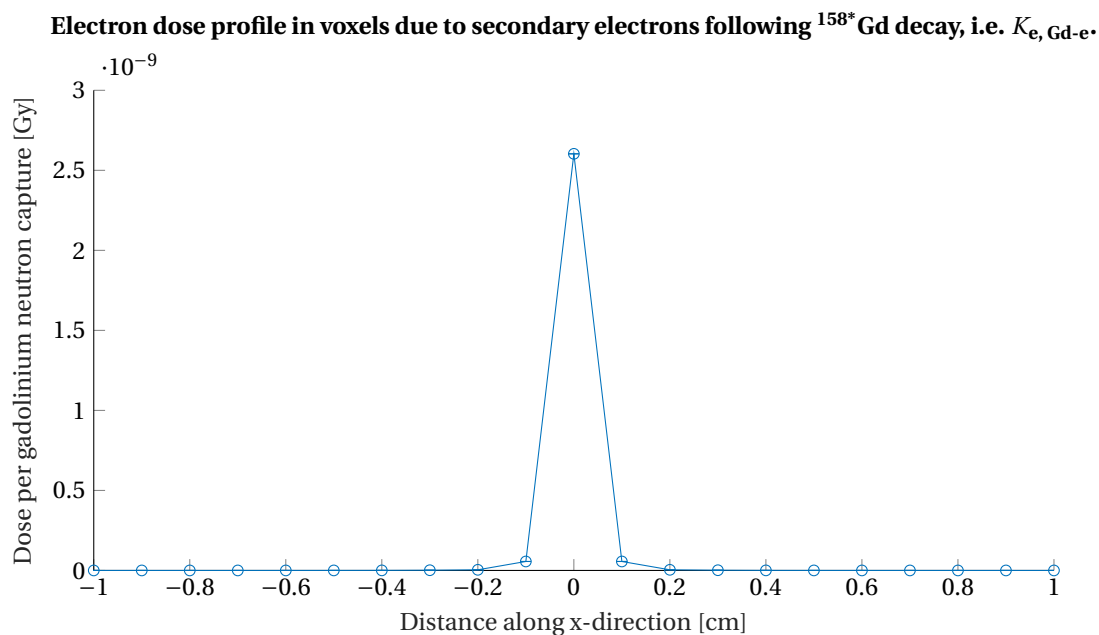

Figure 4.5: A trimmed profile of the electron dose distribution from neutron captures homogeneously distributed in the centre voxel normalised per neutron capture showing 81.23% ($\pm$ 0.03 p.p.) of energy remaining in the originating voxel. Convolving the full kernel with the neutron capture distribution yields the total dose distribution due to all electrons produced in the gadolinium neutron capture reactions.

contribution of electrons produced in gadolinium neutron captures in a voxel, the method described in Subsection 4.4.1 is used with the source definitions as laid out in Chapter 3. From Stepanek et al. [31] it is known that the maximal range for these particles is less then 8 cm, therefore that is chosen as a the radius of the material surrounding the voxel. Where the Gd-PSMA is in the voxel is unknown and a homogeneous distribution was chosen. Therefore, the kernel approximating the deposition and transport of the electrons following a ^{158*}Gd decay is simulated for a voxel with a homogeneous isotropic electron source with the energy spectrum taken from Stepanek et al. [31].

To obtain a 3D dose distribution of these electrons, a track-length estimated electron flux mesh was used that was converted to dose using a flux-to-dose look up table as explained in Section 2.3 and Appendix A.5.

In Figure 4.5, the central profile of the kernel is shown. In Figure 4.9 the profile is shown among the profiles of the other contributing particles that are produced following gadolinium neutron capture. The formal description of calculating the dose contribution of electrons produced in gadolinium neutron captures in this post-processing step is given by

$$D_{\text{e, Gd-e}} = R_{\text{Gd(n,}\gamma\text{)}} \circ K_{\text{e, Gd-e}}, \tag{4.1}$$

where the convolution operator is denoted by the $\circ$ symbol.

For practical reasons, the kernel is cut-off to correspond to a volume of $8 \times 8 \times 8$ cm, which neglects less than 0.1% of energy due to leakage outside this volume. The energy loss due to the premature stopping of electron transport below 20 eV is estimated at 0.3%. An additional 1.2% of energy is not present in the kernel either, this was presumed to be caused by the missing stopping powers for electron energies below 1 keV and interpolation errors of the stopping power table.

4.4.3. Electron dose kernel of soft x-rays to calculate $D_{\text{e, Gd x-ray}}$

As previously stated in Chapter 3, an additional 36 keV was missing from the energy produced in ^{157}Gd(n,γ) compared to the literature value in the form of soft x-rays. To calculate the kernel $K_{\text{e, Gd x-ray}}$ approximating the deposition and transport of these x-rays, an identical method to section 4.4.2 is used. The x-ray spectrum for the source was taken from Stepanek et al. [31] and the 3D dose distribution of the electrons produced in the photo-atomic events, a track-length estimated electron flux mesh was used that was converted to dose using a flux-to-dose look up table as explained in Section 2.3 and Appendix A.5.

Electron dose profile in voxels due to secondary x-rays following ^{157}Gd(n,γ), i.e. $K_{\text{e, Gd x-ray}}$.
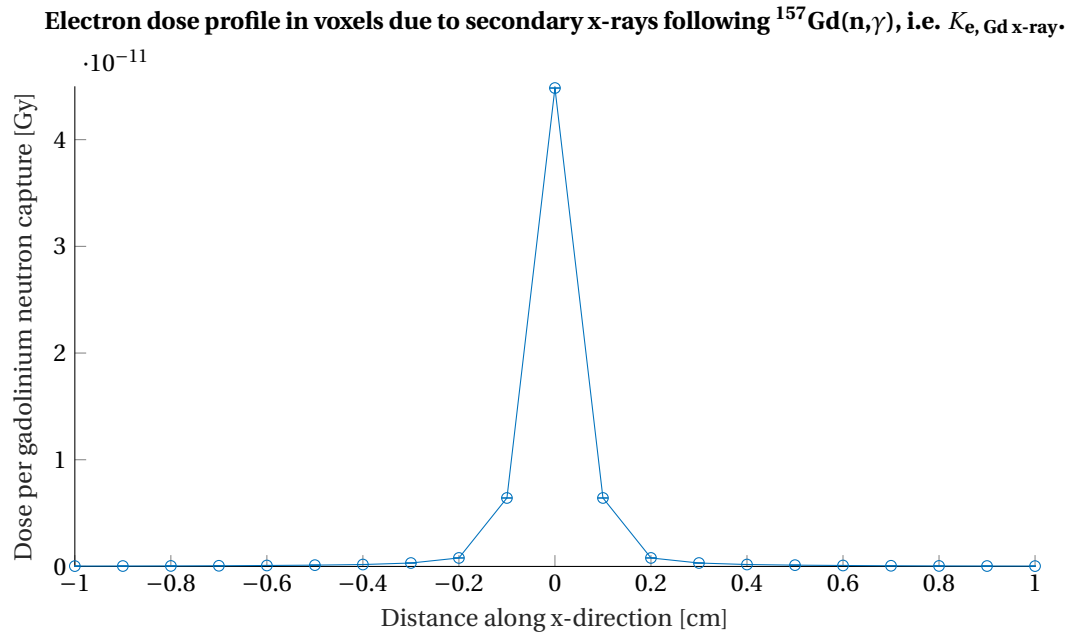

Figure 4.6: A trimmed profile of the x-ray dose distribution from neutron captures homogeneously distributed in the centre voxel normalised per neutron capture showing 1.9435% of the 36 keV energy remaining in the originating voxel. Convolving the full kernel with the neutron capture distribution yields the total dose distribution due to all x-rays produced in the gadolinium neutron capture reactions.

In Figure 4.6, the profile of the kernel is shown. It is visible that due to the longer range of these x-rays compared to the electrons produced in gadolinium neutron capture, the contribution to the local dose is about 2 orders of magnitude less than that of those electrons. In addition, the non-local energy deposition of the x-rays is also outweighed by the gammas produced in the same neutron capture reaction by about 2 orders of magnitude (see Figure 4.9).

For practical reasons and the low importance of this component, the kernel is cut-off to correspond with a volume of 8 × 8 × 8 cm. Although this neglects almost 30% of the total energy delivered by the soft x-rays, the remaining 10 keV is deposited over a very large region making it negligible compared to the contribution of the gammas produced in the same neutron capture reaction (see Figure 4.9). The energy loss due to the premature stopping of electron transport below 20 eV is estimated at 0.06%.

The formal description of this post-processing step is given by

$$D_{\text{e, Gd x-ray}} = R_{\text{Gd(n,}\gamma\text{)}} \circ K_{\text{e, Gd x-ray}}. \tag{4.2}$$

4.4.4. Electron dose kernel of gammas to calculate $D_{\text{e, Gd-}\gamma}$

To calculate the kernel that describes the dose distribution of the gammas produced in gadolinium neutron capture, one could use the same method as used for the electron dose kernels from x-rays and the secondary internal conversion and Auger electrons. However, the spectrum of these gammas is already known in MCNP, therefore they don't need to be artificially added. Instead a homogeneous neutron flux could be imposed that provides the neutrons to be captured by the gadolinium within the voxel, there the produced gammas could travel to outside the voxel where their 3D dose deposition after electron transport is counted.

However, the calculated electron dose also includes energy from neutron interactions other than the gammas from gadolinium neutron capture e.g. neutron captures in nitrogen or collisions with hydrogen. The simulation is therefore performed both with gadolinium and without gadolinium as control. The difference in doses between the control and the gadolinium positive voxel must then be due to the gadolinium neutron captures. Normalising this difference to the number of gadolinium neutron captures within the voxel yields the final electron dose kernel for just the gammas from gadolinium neutron captures. In Figure 4.7, both the control and gadolinium positive simulation is displayed.

(a) Tissue sphere without gadolinium.   (b) Tissue sphere with gadolinium, only in centred voxel.
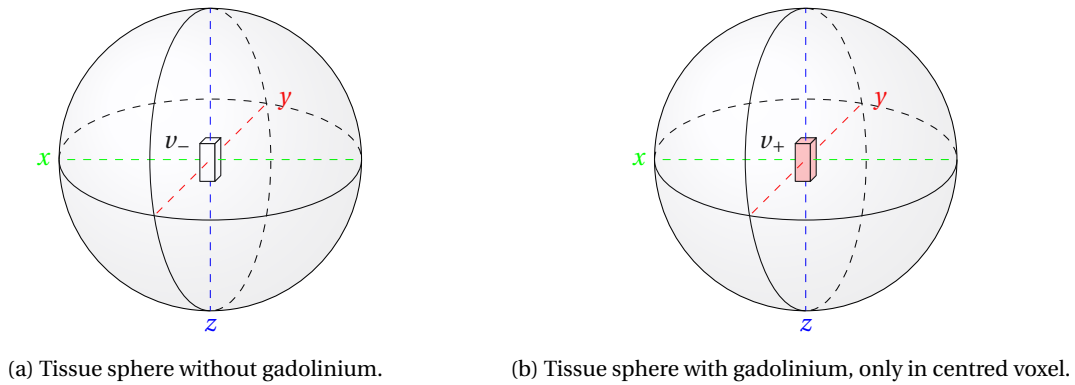
Figure 4.7: A large spherical volume of tissue equivalent material with at its centre a rectangular box equal to the size of a voxel (1 × 1 × 2.5 mm). The gadolinium concentration in the voxel is varied to see its added effect. Here v_+ denotes the voxel with gadolinium and v_- the voxel without gadolinium. The central box aligns exactly with the central voxel of the mesh used to store the dose depositions in.

In Figure 4.8, the cross section of the kernel obtained with electron transport as described here is shown along with a kernel obtained without electron transport enabled. The formal description of calculating the electron dose from the gammas produced in gadolinium neutron captures in this post-processing step is given by

$$D_{\text{e, Gd-}\gamma} = R_{\text{Gd(n,}\gamma)} \circ K_{\text{e, Gd-}\gamma}. \tag{4.3}$$

The gadolinium gamma dose $D_{\text{e, Gd-}\gamma}$ was already accounted for in the photon dose D_{p}. The dose that needs to be subtracted from the photon dose D_{p} is given by

$$D_{\text{p, Gd-}\gamma} = R_{\text{Gd(n,}\gamma)} \circ K_{\text{p, Gd-}\gamma}. \tag{4.4}$$

4.5. Separating photon doses during post-processing n-γ dose calculations

The therapeutic simulations provide the total photon dose from any photons, x-rays or gammas, including the gammas from the neutron capture reaction with ^{157}Gd. To distinguish between the dose due to the prompt gammas from the ^{157}Gd(n,γ) and all other photons, a kernel based method is devised. To investigate the contribution of neutron captures in gadolinium to the gamma component of the dose distribution, an computer experiment was set up similar to that performed in Section 4.4.4. However, unlike in Section 4.4.4 there was no electron transport in these simulations. This produces a kernel that when convolved with the gadolinium neutron capture density gives the contribution of the gadolinium gammas to the total photon dose. The remaining dose from photons other than gadolinium is simply calculated by subtracting this estimated contribution of the gadolinium gammas from the total photon dose.

In Figure 4.8, a profile is shown of the kernel approximating the photon dose deposition of gammas from gadolinium neutron captures. For practical reasons, this kernel is truncated to a 16 × 16 × 16 cm kernel which corresponds to 159 x 159 x 63 elements ($\approx 1.6 \cdot 10^6$ elements). This truncation is necessary to obtain affordable computation time. Convolution with such a kernel over the whole voxelised representation of the phantom using MatLab's native `convn` function still takes 40 CPU minutes.

To this convolution operation an optimisation was implemented. Due to the relative small number of non-zero elements in the matrix describing gadolinium neutron capture rates, an optimisation can be made compared to the naive convolution approach used in Matlab's native `convn`. Instead of performing $1.6 \cdot 10^6$ kernel evaluations per voxel for $8 \cdot 10^6$ voxels, one only has to perform $1.6 \cdot 10^6$ kernel evaluations per voxel for $1.6 \cdot 10^4$ voxels containing gadolinium. Although some additional overhead diminishes the reduction in computation time, a speed up factor of 10 was still achieved, reducing the computation time from 40 minutes down to less than 4 minutes depending on the fraction of non-zero elements in the gadolinium neutron capture matrix. This convolution implementation was also used for the other smaller kernels in this chapter.

In order to achieve energy conservation, the cut-off tails of the kernel beyond the 16 × 16 × 16 cm were approximated by a 3D Gaussian function, with an empirically chosen standard divination. The Gaussian

Electron and photon dose profile in voxels due to gammas from ^{157}Gd(n,γ).
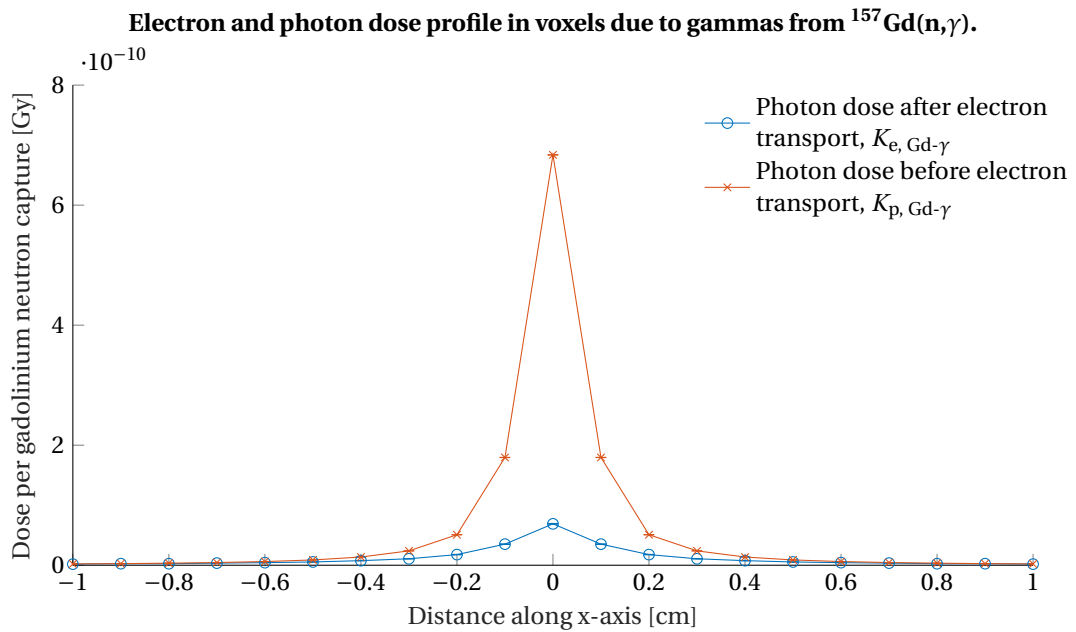
Figure 4.8: A trimmed profile of the gamma dose distribution from neutron captures homogeneously distributed in the centre voxel normalised per neutron capture showing the effect of electron transport on this dose component. Convolving both kernels with the neutron capture distribution yields the total dose distribution before and after electron transport which can be used to adjust the full dose distribution.

**Electron dose profiles in voxels due to gammas, x-rays and electrons following ^{157}Gd(n,γ).**
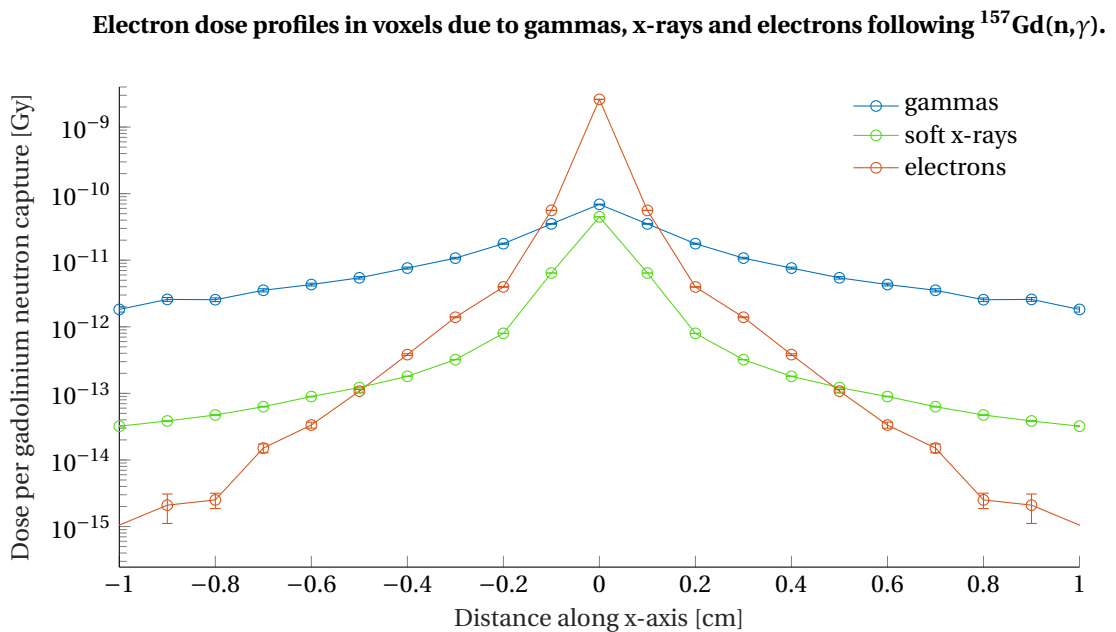

Figure 4.9: A trimmed profile of the dose distribution from neutron captures homogeneously distributed in the central voxel normalised per neutron capture showing the local importance of the electrons and the non-local importance of the gammas. The soft x-rays contribute minimal to both the local and non-local dose.

kernel was scaled such that it contained all of the 7.9 MeV of gamma energy per neutron capture that was not already present within the $16 \times 16 \times 16$ cm kernel. This Gaussian kernel was then only applied beyond the $16 \times 16 \times 16$ cm kernel. The standard deviation is chosen by empirical at 12.5 cm to yield minimal discontinuity between the inner $16 \times 16 \times 16$ cm kernel and the gaussian tails.

Implementation notes: A Gaussian is chosen for its efficient convolution of large 3D matrices due to its separability. Therefore the scaled Gaussian function is first applied on the neutron capture density $R_{\text{Gd}(n,\gamma)}$ in full, including its centre. Afterwards the central $16 \times 16 \times 16$ cm kernel is convolved with the neutron capture density $R_{\text{Gd}(n,\gamma)}$ and added to the tail approximation from the Gaussian. To undo the central part of the Gaussian it is subtracted from the central kernel prior to its convolution. This is an efficient implementation of the kernel based deposition of the electron dose due to the electrons from $^{157}\text{Gd}(n,\gamma)$.

As shown in the flow chart in Figure 4.3, the photon dose due to the gammas produced in $^{157}\text{Gd}(n,\gamma)$ will be replaced by a kernel based electron dose deposition from those same gammas. Therefore, after splitting the photon doses, the photon dose due to the gadolinium gammas can be disregarded.

4.6. Approximate transport of electrons from background photons

The gammas from gadolinium neutron captures can be replaced by the kernel estimation of the electron dose due to those gammas. However, the photon dose from the remaining photons in the problem has not been corrected yet. In Figure 4.2 it was visible that outside the gadolinium region, the error made by not transporting electrons was smaller than near the gadolinium region. This leads to the conclusion that the electrons produced by these photons are either in equilibrium or have a shorter range. However, we would still like to apply a post-processing step to this photon dose to achieve an even better agreement with the ground truth.

Since these photons have many sources, it is unfeasible to apply a kernel approximation to each reaction type like was done for the secondary particles of the neutron captures in gadolinium. Instead a Gaussian kernel is empirically optimised such that when applied to the photon dose, a better approximation of the electron dose is obtained.

As this kernel approximation is not valid near inhomogeneous density regions only the values more than one standard deviation from the outer rim of the phantom inwards were updated with the new smoothed values. To determine which voxels were in this area, a binary mask corresponding to whether the voxel is in- or outside the patient was eroded by the wanted distance of one standard deviation

The optimisation of the standard deviation was performed by minimising the mean squared error between the smoothed photon dose and the ground truth electron dose. The optimised Gaussian kernel had a 9 mm standard deviation and was therefore only applied 9 mm from the phantom's interface inward, resulting both in a better correspondence with the ground truth and lower variance.

4.7. Post-processed absorbed dose simulations in GdNCT

The MCNP output doses from n-γ calculations were post-processed using the pipeline as explained in this section, to better approximate the doses after electron transport and to include the energies of the missing (or removed) secondary particles from the gadolinium neutron capture. The profiles of the resulting various dose components making up the total dose is displayed in Figure 4.10. In addition, the total absorbed dose is shown as well.

What is seen in Figure 4.10 is how the particles attenuate with depth, leaving less and less energy for the deeper parts of the body. At the tumour we see that this attenuation increases. By the high cross-section of the gadolinium, many neutrons are captured before reaching the centre of the tumour. This effect is called the self-shielding effect, where the tumour itself shields the neutrons from penetrating deeper. Nevertheless, in the gadolinium electron dose component, a rise in energy on the rear side of the tumor is visible. This is because neutrons traveling in a path just missing the tumour to arrive at the tumours back side through scattering see far less attenuation then those traveling through the tumour even though their path is longer.

Note that as of May 1st 2018 no computational GdNCT studies [7, 12, 16, 19] have included electron transport or estimations thereof in their dose calculations like is done in this thesis. Therefore it is possible that those papers [7, 12, 16, 19] over estimated the efficacy of GdNCT as including electron transport diminishes tumour doses.
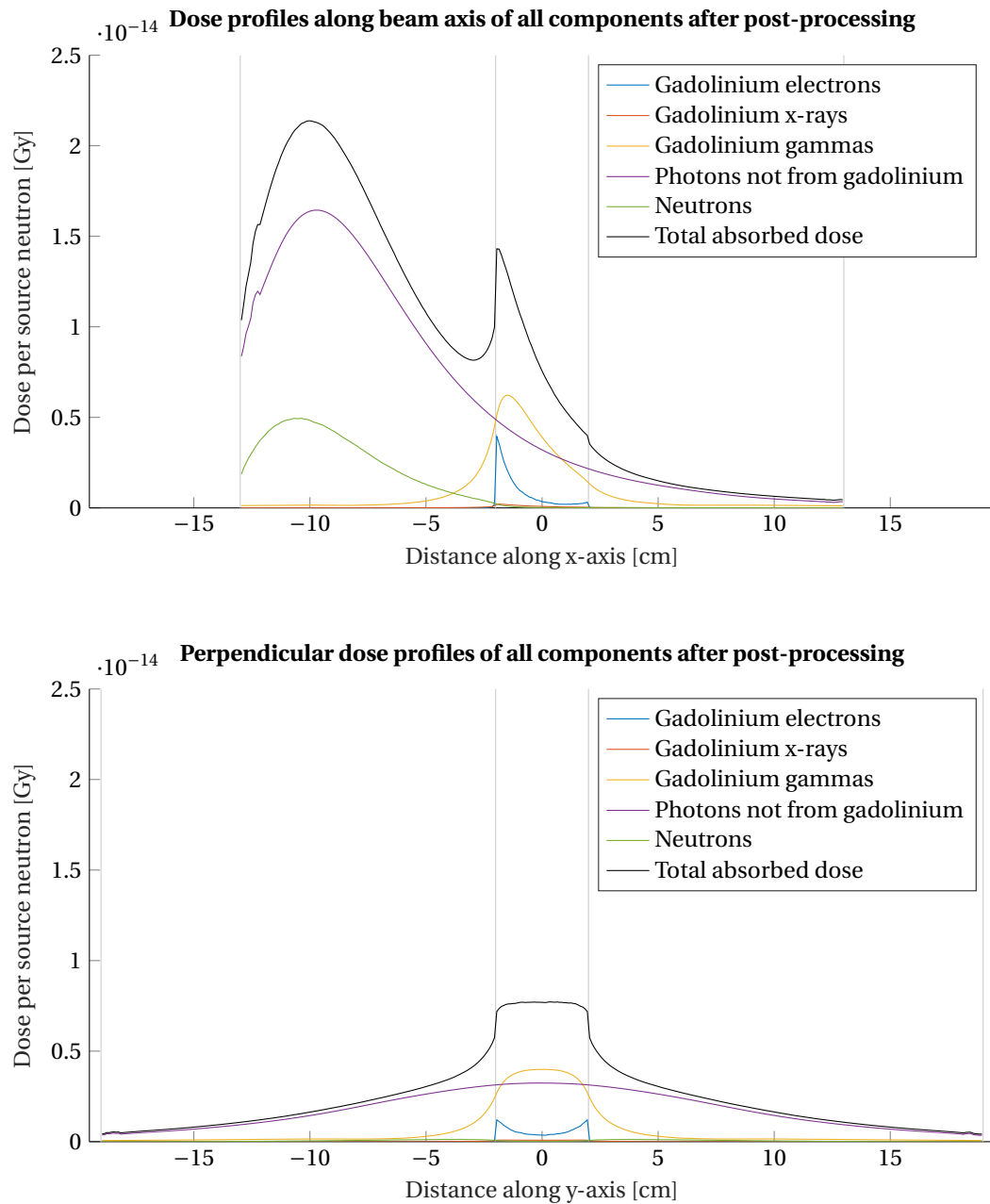
Figure 4.10: Profile of all the final post-processed doses for an incident neutron beam of 764 eV to 1305 eV in phantom B as is seen in the final column of the flow chart in Figure 4.3 including the total dose. The small discrepancy at 9 mm from the edges of the phantom are due to the Gaussian no longer being applied that close to the edge resulting in a small discontinuity.

<div style="text-align: right; font-size: 3em;">5</div>

Effect of sub-voxel inhomogeneities of Gd-PSMA distribution

5.1. Sub-voxel inhomogeneities of Gd-PSMA distribution

From imaging modalities like CT we have voxel level information. Methods exist to relate that information to actual atomic compositions under some assumptions, e.g. lookup tables allowing for conversion from CT intensities to tissue composition. Since Gd-PSMA is a good contrast agent for MRI, the Gd-PSMA concentrations can also be measured at the voxel scale via MRI. In practice, MRI has a lower resolution than CT. This means that when this information is sampled at an equal voxel size as CT it needs to be interpolated which can not bring back any lost higher spatial resolution.

At this point the concentration of each isotope of importance to GdNCT is known at the voxel scale and simulations are possible. However, a last prerequisite is an assumption about the distribution of those isotopes within the voxel. The simplest assumption is that the concentrations are homogeneous throughout the voxel. This is a good approximation for carbon, hydrogen and nitrogen since they are present in every cell naturally. However, this is not a good assumption for the foreign gadolinium since it only binds to tumor cells that form inhomogeneous clusters and structures smaller than the voxel size [4, 28]. The down-sampling of sub-voxel concentration distribution to average voxel distributions is illustrated in Figure 5.1.

In conventional radiotherapy, this is not an issue as the event cross sections are dependent on fairly homogeneously distributed properties. In photon therapy, the main property determining the cross section is the local effective atomic number, as for example the photo electric effect is more likely to occur with heavy atoms. In proton therapy, the property that determines the interaction cross section is mainly the electron/proton density of the material as most interactions with the material are due to the electric interplay of
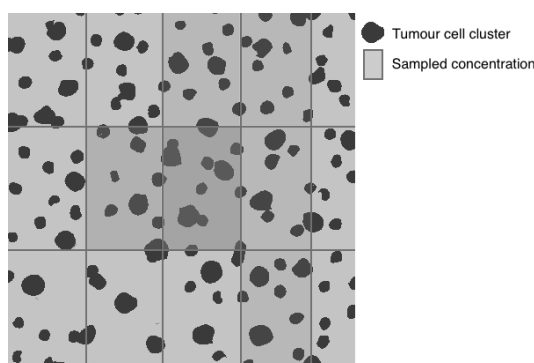

Figure 5.1: Figure illustrating the effect of finite resolution and voxel size on Gd-PSMA measurements in MRI. The total signal received by the MRI within the voxel is limited in the localisation precision. The gadolinium is assumed to be homogeneously distributed in the voxel losing the details on a sub-voxel scale.

these particles with the incident proton. Both these properties are fairly homogeneous, even at the sub-voxel scale. This means that the calculated absorbed dose for the whole voxel is a good estimator for the absorbed doses of each malignant cell in that voxel. For GdNCT the main property that determines the interaction cross section for neutrons is the gadolinium concentration, since it outweighs the effect of other isotopes that occur naturally in the body (see later in Chapter 6). The gadolinium concentration however is not well approximated by a homogeneous distribution due to the selectiveness of the compound.

For the very short (sub-voxel) range Auger and internal conversion electrons created in the decay of $^{158^*}$Gd the exact origin of these particles within the voxel does become important. Especially, since their origin is strongly correlated to the location of tumour clusters. Thus, the voxel dose is no longer a one to one estimator for the dose that is received by the malignant cells in the voxel. For the gammas created in the gadolinium neutron capture reaction, the assumption of homogeneity can be appropriate since the average path length extends well beyond the voxel, making the exact point of origin less important.

5.2. Relating voxel dose to dose in sub-voxel structures

To illustrate the error one makes by assuming the gadolinium to be homogeneously distributed, simulations were performed. In these simulations, a voxel filled with- and surrounded by tissue equivalent material was used. For the ground truth, it was assumed that a spherical cluster of various sizes is centred in the voxel with a 700 ppm gadolinium concentration (see Figure 5.2 (f) to (j)). To simulate the information loss in the imaging modalities and the voxelised description of geometry, the total amount of gadolinium in that sphere was also spread out homogeneously over the voxel in an other set of experiments (see Figure 5.2 (a) to (e)). The number of gadolinium atoms in the voxel thus was conserved in each column of Figure 5.2, i.e., (a) to (e) respectively had the same amount of gadolinium as (f) to (j). In each experiment a homogeneous isotropic thermal neutron source was imposed in the geometry extending multiple voxel lengths in each direction beyond the voxel.

Profiles of the dose caused by only the electrons produced in the gadolinium neutron capture reactions in these geometries both before and after electron transport are shown in Figure 5.3. The dose profiles were taken along the long central z-axis of each voxel, as shown in Figure 5.2. The mesh used to score the doses in Figure 5.3 was much finer than ever would be practical in patient scale simulations, however for a single voxel it was manageable. To illustrate what would have been known when using a traditional mesh where each physical voxel has a singular value, the "naive dose after electron transport by kernel" dose was measured over the voxel average and post-processed as would have been done in a voxel scale simulation via a transport kernel as explained in Chapter 4. It is important to note that for these small tumour clusters, given the finite resolution of the MRI data and a realistic voxel size, the "naive dose after electron transport by kernel" is in this point in time our only indication of how much dose is deposited in the tumour cells. However, having specified the spheres as being the ground truth we see that this heavily undermines the actual absorbed dose in the tumour cells. When not correcting for the inhomogeneity of the tumour cells containing gadolinium, doses to Gd-PSMA positive cell clusters will be underestimated while doses to Gd-PSMA negative cell clusters will be overestimated. Therefore, a method is wanted to translate the dose known at the voxel level to the sub-voxel observations made in this experiment.
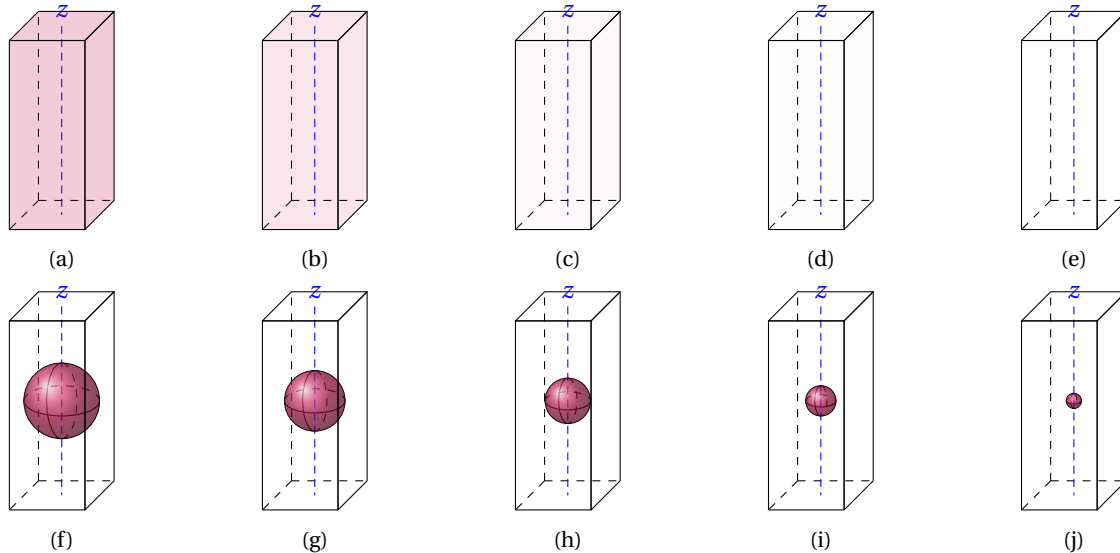
Figure 5.2: The bottom row shows spheres that each hold a fixed concentration of gadolinium with spherical radii of .5 mm, .4 mm, .3 mm, .2 mm and .1 mm from (f) to (j). The top row shows an equal amount of gadolinium as its lower neighbor in the bottom row but here it is spread out homogeneously over the voxel to simulate the reconstruction of the lower voxel after imaging using MRI. The voxels are surrounded by tissue equivalent material extending multiple voxel lengths.
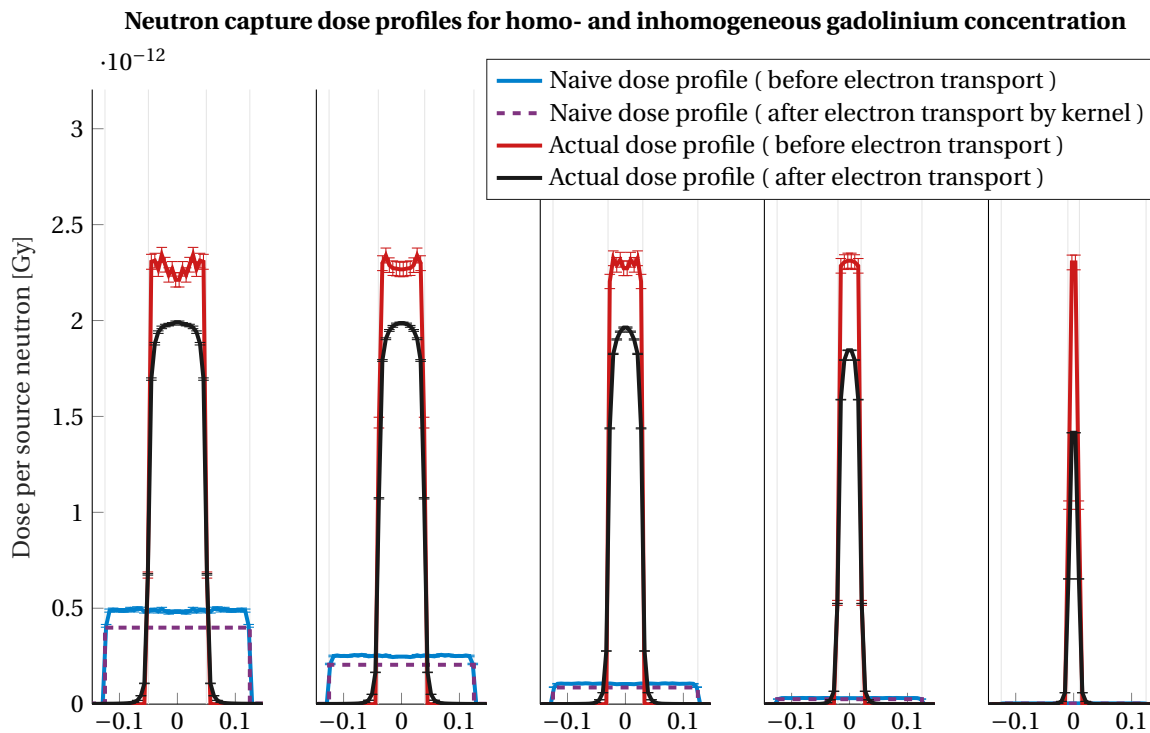
Figure 5.3: Profiles of the dose only due to the electrons produced by gadolinium neutron captures. The actual and naive dose profiles correspond to profiles along the blue lines in, respectively, the bottom and top row of Figure 5.2. The doses before electron transport contain 50 keV at each neutron capture reaction with gadolinium while the doses after electron transport contain the actual dose deposition after transport of those 50 keV of electrons. Each sphere contains $700 \, \mu g/g \, {}^{157}Gd$. From left to right, the spherical radii are .5 mm, .4 mm, .3 mm, .2 mm and .1 mm. The outer grey lines show voxel edges, while the inner grey lines show tumour edges. Note: radial symmetry was used to lower variance.

As the severity of the dose under-estimation depends on the actual size of the cluster, this was chosen as a parameter of interest in creating a method to translate the voxel scale observations to the doses in sub-voxel tumour clusters.

In our notation, we would like to distinguish between the voxel average doses as have been used up till now, the sub-voxel doses to Gd-PSMA positive cells and Gd-PSMA negative cells averaged over the voxel. This will be stated in the superscript of the dose symbols where the doses D used prior to this chapter are analogous to D^{voxel}, and the doses $D^{\text{Gd-PSMA}^+}$ and $D^{\text{Gd-PSMA}^-}$ respectively represent how the average voxel dose D^{voxel} is divided between the Gd-PSMA positive and negative cells.

If the tumour selectivity of Gd-PSMA is high then the dose to the Gd-PSMA positive cell clusters in the voxel is a good estimator for the tumour dose within the voxel. In creating the voxel dose to sub-voxel dose conversion method, it was therefore assumed that all the Gd-PSMA containing cells are tumour cells and all Gd-PSMA would be confined to the tumour cells.

The first step in constructing this model was to formally describe the energies involved respecting energy conservation. We are only concerned in the energy of electrons that originated from the voxel, as their point of origin corresponds to the sub-voxel tumour. Energy that arrives from neighbouring voxels due to transport of these electrons, do not originate from the sub-voxel tumour of interest. In our prepossessing step we only calculated the total dose due to the gadolinium electrons in a voxel. Now we want to differentiate between the voxel dose $D^{\text{voxel}}_{\text{e, int. Gd-e}}$ due to internally created electrons and the voxel dose $D^{\text{voxel}}_{\text{e, ext. Gd-e}}$ due to externally created electrons. We can split the kernel used in Section 4.4.2 into two separate kernels where the dose staying within the voxel can be expressed by

$$D^{\text{voxel}}_{\text{e, int. Gd-e}} = R^{\text{voxel}}_{\text{Gd(n,}\gamma\text{)}} \cdot K^{\text{voxel}}_{\text{e, Gd-e}}(0,0,0) \tag{5.1}$$

and the dose due cross-fire from other voxels is expressed by

$$D^{\text{voxel}}_{\text{e, ext. Gd-e}} = D^{\text{voxel}}_{\text{e, Gd-e}} - D^{\text{voxel}}_{\text{e, int. Gd-e}}. \tag{5.2}$$

Here we use the central kernel value to determine the fraction of electrons remaining in the voxel, leaving the residual values to calculate the external dose component.

Using these newly defined doses, the energy $E^{\text{voxel}}_{\text{int. Gd-e}}$ deposited from the gadolinium electrons in the voxel originating from the same voxel can be calculated using

$$E^{\text{voxel}}_{\text{e, int. Gd-e}} = m^{\text{voxel}} \cdot D^{\text{voxel}}_{\text{e, int. Gd-e}}. \tag{5.3}$$

The energy here is put in terms of the mass m^{voxel} of the voxel and the average voxel dose $D^{\text{voxel}}_{\text{int. Gd-e}}$ due to gadolinium electrons originating from within the voxel. If the range of the electrons that did not leak out of the voxel can be assumed negligible for now, then all their energy is completely deposited within the Gd-PSMA positive cells. The energy to both the Gd-PSMA positive and negative cell clusters can then be approximated by

$$E^{\text{Gd-PSMA}^+}_{\text{e, int. Gd-e}} \approx E^{\text{voxel}}_{\text{e, int. Gd-e}} \text{ and}$$
$$E^{\text{Gd-PSMA}^-}_{\text{e, int. Gd-e}} \approx 0. \tag{5.4}$$

Converting these energies back to the absorbed doses, can be done by

$$D^{\text{Gd-PSMA}^+}_{\text{int. Gd-e}} \approx \frac{E^{\text{Gd-PSMA}^+}_{\text{int. Gd-e}}}{m^{\text{Gd-PSMA}^+}} \approx \frac{m^{\text{voxel}}}{m^{\text{Gd-PSMA}^+}} \cdot D^{\text{voxel}}_{\text{int. Gd-e}} \text{ and}$$
$$D^{\text{Gd-PSMA}^-}_{\text{int. Gd-e}} \approx 0. \tag{5.5}$$

To test the model given by Equation 5.5, the equation is plotted against the data obtained in the computer experiments from Section 5.2 in Figure 5.4. It is apparent that although the model does predict the correct behaviour before electron transport, it does overestimate the tumour dose relative to the voxel dose when electron transport is enabled. This indicates that the fraction of energy leaking out of the sphere increases for smaller structures. Therefore, the assumption about the negligibility of these electron ranges is incorrect and the electrons that did not have enough range to leave the voxel can still have enough range leave the tumour clusters and enter healthy tissue within the voxel.

Relative difference between precieved voxel dose and actual tumour dose.
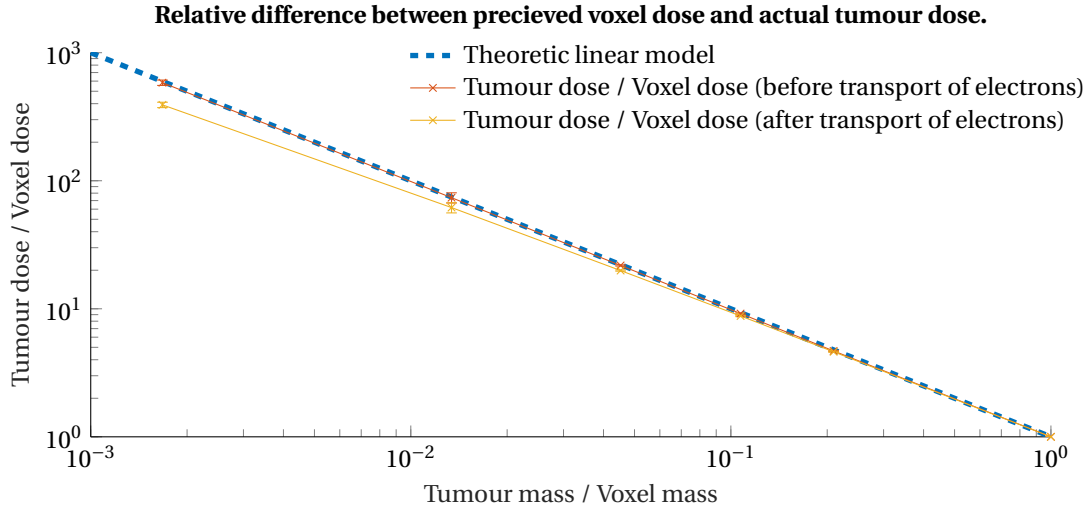
Figure 5.4: The relation of the volume ratio between the voxel and its tumour cells and the average dose ration between the tumour cells and the voxel. Doses here are normalised per neutron capture with gadolinium, thus any self-shielding does not contribute to the deviations from the model. Our model does correctly predict the dose ratio prior to electron transport but this breaks when electron transport is enabled.

To account for this leakage of the energy from the tumour into the healthy parts of the voxel in our model, a leakage parameter l is added. The leakage parameter describes the fraction of the energy due to the internal gadolinium electrons that leaks out of the tumour cluster. This leakage parameter is defined such that after incorporating it the into Equation 5.4 one can calculate the energies received by the tumour and healthy tissues by

$$
\begin{aligned}
E^{\text{Gd-PSMA}^+}_{\text{e, int. Gd-e}} &= (1-l)\cdot E^{\text{voxel}}_{\text{e, int. Gd-e}} \text{ and} \\
E^{\text{Gd-PSMA}^-}_{\text{e, int. Gd-e}} &= l\cdot E^{\text{voxel}}_{\text{e, int. Gd-e}}.
\end{aligned}
\tag{5.6}
$$

When converted back into absorbed doses, the conversion from the voxel doses into usable values can be done by

$$
\begin{aligned}
D^{\text{PSMA}^+}_{\text{e, int. Gd-e}} &= (1-l)\cdot D^{\text{voxel}}_{\text{e, int. Gd-e}} \cdot \frac{m^{\text{voxel}}}{m^{\text{PSMA}^+}} \text{ and} \\
D^{\text{PSMA}^-}_{\text{e, int. Gd-e}} &= l\cdot D^{\text{voxel}}_{\text{e, int. Gd-e}} \cdot \frac{m^{\text{voxel}}}{m^{\text{PSMA}^-}}.
\end{aligned}
\tag{5.7}
$$

The right hand sides of Equation 5.7 rely on two unknown parameters, the leakage l and the mass fraction of tumour to healthy tissue within the voxel.

The first unknown parameter is the total sub-voxel mass ratio of the Gd-PSMA positive (and negative) cell clusters relative to the whole voxel. One way to estimate this from MRI data is to assume that each tumour cell takes up a similar concentration of gadolinium. Therefore, the total gadolinium amount in a voxel as seen on an MRI image can be related to the total amount and mass of tumour cells. At the moment of writing, no information about the distribution of Gd-PSMA on a sub-voxel scale is available. Therefore, such fixed concentration is not yet known per unit of injected gadolinium. However, this thesis performs solely computer simulations were the gadolinium concentration in a tumour cell was defined to be 700 ppm and the mass fractions of healthy to tumour tissue were also defined. This ground truth data was used for the mass ratios needed in Equation 5.7.

The second unknown parameter is the leakage parameter l. Again, since no information about the shape and sizes of the Gd-PSMA positive cell clusters is available this factor has to be estimated as well. By assuming that all the Gd-PSMA positive cells are clustered together in a sphere like in Figure 5.2, leakage can be estimated from the mass fraction by creating a lookup table for leakages from different sizes of clusters. This look-up table of the leaked energy fraction consists of multiple simulated leaked fractions in computer experiments similar to that displayed in Figure 5.2. The leakages of energy out of the cluster are given in terms

Fraction of energy due to gadonlinium neutron capture electrons leaking out of sub-voxel tumor.
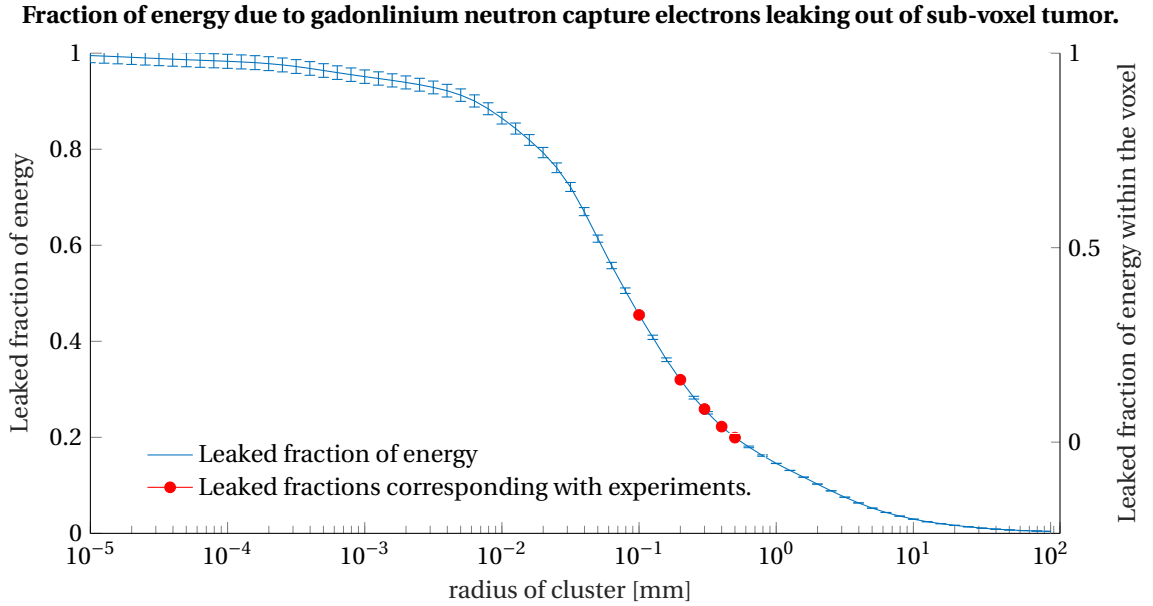

Figure 5.5: The fraction of energy due to electrons produced by neutron captures with gadolinium leaking out of a spherical tumour for various sizes. This fraction will asymptotically go to zero for large enough spheres. Note that this includes leakage to both in and outside of the voxel on the left axis and an estimation is made for just the leakage l within the voxel on the right axis.

of the sphere radii in Figure 5.5 but they can also be put in terms of the mass fraction of Gd-PSMA positive cells and the whole voxel.

During the post-possessing detailed in Chapter 4, a kernel was used to transport the electrons produced in gadolinium neutron capture. This kernel was calculated for a homogenous distribution of neutron captures in the voxel as no better distribution is known. In this chapter, however we state that the tumour cells and thus neutron captures could be clustered together. The two distribution assumptions wil yield in different fractions of energy to leak out of the voxel. As in Chapter 4, about 19% of the electron energy due to neutron captures was transported out the originating voxel, the remaining 81% should stay within the voxel to preserve energy. Thus, in Figure 5.5 the leakage out of the sphere is assumed to include this fixed fraction of 19% to leak out of the voxel. The leakage parameter l can then be obtained by rescaling the graph in Figure 5.5 such that zero leakage from the sphere to the voxel ($l = 0$) is identical to a general leakage out of the sphere of 19% as seen in the figure. This rescaling maps $l = 0$ to 19% general leakage and $l = 1$ to 100% general leakage in Figure 5.5 and is seen on its right axis. This is a crude estimation for the look-up table of energy fractions of the internal gadolinium electrons that is deposited within the healthy part of the voxel. The errors made in these assumptions are inherent to the different assumptions on which the two scales handle the distribution of the neutron captures.

Due to the neutron and photon radiation also present besides that of the gadolinium electrons, the actual difference in dose that is seen by a PSMA positive and negative cell in the same voxel following Equation 5.7 was at most 10 percent within the bulk tumour in the performed simulations, see Figure 5.6. More differentiation is possible when the thermal neutron flux increases relative to the photon and neutron dose components which is the case in shallower regions of the phantom, see Figure 9.4.

In Figure 5.7, the recipe detailed in Equation 5.7 has been applied to simulation data using neutrons from multiple energy groups. Seen is how the different energy ranges behave differently in the body. The dose boost due to the gadolinium is most dominant in the energy range between 1 keV and 20 keV. For fast neutrons, one sees that aiming or collimating the beam would be useful, whereas this is less the case with lower energetic neutrons since they do not retain their direction trough out their path in the body. However, as it is hypothesised that mostly epi-thermal neutrons will be suited for this type of therapy and fast neutrons will only be present in low numbers as contaminations. This means that the uncollimated 8 fixed neutron beams should already be able to provide most of the distributions in the total distribution space where multiple beams or collimators would be available.

Physical doses to tumorous and non-tumorous regions
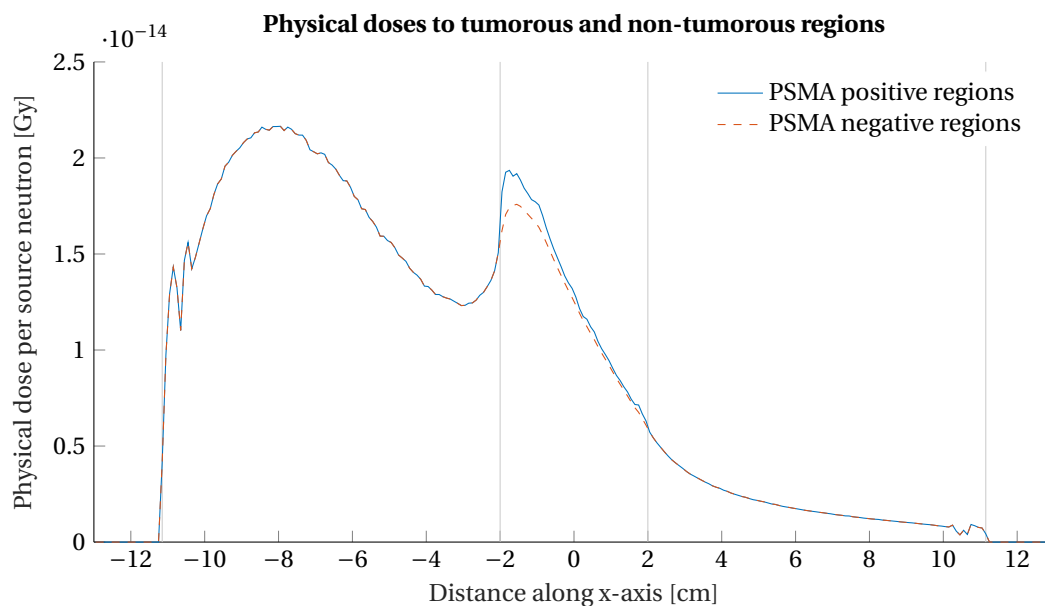
Figure 5.6: The different physical doses obtained in tumorous and non-tumorous regions when accounting for the sub-voxel behaviour of the electrons coming from the gadolinium neutron captures. Here the central tumour lies between the two grey lines. It contains 700 ppm in the PSMA positive regions but the ratio to PSMA negative and positive volume is one to one. This non-tumorous fraction could be blood vessels or dead/inactive tumour cells. This data is obtained from a coupled neutron and photon simulation with neutrons of 764 eV to 1305 eV for phantom A, using the post-processing method as described in this chapter and in Chapter 4.
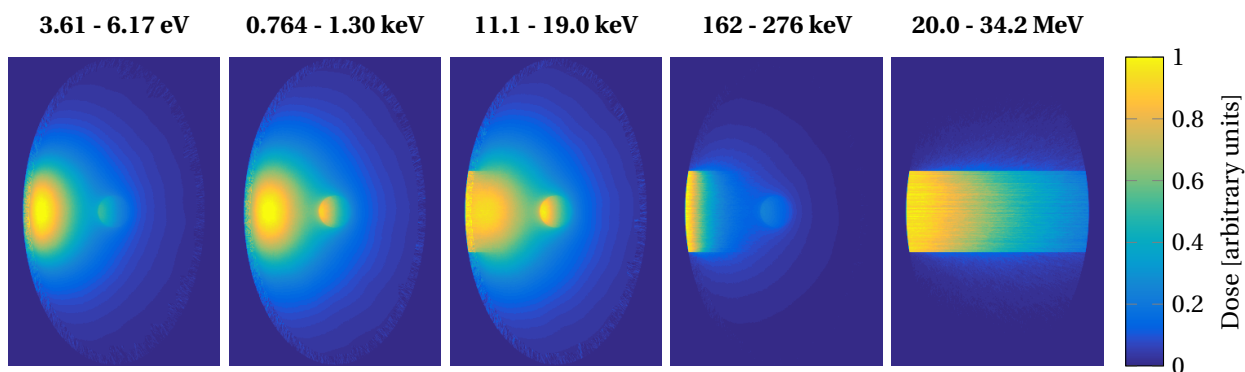
Figure 5.7: Normalised absorbed dose distributions in phantom A for multiple neutron beams of different energies from neutron beam 1. All dose components which were indifferent to gadolinium are present throughout the picture, for the internal gadolinium electron dose component which does discriminate between Gd-PSMA positive and negative cells, the dose to Gd-PSMA positive cells is shown only in the gadolinium containing regions. Seen is that the lower energetic neutrons don't retain their direction. The dose boost in the tumour decays fast due to the outer layer of gadolinium shielding the inner ones. The fast neutrons can provide a uniform dose along the beam, especially when irradiated bilateral. The boost due to gadolinium is, however, very low in these fast neutron beams.

6

Designing a cell culture experiment for measuring biological effects

6.1. Relating sub-voxel scale dose to biological effect

To relate absorbed doses to tissue damage or hazard in the radiation safety field, many different types of correction factors are applied. The physical or absorbed dose is equal to the total amount of energy per unit mass. A particle that delivers much energy over an extremely short distance could induce more complicated cell damage which is more difficult to repair. This effect is usually taken into account by adjusting the absorbed dose with a radiation weighting factor like the relative biological effectiveness (RBE) factor [33]. This factor relates the relative biological damage from a particle to that of a photon. An absorbed dose corrected by this factor is called a (photon) equivalent dose [33]. To account for the differences in importance and radio sensitivity of different organs, tissue weighting factors could be applied to the equivalent dose, giving the effective full body dose.

In radiotherapy the goals and situations are very different from those of the radiation safety field. In conventional radiotherapy, absorbed dose calculations are made on the voxel scale where typically the dose resolution is a few millimetres. These calculated doses are assumed to be specially continues and smooth, down to the single cellular organelles. This means that the energy deposition due to stochastic events in any cell organelle sized region could be seen as being Poisson distributed, on average matching the dose on macro scale. Since molecular targets in similar cells have similar volumes and sensitivity, a direct correlation exists between the effective dose on macro scale and the local cell damage.

However, this assumption of spatial smoothness does not hold when biological targeting compounds are used to deliver the radiation [5]. For example, a 20 nm range electron from a compound bound to the cellular membrane will never cause a direct hit to DNA, while a DNA incorporated compound could. This illustrates that similar equivalent doses on macro scale could yield a very different biological response in these cases.

Tissue weighting factors, used in radiation safety and conventional radiotherapy are defined on an organ scale (skin, liver, heart). This is appropriate since the doses are often smoothly distributed on the organ scales in the radiation safety field. In radiotherapy, however, no such weighing factors are used: instead, the doses are prescribed directly on the smaller voxel scale where high dose is required at some places and low dose a few millimetres next to it. Typical radiation therapy modalities yields doses that are smooth on this and smaller scales. To account for the much more inhomogeneous distribution of the energy deposition as found in compound delivered radiation which can differ per cellular organel, new weighting factors would have to be defined on the smaller cell organel scale. That would require the dose distribution to be known on that scale as well. Deriving such factors about the radiosensitivity of the different organelles in the cell is quite difficult, and a lot of research is still ongoing into which molecular targets are more sensitive to radiation [25, 30]. In addition, the relative concentrations of these compounds and their dose distribution at all different organelles must be known which is often not the case. This makes tissue radiation weighting factors unpractical for chemically targeted radiation.

A more practical way to account for these effects is to define a new factor that relates the absorbed dose on macro scale directly to the average biological effect in PSMA positive and PSMA negative cells within that

region relative to that of homogeneously deposited photons. Such a factor is the Compound Biological Effectiveness (CBE) factor [5, 23]. This factor can be determined experimentally for each type of cell without knowing the exact micro distribution or radiosensitivity of all organelles. To determine the CBE, a group of cells is given a known amount of the compound. Then absorbed dose calculations on the voxel scale can be made. On that scale the absorbed dose is independent of micro distribution effects. The observed outcome, like cell death, is then related to the same measure in a photon irradiated control with an absorbed dose such that the outcomes are equal. The factor that scales the absorbed compound dose to the equivalent absorbed photon dose is the CBE. The resulting CBE can then convert an absorbed dose on macro scale to the effective dose on macro scale, omitting the difficult to handle cell organel scale.

For the two main BNCT drugs, these CBEs have been measured [8, 13, 23]. Since the compound behaves in blood differently from tumour cells, these two each have their own CBEs [13, 23]. For the electrons produced in neutron capture in gadolinium in GdNCT, several distribution dependent RBE values exist. However, since all GdNCT cell culture experiments in the existing literature have been performed with gadolinium that had different biological distributions within the cell compared from that as found in Gd-PSMA, a new experiment needs to be designed in which a known absorbed dose at macro scale can be related to its biological damage.

A cell culture experiment was designed. Here intracellular or membrane bound Gd-PSMA is the only gadolinium present with extra cellular Gd-PSMA washed away. The narrow 2D geometry of a thin layer sees little radiation from neighbouring cells. This will cause most of the cell damage due to this gadolinium to be because of the gadolinium within that cell. This allows the CBE factor for intra cellular PSMA delivered gadolinium neutron capture to be measured. To do so, the **absorbed dose components to the cells have to be calculated** on a voxel scale and a **measurable biological effect needs to be produced** to relate it to these calculated doses.

To *calculate the dose components*, MCNP was used. Neutrons, photons and electrons were all transported in these simulations. Other produced particles were assumed to deposit their energy locally.

To assure a *measurable biological effect*, the experiment was simulated in advance to give insights into the required intra cellular gadolinium concentrations and other parameters. An interpolation model was derived from these simulations as a fast method to evaluate the influence of parameter changes during the design process of the study.

When measured, this CBE factor for the gadolinium electrons combined with the traditional RBE factors for the other dose components can be used to convert all of the absorbed doses to equivalent doses. For the long range electrons the exact origin and micro distribution is not of importance. For the gadolinium electron dose $D_{e, \text{int. Gd-e}}$ from neighbouring cells the CBE factor is no longer necessary and a standard RBE factor for electrons can be used as well as the neutrons and photons. Only the gadolinium electrons remaining in the voxel will need this new factor applied to them.

6.2. Cell culture experimental and simulation setup

In Figure 6.1 we see the rough geometry that is expected in this cell culture experiment. The thickness of the petri dish walls was put at 1.3 mm. The high density layer of cells from the LNCaP cell line was estimated to be between 10 and 20 μm thick. The material used in the problem for the bottom, top and side of the petri dish was pure polystyrene. The petri dish was filled with a liquid which was modeled as being tissue equivalent material (Soft Tissue, IRCU four component). The correct thermal treatment was applied to account for the chemical bonds of the hydrogen atoms. The cell layer is also simulated as tissue equivalent material for the Gd-PSMA negative control and gadolinium is added to the layer when simulating the Gd-PSMA positive experiments.

In each simulation a dose profile along the central axis of the problem was calculated. The doses were classified as caused by electrons produced by the gammas or the electrons produced in the gadolinium neutron captures. Energy from non-transported particles in neutron collisions were contributed to the neutrons. Since these particles were not transported, the neutron dose is a kerma approximation which is only valid under the assumption of a charged particle equilibrium. Since the range of most (90%) of the protons in the problem the dose is so small (< 10 μm) and presumed smooth over the whole problem, this is a reasonable assumption [2].

The simulations have been done separately for the neutron beam and the contaminating gamma beams since the ratio between their intensities was not yet known. After performing simulations with the neutron beam, the neutron captures were counted at each slice in the geometry. To account for the missing energy
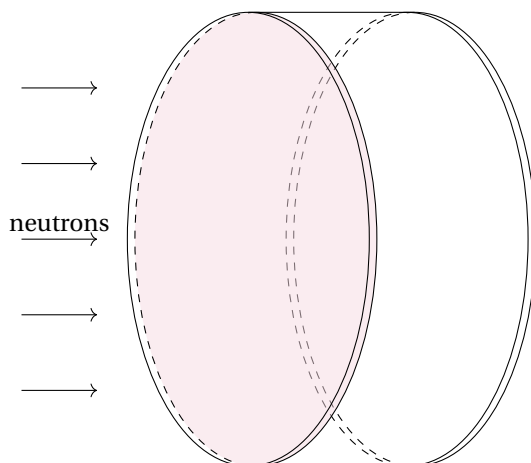
Figure 6.1: Setup geometry of the cell culture experiment. A plastic petri dish with a LNCaP cell culture on the bottom has been put on its side having the bottom with the cell layer (here in pink) on the left and the lid on the right. The remaining volume is filled with liquid to support the cells. The neutrons and contaminating gammas are coming from the left, passing through the plastic bottom, the cell layer, the liquid and then the lid of the petri dish.

in the MCNP neutron capture models for ^{157}Gd, the secondary particles were manually added to those slices where neutron captures were counted. These electrons were than transported, including the secondary electrons and photons they produced.

The available neutron irradiation locations were at the HFR-HB5 neutron beam in the Petten HFR reactor and the beam tube at the Reactor Institute Delft. From the Delft beam tube, gold foil measurements were available which provided the neutron yield per wavelength, totalling at an integrated flux of $2.7 \cdot 10^7$ cm^{-2}s^{-1} that is mostly comprised of cold to thermal neutrons [24]. The full spectrum is displayed in Figure 6.2. This measurement was performed behind a monochromator and a waveguide [27]. For the contaminating gammas present in this beam, no spectrum is available. Instead a normalised photon spectrum from elsewhere in the reactor is taken as an indication of the contaminating gammas after the waveguide.
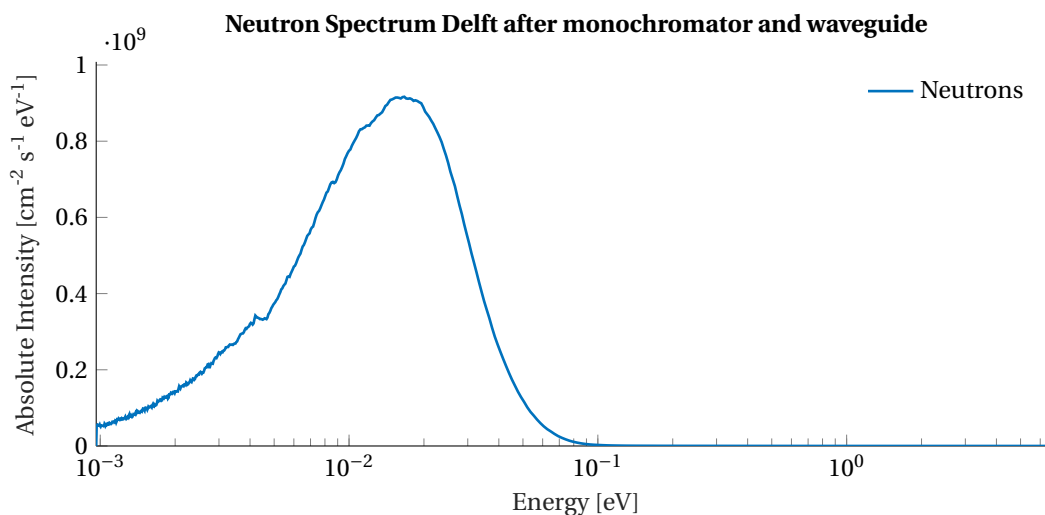
Figure 6.2: Neutron spectrum measured at the neutron bundle after the waveguide and monochromator in the RID reactor. These values were converted from the spectrum from [24] as function of neutron wavelength.

For the HFR-HB5 neutron beam in Petten, neutron measurements were also performed to asses the thermal, intermediate and fast neutron fluxes. The measurements showed a mostly thermal neutron flux relative to the intermediate and fast neutrons by 2 to 3 orders of magnitude. The measured neutron fluxes were:

$3.92 \cdot 10^6$ cm^{-2}s^{-1}, $2.02 \cdot 10^4$ cm^{-2}s^{-1} and $9.09 \cdot 10^3$ cm^{-2}s^{-1} for the thermal, intermediate and fast neutron fluxes respectively [22]. As only three bins are provided here the peak energy is not as easily determined as that of the spectrum in Figure 6.2. However, in this thesis the simulations were performed using the Delft spectrum and scaled to correct for the total integrated flux difference between the thermal component in the Petten and Delft beam.

6.3. Interpolation model for fast experimental parameter tuning

During the design of the cell culture experiment, higher and higher gadolinium concentrations were obtained by our partners at the NKI-AvL [10]. In addition, it was not yet decided whether enriched, partially enriched or non-enriched gadolinium was be used. To be able to provide quick estimation of the effect of such parameter changes, an interpolation model of the experiment was made where the parameter space was evaluated at several points which could be interpolated in-between.

The experiment design parameter space consisted of the gadolinium concentration, the enriched fraction and the width of the cell layer. The gadolinium concentration [Gd] was varied between 0.1 µg, 1 µg, 10 µg and 100 µg gadolinium per 1 g tissue; the enrichment fraction F was varied from natural gadolinium (F=0) to pure 100% ^{157}Gd (F=1); and the cell layer thickness W was varied between 10 µg, 15 µg and 20 µm. A total of 36 (= $4 \times 3 \times 3$) evaluations of the parameter space was performed. Each simulation was performed once for the neutrons present in the incident spectrum and once for the contaminating gammas also present.

First the effect of the gadolinium concentration was investigated. In Figure 6.3, the effect of increasing the concentration on the dose components from the neutron beam without contaminating gammas is displayed. Only the dose from electrons produced in the neutron capture reaction was influenced significantly by the gadolinium concentration. The effect was very linear and did not change with different parameter combinations, of which a few have been included in Figure 6.3 as well. Since the number of neutron captures increased with more gadolinium, a higher photon dose due to the photons produced in those reactions is expected as well. However this is effect is negligible in this 2D geometry where build up and cross firing is hardly as apparent as in 3D.
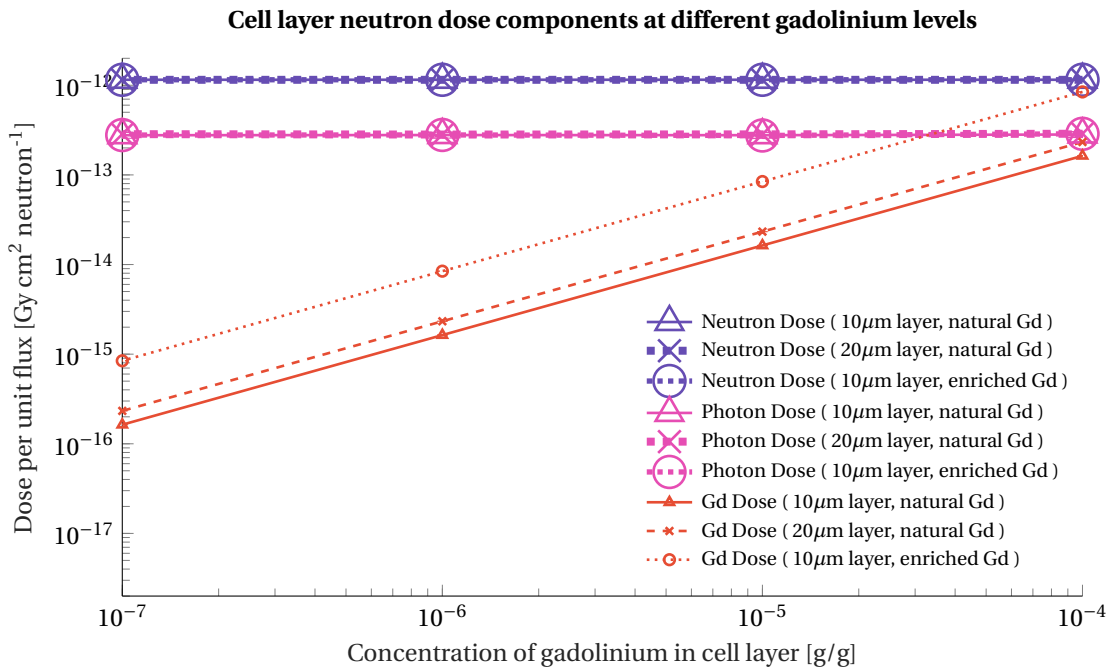
Figure 6.3: Neutron dose components in the cell layer evaluated for a range of Gadolinium concentrations for different enrichment levels and different cell layer thicknesses. All dose components, except for that caused by the neutron capture reaction itself, seem independent of concentration.

The second parameter investigated was the effect of the ^{157}Gd enrichment level. In Figure 6.4, it is again visible that this parameter only influences the gadolinium dose in the same linear manner as seen in Figure

6.3.

Cell layer neutron dose components at different levels of enrichment
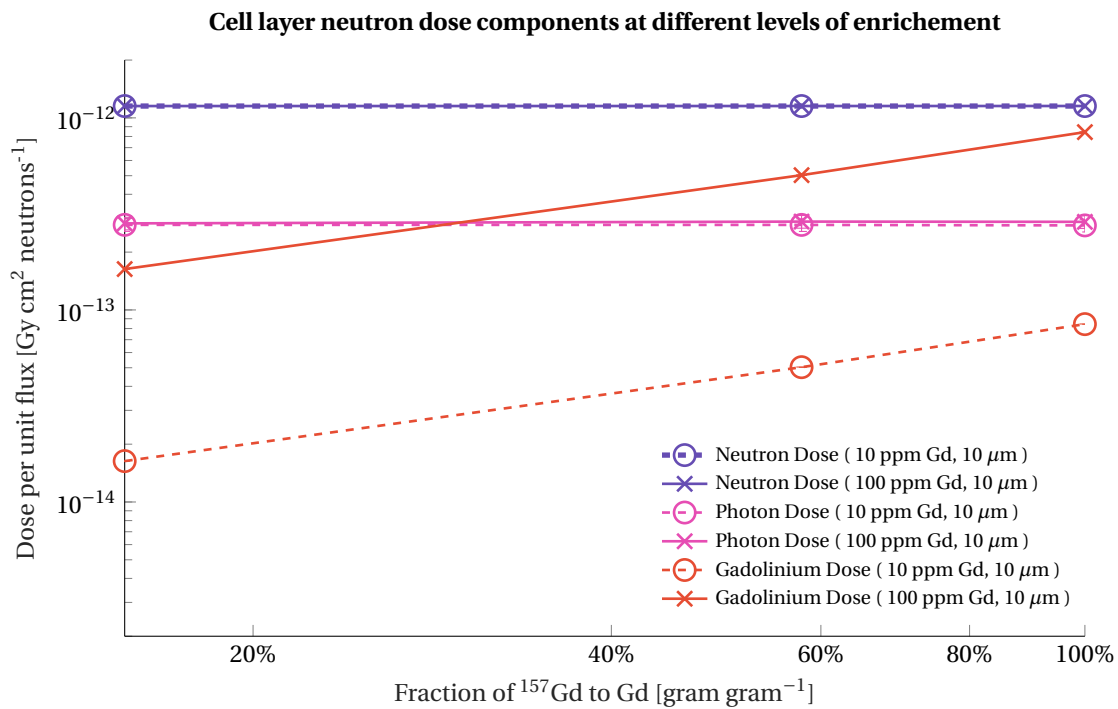
Figure 6.4: Neutron dose components in the cell layer evaluated for a range of enrichment levels for different concentrations. All dose components, except for that caused by the neutron capture reaction self, seem independent of the ^{157}Gd enrichment level.

The third parameter investigated was the thickness of the cell layer. The LNCaP cell line can be grown on a flat surface where they could overlap [10]. In a dense cell culture it is assumed that these cells are nestled close enough to one and other that this whole layer can be approximated by a solid slab of 10 μm. However, since these overlapping cells might be present, it is not clear what the best slab thickness is that best approximates the cell layer. Therefore, this third parameter was not included as a design parameter but rather as an unknown variable. In Figure 6.5 the effect is of the thickness of the cell layer on the calculated dose components is shown. It is visible that this effect is less strong than that of the other parameters in the evaluated ranges. However, we see that this uncertainty in the optimal approximation of the layer thickness does translate to an uncertainty in the dose due to neutron capture electrons.

From these observations the following model was derived that captures the dose due to the electrons produced in gadolinium neutron capture:

$$\dot{D}_{\text{Gd-electrons}}^{\text{cell layer}} = c_{\text{Gd}} \cdot (a_1 \cdot F + a_2) \cdot (a_3 \cdot W + a_4) \cdot \Phi_n. \tag{6.1}$$

Here, the dose rate $\dot{D}_{\text{Gd-electrons}}^{\text{cell layer}}$ (in Gy s^{-1}) is expressed by the gadolinium concentration c_{Gd} (in g/g), the enriched fraction F, the width of the cell layer W (in μm), the incident neutron flux Φ_n (in neutrons cm^{-2} s^{-1}) and a few fitting parameters. This model was then fitted to the data using a least squares approach, using the Levenberg-Marquardt optimisation algorithm. Since in low concentration regions the *absolute* change in dose achieved by tuning parameters (other than concentration) is low, the least squares cost function will put more weight on measurements performed with higher concentrations. To overcome this the actual fit was performed on the relative dose per concentration unit and per neutron flux. This was stated as

$$\frac{\dot{D}_{\text{Gd-electrons}}^{\text{cell layer}}}{c_{\text{Gd}} \cdot \Phi_n} = (a_1 \cdot F + a_2) \cdot (a_3 \cdot W + a_4). \tag{6.2}$$

The fitted parameters are; a_1: 0.8123, a_2: 0.1951, a_3: $3.567 \cdot 10^{-10}$ and a_4: $4.806 \cdot 10^{-9}$. R-square and the Adjusted R-square were both found to be 0.9999. However, this interpolation model is only valid in the range of the specified parameters.
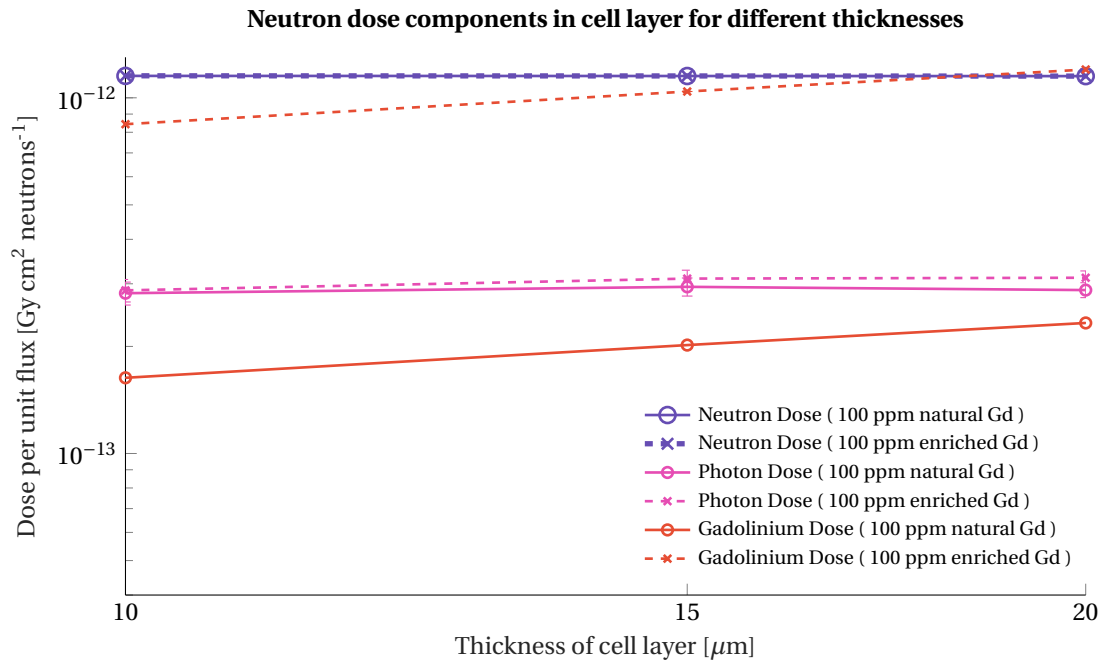
Figure 6.5: Neutron dose components in the cell layer evaluated for a range of thicknesses for different enrichment levels. All dose components, except for that caused by the neutron capture reaction itself, seem independent of the thickness of the cell layer.

The neutron kerma in the cell layer per unit flux was $1.1516 \cdot 10^{-12} \pm 7.0738 \cdot 10^{-16}$ Gy cm^2 neutron^{-1} regardless of which parameters are used. The variance between different evaluations for different parameters is as large as the average Monte Carlo standard deviations present in the outcomes.

The photon dose in the cell layer per unit flux was $2.8831 \cdot 10^{-13} \pm 1.7580 \cdot 10^{-14}$ Gy cm^2 neutron^{-1}. Here the Monte Carlo variance does not explain these fluctuations seen in Figure 6.5 meaning this dose component is not completely independent. However, it is an adequate approximation for the purposes of a fast method to estimate the effect of parameter changes during the design phase of this experiment.

For the contaminating gammas, the photon dose was found to be $1.7205 \cdot 10^{-12} \pm 4.7722 \cdot 10^{-14}$ Gy cm^2 photon^{-1}. Here too, the deviations were outweighed by the Monte Carlo variance.

For the Petten beam, the value for the neutron flux Φ_n needed in Equation is $3.92 \cdot 10^6$ cm^{-2}s^{-1}. For the Delft beam the value to be used in Equation for the neutron flux Φ_n is $2.7 \cdot 10^7$ cm^{-2}s^{-1}.

Since the geometry of the material is so thin, many of the internal conversion electrons are believed to exit the plane. Therefore the extra observed biological effect due to the $\dot{D}_{\text{Gd-electrons}}^{\text{cell layer}}$ could be used to approximate the CBE for just the internal gadolinium electrons. However, due to the timing of this thesis and the experiment, data from the experiments were not used. All doses were calculated as physical/absorbed doses.

<div style="text-align: right; font-size: 3em;">7</div>

GdNCT Treatment planning

7.1. Patient description

For treatment simulation, a phantom is needed with the material composition and geometry of the patient. In practical applications, such a material composition and geometry could be derived from registered CT and MRI images taken from the actual patient. From those, the material composition, including gadolinium concentration could be measured per voxel due to the contrast that gadolinium adds to the MRI image. A simple recipe could then be applied to estimate the tumorous mass fraction and the leakage factor from the gadolinium concentration per voxel.

As we do not have a patient, but rather a predefined phantom, the imaging stage is skipped and the gadolinium concentration per voxel has to be calculated slightly differently. For this chapter phantom A was used. As phantom A is described using simple geometric shapes and not in voxels, a method is needed to transform this description into voxelised tumorous mass fractions and leakage factors, analogous to "imaging" the phantom. To simulate the imaging of the phantom, Monte Carlo sampling is used. Random points in each voxel are checked for being in or outside the geometric shapes describing the tumour and metastasis. The fraction of points within the tumour is an estimator for the volume fraction of the tumour tissue in the voxel from which the necessary parameters can be determined. In phantom A, the bulk tumour in the prostate was defined to have a tumour density of 50%, where half of its cells to contain gadolinium at 700 ppm which was modelled as an effective concentration of 350 ppm. Together with the volume fraction that the tumour spheres occupy in the voxel, these densities can be used to determine the tumorous mass ratio per voxel needed to adjust the absorbed doses from the MCNP n-γ calculation. This random sampling of the geometry to determine the gadolinium concentration effectively simulates MRI to obtain the gadolinium concentration per voxel, only more accurate as it is a direct resampling of the ground truth. The healthy mass fraction was determined in this way as well.

For the voxels' tumours mass fractions a reasonable approximation is assumed to be a spherical distribution of these tumour cells within the voxels similar to Figure 5.2 (f)-(j). Using the look-up table as proposed in Chapter 5, the fraction of energy leaking out of the tumorous regions into the non-tumorous regions is interpolated for each voxel.

Each relevant organ at risk was delineated using simple geometric shapes which through Monte Carlo sampling was voxelised similarly as was done for the gadolinium concentration. Each voxel could in theory contain fractional amounts of an organ's tissue, which is allowed by the treatment planning method described in this chapter. This was done for a crude model of the bladder and rectum. Here the bladder was modelled as a sphere elevated above the prostate on the front end of the phantom, just touching the prostate. The rectum was modelled as an oval cilinder extending the full phantom also toughing the prostate. The remaining tissue was also treated as a separate organ such that for each voxel all organ mass fractions would count up to 1. These delineations are visualised in Figure 7.1.

In summary, the dummy patient is now fully described in a voxel based model which would also be possible with an actual patient. For each voxel, the fraction of non-tumorous and tumorous cells is known or could be estimated. In addition, the fraction of each organ in each voxel is known. Further it has been assumed that these fractions behave independently of each other. If, for example, 50% of a voxel containing
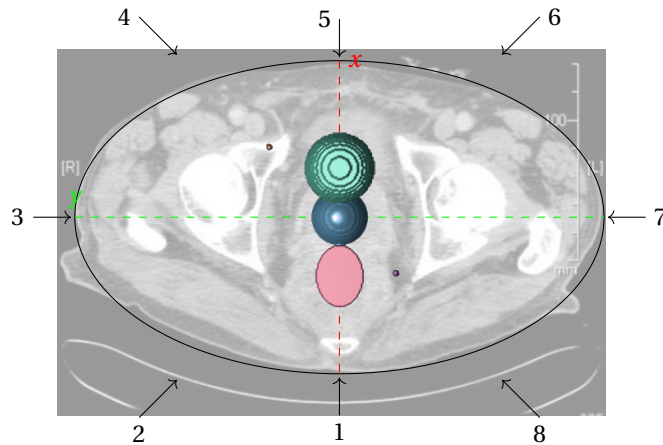
Figure 7.1: Top view of material description phantom A, overlaid on a CT scan [1] similarly as shown in Figure 4.1. Overlaid are isocontours of the delineations of the organs at risk: the bladder (green) and rectum (pink) in an overlaid voxel mesh identical to the dose deposition voxel mesh. In addition, an iso-surface of the gadolinium concentrations on the simulated MRI data is displayed, showing the main tumour (blue) and the metastasis (purple and orange). The arrows indicate the neutron beams centre axes with radii of 5 cm.

multiple organs is considered tumorous, so is each fraction of organ in that voxel assumed to contain 50% tumorous cells. In theory this could be improved upon by using the correct a-priory chances of each tissue type to contain tumour cells and using Bayesian logic to update these chances using the evidence as found by the MRI scan. However, this is a good enough approximation for the scope of this thesis.

7.2. Multi scale dose calculation

Macro scale dose calculation   The dose calculations on the patient geometriy were performed as explained in Chapter 4. This was done for all 8 different beam orientations as portrayed in Figure 4.1. Each beam orientation was simulated independently with neutrons from all of 40 different energy groups that were chosen logarithmically. This resulted in 320 different beam simulations or *beamlets* of which only the neutron and photon components as given by MCNP were known. Using the post-processing steps explained in Chapter 4, these were converted to contain all dose components, corrected for the lack of electron transport.

Micro scale dose calculation   For the 320 beamlets the dose components were converted into two doses, the total physical dose that a non-tumorous cell cluster would receive and the total physical dose that a tumorous cell cluster would receive in each voxel. This was done using the method as described in Chapter 5.

Cell scale dose calculation   As the data to convert these absorbed doses into equivalent or effective doses was not yet available for the gadolinium electrons, no conversions have been done. If in the future, these values become available for all significant radiation components, then the treatment planning could be performed using prescribed biological effect rather than prescribed physical doses.

7.3. Multi scale dose prescription without the traditional target volumes

In traditional treatment planning, one would use delineated target volumes for which a dose is prescribed. Such target volumes need to take into account patient movement relative to the photon or proton beam. The treatment optimisation is then performed to find a treatment that does not under- or overdose this target volume too much while minimising the dose outside the target.

However, as GdNCT is chemically targeted and the neutron beam is very wide due to scattering, patient movements are of less concern. In addition, we don't want all voxels in the prostate to receive the same dose as each voxel might contain different amounts of tumorous tissue and therefore gadolinium. We do however, want all the tumour cells in the prostate to receive a minimal dose. Therefore in a potential cost function we

can use a measure on the PSMA positive calculated dose weighed by the fraction of PSMA positive cells in the voxel and combine it with a measure of the dose to the PSMA negative cells which we want to receive zero dose.

Furthermore, in traditional radiotherapy, no overdosing of the tumour is wanted. This is a precaution to protect healthy cells surrounding the tumour cells such that the prostate itself retains some functionality. However, in Gd-PSMA NCT we could put a lower bound on the PSMA positive dose in all voxels where a significant amount of gadolinium is detected and penalise the PSMA negative dose in all voxels weighted by their PSMA negative fraction. These penalisations could be set on the non-tumorous cells in each organ separately.

Although GdNCT is able to provide divergent doses to both healthy and tumorous cells within a voxel, these doses are still strongly correlated and in the most extreme cases are less then 15% apart. This makes putting constraints on both the minimal tumour dose and the maximal healthy prostate dose tricky. As in this thesis, the healthy part of the prostate falls within the organ at risk group "other" it is chosen to only constrain the 95th percentile of the voxel doses in this organ at risk group such that the prostate, healthy lymph nodes and a margin could receive higher doses. Both the bladder and rectum lie in near vicinity to the prostate, here as well a percentile is used to allow part of these organs to receive higher dose.

7.4. Treatment optimisation

The method with separate treatment of tumorous and non-tumorous cells in the same voxels allows us to define a cost function that only penalises excess dose to non-tumorous cells while rewarding dose to tumorous cells. In traditional radiotherapy, over-dosing of the tumour *is* penalised to indirectly penalise the dose to healthy cells within the traditional planning target volume. Tumour dose reward should be given up to the prescribed dose whereafter the reward drops to zero. Alternatively, the reward could be the based on the actual tumour control probabilities. Different weights can be set for the different organs and tumour to reduce dose in more sensitive organs.

As this is a novel approach, it is not known yet if clinically standard used constraints could be satisfied with any combination of the beamlets. To evaluate the kinds of treatment plans that are obtainable with this modality, most constraints that are used in traditional treatment planning are therefore left out. Solely upper constraints on the dose histograms of several organs at risk are used in this treatment plan. The 90th percentile of the voxel doses in the bladder must not exceed 20 Gy. The 90th percentile of the voxel doses in the rectum must not exceed 20 Gy. The 95th percentile of the voxel doses in parts of the body other than the bladder or rectum must not exceed 20 Gy. These constraints can easily be satisfied at initialisation by choosing low beam weights. To promote high tumour dose in this explorative GdNCT treatment plan a cost function is used.

The generalised cost function as was used in this thesis is displayed in Equation 7.1.

$$\text{cost} = \sum_{o \in \{\text{bladder,rectum,other,...}\}} \left(w_o \sum_{v \in \{1,...,N_v\}} F_o(v) \cdot P^-(v) \cdot D^-(v)^2 \right) + \left(w_t \sum_{v = \text{voxels}} P^+(v) \cdot \max(0, S - D^+(v))^2 \right)$$

(7.1)

In Equation 7.1, the cost is defined by summing the costs for each organ o and tumour t, weighted by the organs weight w_o and tumours weight w_t respectively. For each of those organs, the cost is build up of all the doses $D^-(v)$ received by the healthy cells in all the voxels v weighted by the actual fraction $F_o(v)$ the voxel is occupied by the organ multiplied by the fraction $P^-(v)$ of how much of that voxel contains PSMA negative cells. The tumour dose is similarly penalised by using the tumour dose $D^+(v)$ to penalise any under dose below the prescribed dose S for each tumorous voxel, weighted by the actual fraction of PSMA positive cells $P^+(v)$ in those voxels.

In the initial explorative treatment plan we first want to evaluate whether a sufficient therapeutic dose to the tumour is obtainable while satisfying a minimal number of constraints that unsure the patients survival. This forms the basis requirement for a prostate irradiation modality. This is tested by using zero weight for all organ weights w_o and unit weight for the tumour weight w_t as regularisation of the dose in healthy tissue is not wanted for now. In addition, a prescribed dose S of 40 Gy is chosen to challenge the modality.

For each beam and energy combination, a beamlet has been pre calculated, the intensities of each of the 320 beamlets were used as variables to be optimised. This is analogous to proton therapy were one can first chose an energy and direction that would reach the required depth and later in a different step figure out how

to actually obtain that energy and direction. Whether this also works for neutron therapy was investigated in the remaining of this chapter.

The accompanied contaminating gamma beamlets have been calculated as well for all 8 beam positions in 10 energy groups. Although, these were not used as giving the optimiser control over these gammas is not realistic as it would then approximate photon therapy. Instead the gammas are a consequence of the neutrons, depending on how they are filtered to obtain the preferred spectrums which are yet to be calculated in this chapter. This "spectrum first, filter later" approach can therefore not provide any information about the background dose due to contaminating gammas. In addition, the "spectrum first, filter later" approach can also not predict treatment time as this would heavily depend on the number of neutrons passing to the filter to be designed later.

Similarly to holding back the photon beamlets from the optimisation algorithm, one could also argue that the fast neutrons are rather a contamination than a tuneable energy in most neutron spectra and therefore should also not been given control over. However, the choice was made to give the algorithm complete control over all the 40 energy groups as any regularisation on the neutron spectrum would be arbitrary as the source spectrum and filtering thereof are to be determined afterwards as is done in proton therapy.

The optimisation of these 320 parameters was done using the interior-point algorithm. In MatLab's standard optimisation toolbox, this can be implemented using the `fmincon` function in which constraints are allowed. A lower bound of zeros was put on all the beam weights, as negative doses are not possible.

All beamlets representing the 3D dose distribution due to a specific beam and energy combination were converted into 1D vectors. Voxels with zero dose in each of the beamlets were removed from all beamlet vectors to speed up calculations. All the delineated organs and tumour fractions were converted to vectors as well and had their vector elements discarded to match the dose deposition vectors.

The total dose distribution vector was calculated at each iteration by multiplying the correct beam and energy weights with the respective dose distribution beamlet. The sum of all these weighted beamlets then is the approximation of the dose distribution. This dose distribution was then used to check the constraints and to calculate the cost function on.

7.5. Resulting treatment plan

The beamlets as were calculated for this specific phantom were preprocessed as explained in Chapter 4, with just over 1 minute of CPU time per beamlet.

During the optimisation is was necessary to hold more than 40 GB worth of uncompressed beamlets in memory. Combined with overhead this formed a problematic memory load and the decision was made to downsample all the post-processed beamlets and patient descriptions by a factor two in each dimension, yielding a more manageable memory load of 5 GB. After optimisation of the beamlet weights, the result is upscaled again using the original beamlets.

After 300 CPU hours and 468510 function evaluations, the optimisation was terminated due to reaching the maximal number of iterations. During the whole optimisation, constraints where kept satisfied within a small tolerance and the cost decreased steadily at each iteration but could do so further given more iterations. The treatment plan resulting from this is a valid one that is presumably close to optimal although it is unclear how much it could have improved given more computation time. The inability of this algorithm to find the global optimum is due to the limited computational budget and the inefficient optimiser chosen for this task. As at each iteration, the gradient was calculated numerically using one function evaluation per input dimension instead of performing more efficient stochastic gradient descent.

The resulting dose distribution of this treatment plan is visualised in Figure 7.3 for the central plane in the phantom and for a lower plane holding the metastasis. Figure 7.2 shows the 8 different spectra that were optimised which correspond to the dose distributions shown in Figure 7.3. In the thermal to epi-thermal neutron range, the chosen spectra are fairly regulated without explicit regularisation during optimisation. However, the optimisation algorithm is very specific as to which energies do and which energies do not contribute enough in the fast neutron range. The fast neutron beamlets were included because they were expected as a contaminating fraction of the input spectrum, however without any constraints the algorithm fully takes advantage of these energies. Figure 7.3 shows that neutron collimators could have reduced the number of fast neutrons that missed the tumours, however this treatment modality was not meant to rely on fast neutrons this much. This raises the question, whether these spectra are viable and realistic or not. In Chapter
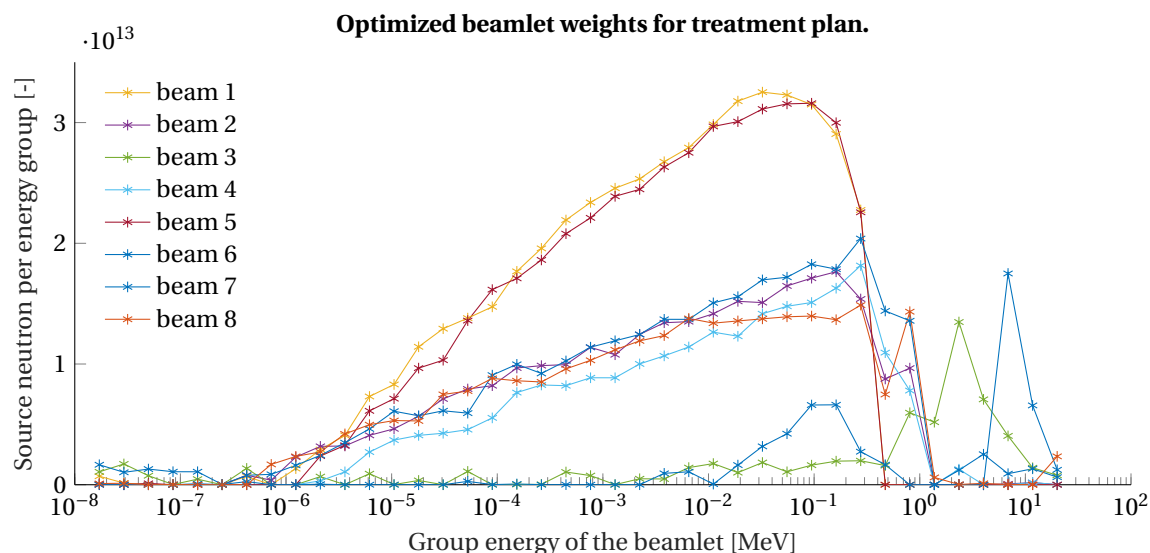
Figure 7.2: The 8 optimised spectra of the beams shown in Figure 7.1. The problem is nearly symmetric aside from the metastases, this symmetry is also visible in the resemblance of opposite beam spectra. Most prominent in the thermal to epi-thermal range are beams 1 and 5 which travel the shortest distances to the tumour. The longer ranges require faster neutrons.

8, the viability of these spectra given a reactor source is assessed using a novel neutron filter optimisation algorithm.

A total of $2.10 \cdot 10^{15}$ source neutrons were present in the beamweights which yields a treatment time of 1 hour if the neutron beams could deliver the spectra at a flux of $7.4 \cdot 10^9$ neutrons cm^{-2} s^{-1}.

The dose distribution per voxel is known for the tumour cells within the voxel and the healthy cells. The bulk tumour, contained 700 ppm of ^{157}Gd at a tumour cell density of 50%. Tumour cell dose in the bulk tumour ranged between 25 - 31 Gy while this was 24 - 30 Gy for the healthy cells within the same region, averaging at a dose differentiation of about 2% near the center of the bulk tumour and 6% near the edge. In the metastasis the tumour density was 100% and the doses to healthy cells have no significance there but they do form a good indication of what would happen to a cluster of healthy cells. In the shallower metastasis (Figure 7.3 B), the peak tumour cell dose was 38.0 Gy and the theoretical peak dose to healthy cells in that region was 21.8 Gy with dose differentiations up to 74%. In the deeper metastasis (Figure 7.3 A), the peak tumour cell dose was 34.8 Gy and the theoretical peak dose to healthy cells in that region was 21.5 Gy with dose differentiations up to 62%. Profiles through the tumours showing the dose differentiation are plotted in Figure 7.4. The 90th percentile of the doses to the organs at risk were pushed up to the limit put by the constraints of 20 Gy.

Dose distribution at prostate pane.   **Dose distribution at metastasis pane.**
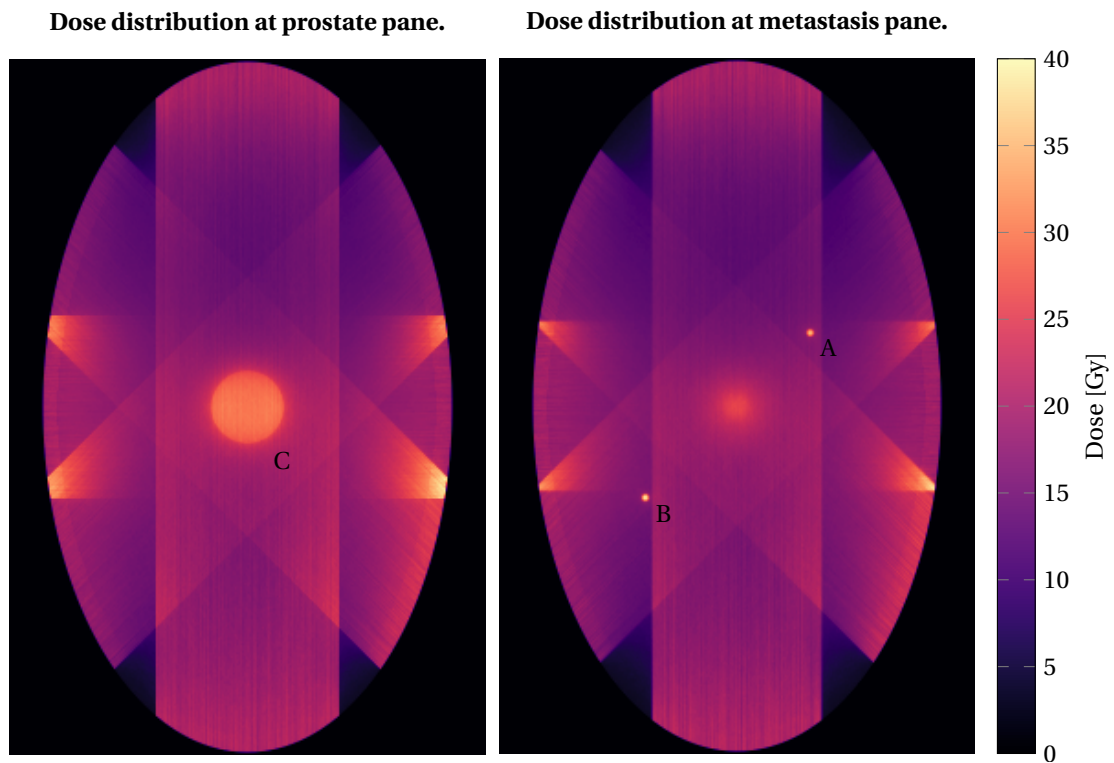
Figure 7.3: The resulting treatment plan. The image shows the dose components after post-processing. For the gadolinium dependent dose components the dose as is received in tumour cells is shown, i.e. inside tumour regions the dose shown is to tumour cells, outside it the dose shown is to healthy cells. Metastases (A) and (B) contained 700 ppm of ^{157}Gd at a tumour cell density of 100% and received respectively a peak dose of about 38.0 Gy and 34.8 Gy. The bulk tumour (C) containing 700 ppm of ^{157}Gd at a tumour cell density of 50% received a dose of about 25 Gy to 31 Gy in the tumour cells. The presence of fast neutrons is observed in the straightness of the neutron beams and the lack of beam widening. All doses are absorbed doses.
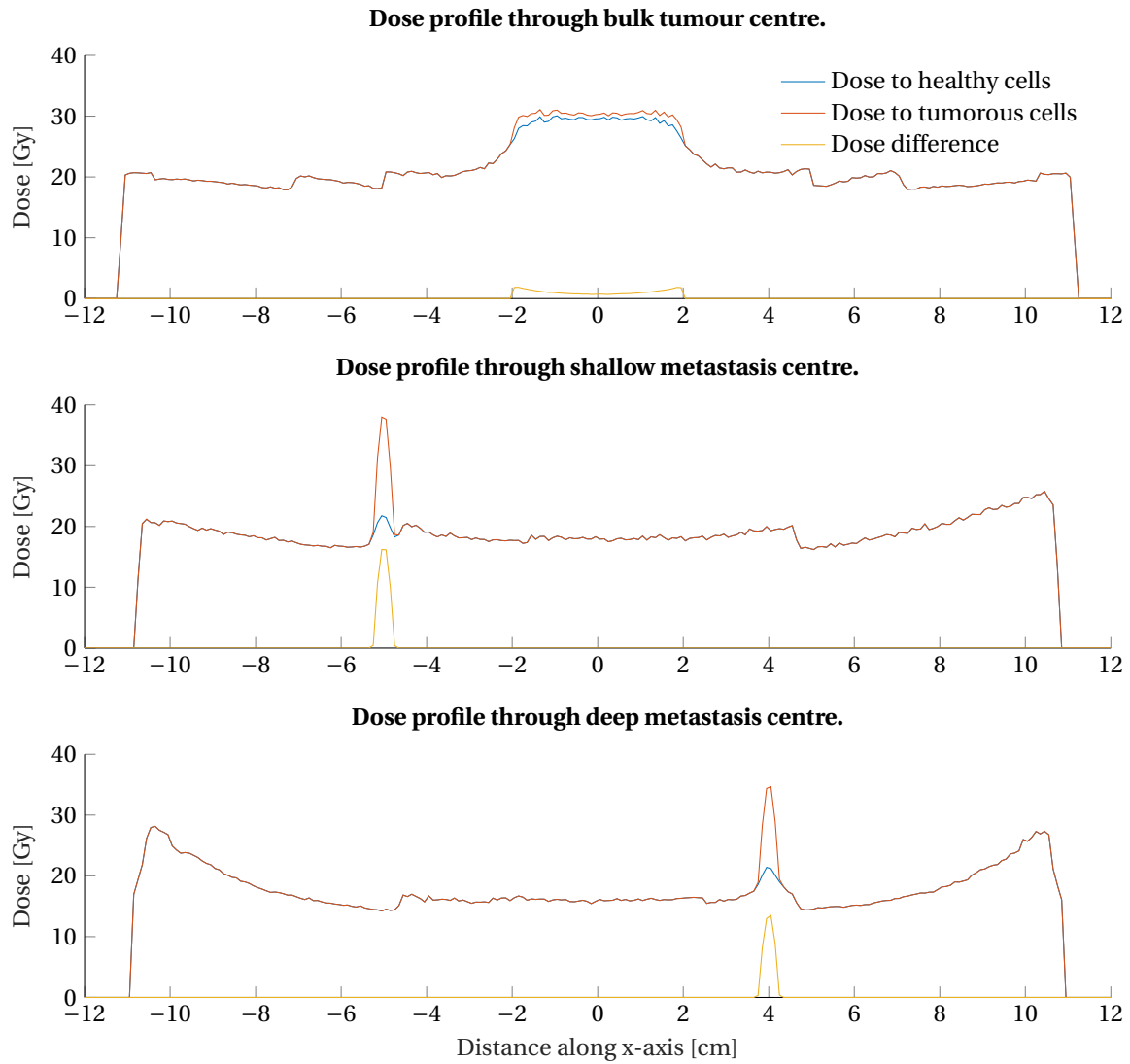
Figure 7.4: Off-axis profiles, parallel to the x-axis, through the metastases and bulk tumour. The bulk tumour, contained 700 ppm of ^{157}Gd at a tumour cell density of 50%. In the metastasis the tumour density was 100% and the doses to healthy cells have no significance there but they do form a good indication of what would happen to a cluster of healthy cells. All doses are absorbed doses.

8
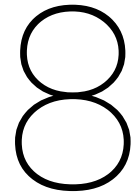
Neutron filter approximation and optimisation

8.1. Neutron filter bank model

For this chapter the goal was to find a neutron filter that yields a outputted spectrum best approximating the optimal neutron spectrum as found in Chapter 7.

The theoretical setup for the neutron filter consists of a holder in which various thicknesses of slabs can be placed perpendicular to the incident neutron beam. These slabs are made of typical neutron filter materials and can be placed in any order that is allowed by the constraints. Each slab's material has different properties with respect to neutrons. Some materials capture low energy neutrons while letting through higher energy ones. Other materials can lower the energy through elastic scattering. It is assumed that enough slabs are available to fill up the slab holder of arbitrary length. An example of such a filled holder is visualised in Figure 8.1. In the figure it is visualised that this method assumes a large homogenous incident neutron beam where after filtering a final collimator is used to shape the beam.

The problem is to find which slabs and in what order these slabs are needed in the holder such that the filtered beam maximises some cost function under some constraints. The input to optimise is a variable length list of integers, each ranging from 1 to the number of slabs. This list represents all the slabs with the number denoting which type of slab is used. Spaces between the slabs can be modelled as air or vacuum slabs. Each type of slab is allowed to have its own thickness and could even consist itself of different layers of materials.

source neutrons   fitlered neutrons
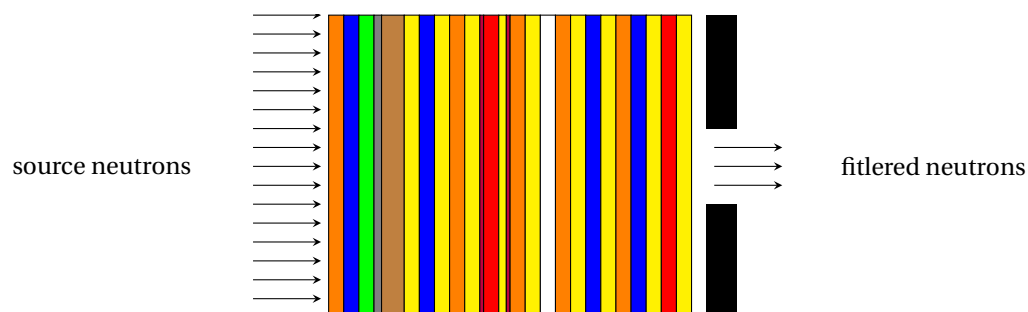
Figure 8.1: A large homogenous incident neutron beam from the left travels through the filter bank, through each slab and through the final collimator. Many neutrons as absorbed, scattered away or slowed down. The filtered neutrons will have a more favourable spectrum than the incident source neutrons.

8.2. Optimisation

To optimise the sequence of slabs, multi-start simulated annealing is used. While simulated annealing is good at finding global maxima, the search space is so vast that multiple tries were necessary. Therefore the simulated annealing is performed with multiple starting points of which the best result is chosen as the final solution.

In each time step in simulated annealing, the list of integers is changed using a few randomly sampled swaps, insertions or deletions resulting in a few solutions closely neighbouring the current accepted solution in the permutation space. This resulting neighbouring solution is then checked for the constraints and rejected or changed accordingly. These constraints on the filter itself could include an upper or lower limit on the number of slabs or fixing the final slab material to lead thereby blocking some contaminating photons. Although, direct constraints on the inputed slabs were not included in this thesis.

The assessment of the new list of integers is done by calculating the outputted spectrum using an efficient approximation further detailed in Section 8.3, after which a cost is assigned to the output spectrum using a cost function. The cost function consisted of the squared differences of the outputted spectrum and the target spectrum after normalisation. For this thesis the only constraint used was, the integrated flux after filtering must not be lower than 3% of the flux before the filter. In addition, the integrated flux was penalised as well in the cost function. The convention in simulated annealing imposes a score rather than a cost, this is achieved by defining the score as the reciprocal of the cost.

At each time step, if an improvement in the score is made compared to the current accepted solution, the new solution is accepted as the current solution with 100% probability. When a constraint is not met, the score is put to zero and the solution is never accepted. If however, the cost is worse than the current accepted solution but the constraints have been met, there is a probability P_{accept} that the algorithm still accepts the solution. This probability along with those in other cases is given by Equation 8.1.

$$P_{\text{accept}}(s', s, T) = \begin{cases} 1 & s > s' \\ \exp\left(-\frac{(1-s/s')^2}{T}\right) \text{ with } T = \frac{1}{i} & 0 < s \le s' \\ 0 & s = 0 \end{cases} \tag{8.1}$$

In Equation 8.1, the probability P_{accept} is expressed by the current score s', the candidate score s and the temperature T. This temperature is a naming convention originating from the first use of simulated annealing, it is a parameter that controls the trade-off between exploration and fine-tuning. For this thesis, this parameter was based on the iteration number i, such that the algorithm begins exploring and finishes with fine-tuning. For low temperatures, simulated annealing approximates a stochastic gradient decent algorithm.

8.3. Fast filter estimation using transmission matrices

8.3.1. Transmission matrix

To provide a fast method of estimating the filtered output spectrum given a filter bank, a linear system is set up. Here the neutron energy is discretised and each slab type is represented by a transmission matrix $\boldsymbol{T}$. The elements of $\boldsymbol{T}$, denoted with T_{ij} are calculated in Monte Carlo simulations where T_{ij} represents how many neutrons are expected to exit the slab with an energy in energy group j per neutron entering the slab at an energy from group i. Filling row i only requires one Monte Carlo simulation with the number of particles proportional to the number of energy levels as all particles exiting the slab will arrive in one of the energy columns. The total number of Monte Carlo simulations equals the number of energy levels as well. Therefore the computation time per transmission matrix is proportional with the number of energy levels squared. For 1000 energy levels, the calculation time for an average slab was 105 minutes using $1 \cdot 10^6$ source particles in MCNP 6 running on 6 cores. Due to the fast calculations of 6 seconds and large overhead, the added cores were of little benefit compared to using a single core. Each slab has to be calculated only once after which the transmission matrix can be used for every filter problem there after.

As materials often block some energies partly or scatter the neutrons down in energy, the transmission matrix will see higher values on the diagonal and below it towards lower output energies. However, low energetic neutrons could by the temperature of the surrounding increase their temperature and therefore upscatter. Moderating materials have a wide distribution of their transmission matrix while simple materials such as aluminium have very sparse and almost diagonal matrices. The information across the diagonal of
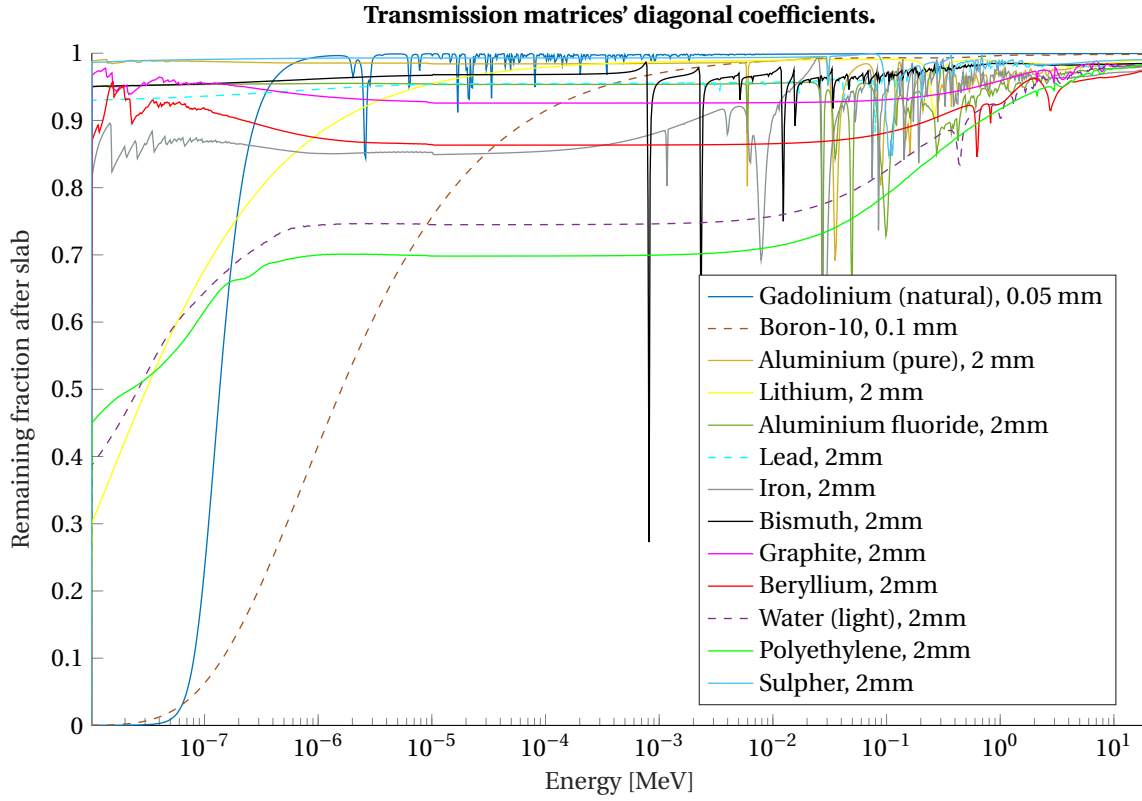
Figure 8.2: Diagonal components of the transmission matrix of several slabs of different materials. The diagonal of these transmission matrices contain most of the information in the whole matrix. Seen is that Bismuth, for example, has some narrow energy bands for which it has a very low transmission rate.

the transmission matrix characterises how much of a certain energy is let through or transmitted. For a few materials and slabs this diagonal is plotted in Figure 8.2. The full transmission matrix for light water and aluminium, is visualised in Figure 8.3.

8.3.2. Transmission matrix multiplication

Using the same number discretised energy levels N, the input spectrum is represented in a vector $\vec{S}_0$ of size $1 \times N$. We calculate spectrum $\vec{S}_1$ following the first slab characterised by the transmission matrix $\boldsymbol{T_0}$ as a linear combination of that slabs responses to each energy group in our energy set weighted by how much that energy was present in the input flux: $\vec{S}_1 = \sum_{i=1}^{N} S_{0,i} \cdot \vec{T}_i$ with $S_{1,j} = \sum_{i=1}^{N} S_{0,i} \cdot T_{ij}$ which essentially equals the matrix multiplication $\vec{S}_1 = \vec{S}_0 \boldsymbol{T}$.

A following slab would no longer see the input flux $\vec{S}_0$ but instead the flux $\vec{S}_1$ which it would filter to obtain the spectrum $\vec{S}_2$. This process can be generalised to $\vec{S}_{k+1} = \vec{S}_k \boldsymbol{T_k}$ where $\boldsymbol{T_k}$ denotes the transmission matrix describing the kth slab.

Since the grouping of matrices in a multiplication chain does not affect the outcome the total transmission matrix of a system of slabs could be calculated once and applied to many input spectra thereafter: $\boldsymbol{T}_{\text{total}} = \prod_k \boldsymbol{T_k}$.

Furthermore, computational optimisations are possible by grouping adjacent slabs with equal transmission matrices together and calculating their integer powers. For example, eight adjacent matrices (seven multiplications) could be optimised to three consecutive squares of that matrix (three multiplications).

As a validation, the total transmission matrix $\boldsymbol{T}_{\text{total}}$ for a set of 25 slabs was calculated in two ways. First by using the matrix multiplication of the respective 25 matrices, second by simulating the transmission matrix for the combined slabs as one single slab, in the same manner as was done for each individual slab. In Figure 8.4, both total transmission matrices are displayed. In Figure 8.5, one sees these transmission matrices applied on a dummy spectrum for comparison. The build up of errors in the total transmission matrix are in
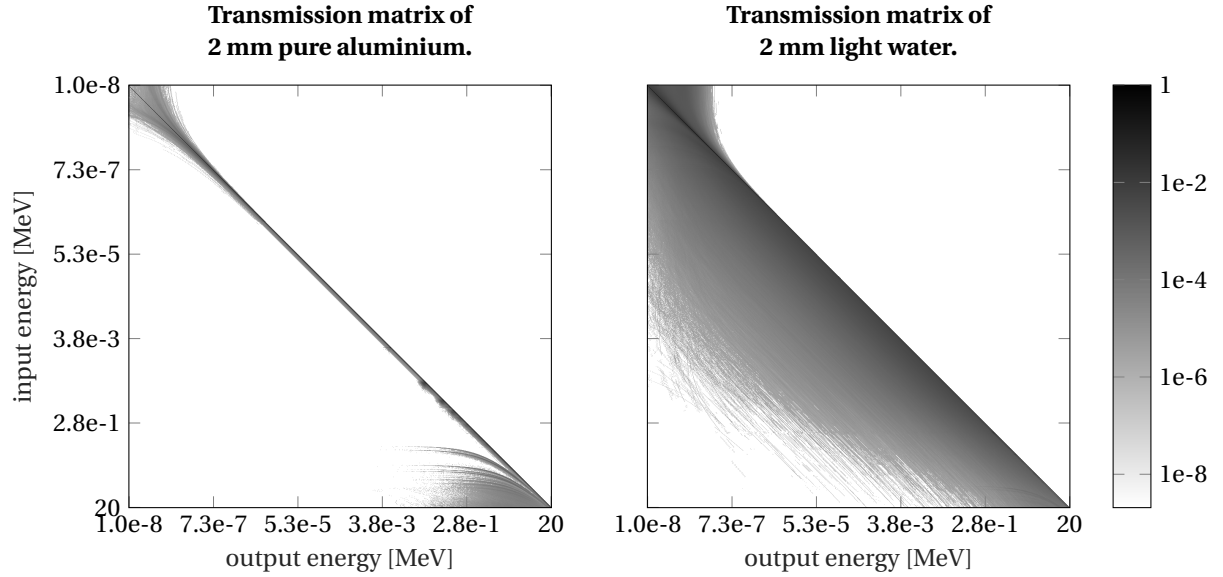
Figure 8.3: Transmission matrix of aluminium and light water in a logarithmic scale. It is visible that for a given energy of the incident neutrons, the light water slab outputs a much wider spectrum than the aluminium slab. Due to the fact that the transmission matrices are not completely diagonal, the actual orders of them matters in the multiplication chain as explained in Section 8.3.2.

part due the build up of angular deviation most prominent in lower energetic neutrons, increasing their path length through the filter slabs thus increasing their attenuation.

In the validation that was performed with an equal amount of source particles as in the slab calculations, it is visible that the transmission matrix is not completely accurate. The added effect of these matrix multiplications therefore is that where in multiple slabs particles get lost or captured, these particles no longer contribute to the final spectrum while for single slabs more particles get taken into account for the final spectrum. This yields that, for example, the transmission matrix of 1mm lead to the 10th power will yield an equivalent effective transmission matrix than for 1 cm lead, but with less variance then when actually simulating the full 1 cm. This however, gets overshadowed by the decrease in accuracy by the build up of angular errors.

8.3.3. Angle corrected transmission matrices

The transmission matrices neglects angular deviations. If a neutron travels at an angle of 10 degrees with respect to the axis it is implicitly changed back to 0 degrees at the next transmission matrix as these matrixes are obtained at perpendicular neutron beams. The path length of these neutrons are therefore underestimated, thus overestimating the final flux and how forward peaked the output spectrum is. Although not implemented in this thesis, some thoughts on how to improve on this are stated in this section.

To overcome one of these angle related problems it is also possible to define the transmission matrix elements as T_{ijkl} where the yield of neutrons exiting at an angle in group l with energy in group j relative to the number of incident neutrons of energy group i with an angle in group k is determined. In order to still have the ability of chaining these matrices in multiplication chains they could be collapsed and redefined as $T_{mp} = T_{(i,k),(j,l)}$ where m and p are indexes that point to a list of all possible (i,k) and (j,l) combinations respectively. The increase in initial computation time would scale proportional to the number of angle bins or the number of angle bins squared depending on how good the statistics of the bins need to be. If the accuracy of thermal neutrons is desired then this extra computationally heavy improvement could provide that extra accuracy.

A second problem is the dispersion of the neutron beam. If the incident neutron beam is not an infinite plate source as is assumed here, the scattering of neutrons causes beam widening, which will be blocked by the final beam collimator. The flux of these scattered neutrons might then be overestimated if not accounting for that.
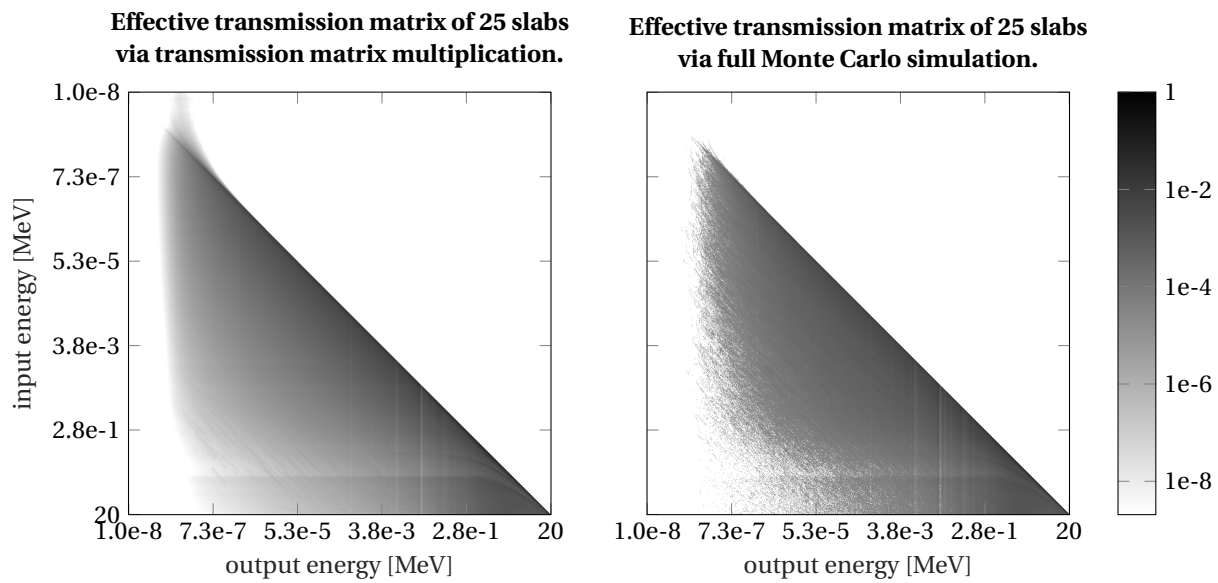
Figure 8.4: Effective transmission matrix of a sequence of 25 slabs. One has been calculated using the respective 25 transmission matrices while the other has been calculated in a Monte Carlo simulation, similarly as a single slab would have been with equal amounts of source particles.
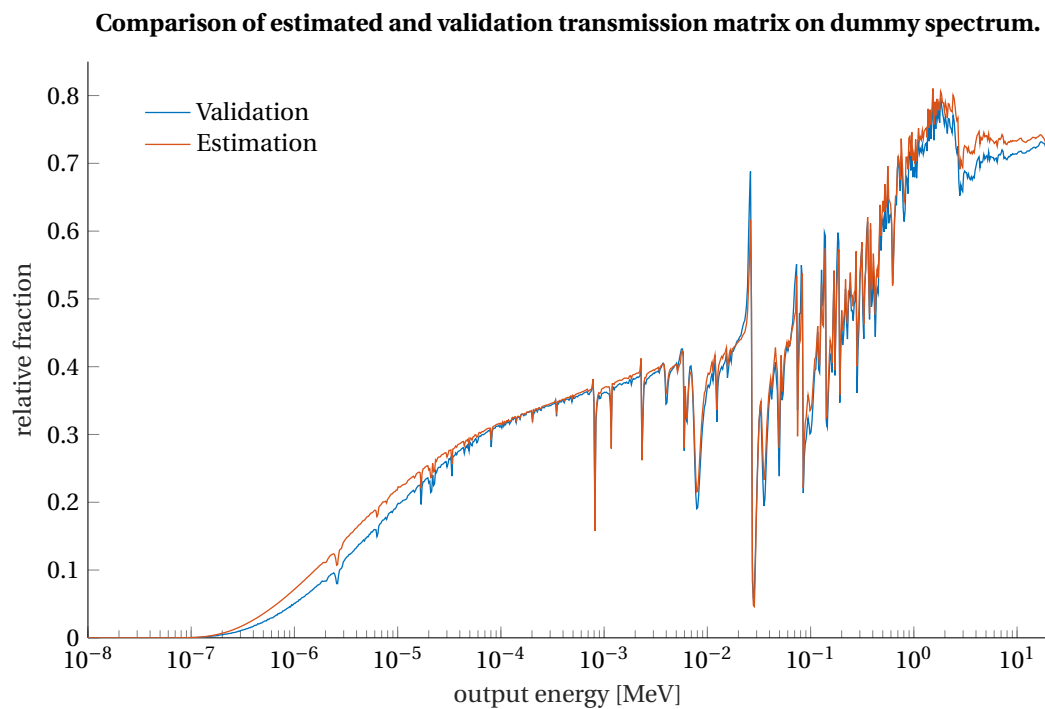
Figure 8.5: Both the estimated and calculated effective transmission matrices applied on a dummy spectrum. Seen is that most regions have been approximated very well. However, at some energies a discrepancy is visible. The dummy spectrum consisted of neutrons from every energy group in equal amounts.

Score evolution of simulated annealing process during filter optimisation.
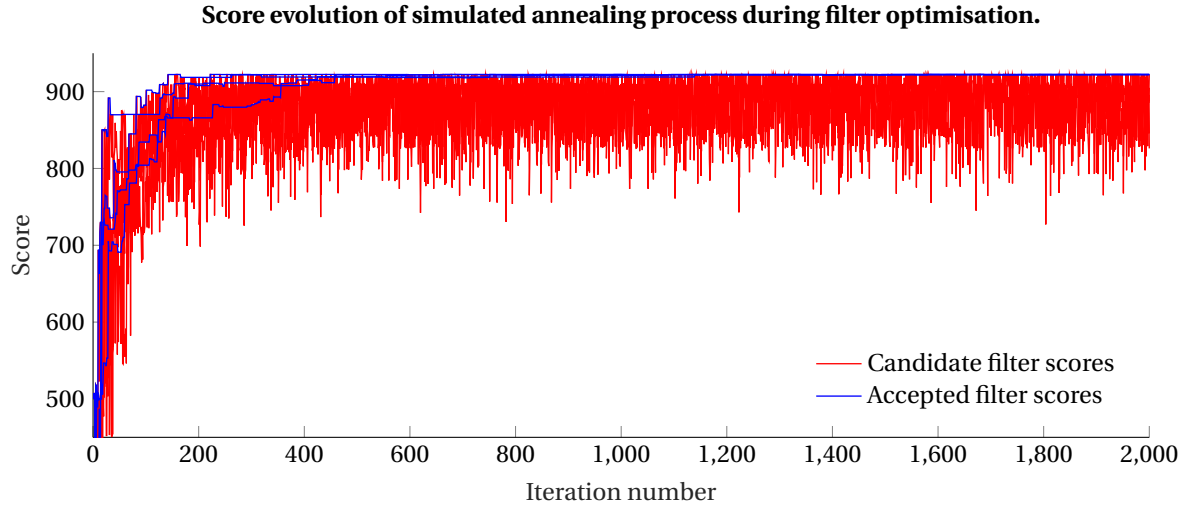
Figure 8.6: Simulated annealing score progression during filter optimisation. Seen is that no big jumps downward are made in the accepted solutions, however small ones are present at earlier iterations due to the lower temperature. Only the first 2000 iterations are shown as no improvements were accepted after it. All four runs were initialised identically and took different routes to the optimum as this is a stochastic method. The identical endpoints mean that the optimisation potentially found the global optimum.

Assuming a Gaussian spatial input spectrum profile, one could per entering and exiting angle combined with the width of the slab calculate some dispersion length d_{jl} for that combination of incident and exiting neutrons. Then that exiting group's intensity could be corrected for by assuming the dispersion length will transform the old Gaussian with its standard deviation σ_0 to the standard deviation of $\sigma_1 = \sqrt{\sigma_0^2 + d_{jl}^2}$. This means that the beam width will increase by that factor and the intensity will diminish by that factor. This diminishing factor could be applied as a first order correction of this dispersion. For an infinite plane source modelled as a Gaussian profile with infinite sigma, this exactly yields the same as without this correction.

8.4. Finding a filter for our treatment plan

In Chapter 7 eight spectra were found by the optimisation. For one of these spectra the neutron filter is calculated that best approximates this spectra given a certain input spectrum. For the source spectrum, a dummy spectrum is used with a high thermal and epi-thermal component without fast neutrons, see Figure 8.7. For 4 starting points, 10000 iterations were performed totalling at 1 CPU hour. The algorithm has no real stopping criteria defined and thus continues indefinitely. However, due to the multiple starting points and identical final scores, 2000 iterations would have sufficed. The resulting filtered output is shown in Figure 8.7. The score evolution of the filter optimisation is shown in Figure 8.6.

As seen in Figure 8.7, the spectrum is not completely reproducible for the given input spectra. Therefore it could be argued that spending computation hours on finetuning the exact beam weights to be used is quite useless if the spectrum can not be practically reproduced. Instead the filters itself should be optimised to deliver a good treatment plan to ensure that the treatment plan is able to be implemented.
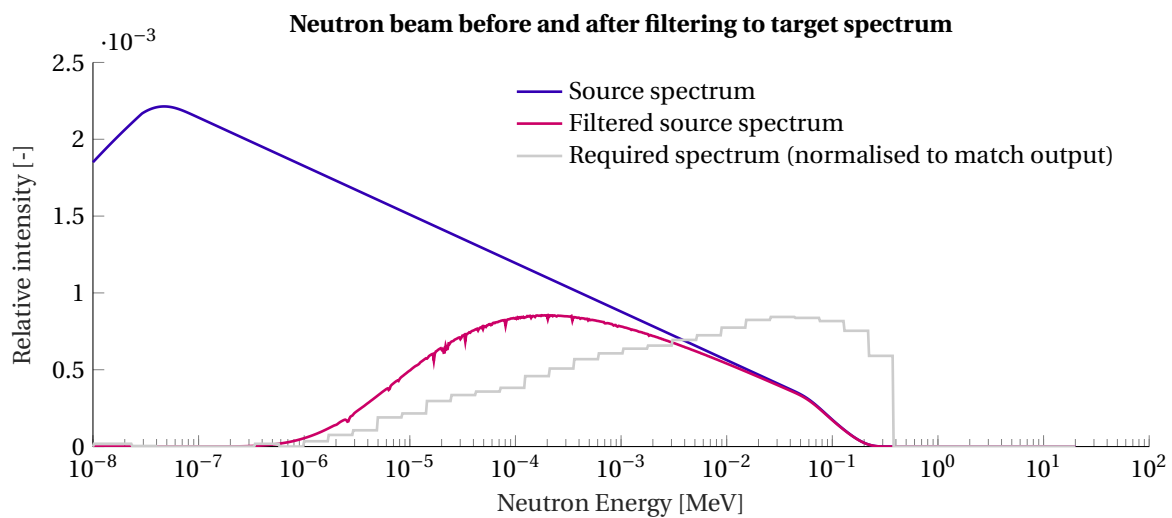
Figure 8.7: The dummy normalised input spectrum and its filtered output spectrum. The wanted spectrum is positioned and normalised to match the output spectrum. A total of 5 slabs of filter material was used in the filter as only a few slabs are needed to stop low energy neutrons. Expected is that filters that require the blockage of fast neutrons consist out of more slabs where the order of these slabs will start to play a more prominent role. This shows that first optimising the spectrum without keeping the filter in mind is not a viable method in treatment planning for GdNCT as the spectrum could not exactly be reproduced, at least for this source spectrum.

<div style="text-align: right; font-size: 3em;">9</div>

Joint optimisation of neutron beam filters and treatment plan

9.1. Necessity for joint optimisation

In the "spectrum first, filter later" approach, we saw that this produces unrealistic spectra to be given as the optimum. This is because the optimisation algorithm doesn't take the neutron source and filtering into account. In addition, this resulted in the inability to take contaminating gammas into account. Moreover, just the number of source neutrons per beamlet were calculated, not the actual treatment times which therefor could not be penalised.

However, the neutron filter optimisation in Chapter 8 and the treatment planning as was done in Chapter 7 do give us the necessary tools to directly optimise the neutron filter for each of the 8 beam positions and the corresponding irradiation durations to directly maximise the quality of the resulting treatment.

9.2. Coupling the treatment planning and filter optimisation

The neutron filter output spectrum is in this thesis given by 1000 energy bins and the dose beamlets are given for 40 energy bins. By resampling the 1000 output energy groups of the neutron filter to the 40 energy groups for which the beamlets have been calculated, the two could be coupled. Given the converted 8 spectra, of now 40 energy groups, combined with an irradiation time per beam, the 320 beamlet weights can be determined. From the 320 beamlets the total dose deposition could be calculated as was done in Chapter 7.

For the actual optimisation of the treatment plan, simulated annealing was used similar to that used in Chapter 8 where now 8 lists of integers are optimised along with the 8 beam durations. Sampling neighbouring solutions was now done by sampling neighbouring solutions in each of the 8 slab list of each filter. For the 8 continuous numbers, representing the irradiation times per beam, their neighbours are obtained by small random relative perturbations which decreased with the temperature T of the problem. Additionally, the algorithm kept track of the best overall solution and at each iteration could continue exploring or jump back to the best solution. The probability with which the algorithm was allowed to jump back to the best solution was based on the relative difference of the current solution and the best solution, such that if the current solution was almost as good as the best solution the exploring was more often allowed to continue. The jump back probability was given by

$$P_{\text{back}}(s', s, T) = \begin{cases} 0 & s > s' \\ 1 - \exp\left(-\frac{(1-s/s'')^2}{\mu T}\right) \text{ with } T = \frac{1}{i} & 0 < s \le s' \end{cases} \tag{9.1}$$

In Equation 9.1, the probability P_{back} is expressed by the best score s'', the candidate score s and the temperature T. Jump backs were only allowed if the current candidate score s was not better than the current accepted score s'. The μ parameter was chosen at 20, to yield longer exploring with relatively few jump backs.

The constraints, prescribed dose and cost function from Chapter 7 was kept the same. As this method reduces the size of the beamlet weight space, the cost of the optimised treatment plan from Chapter 7 forms

Optimised filter responses
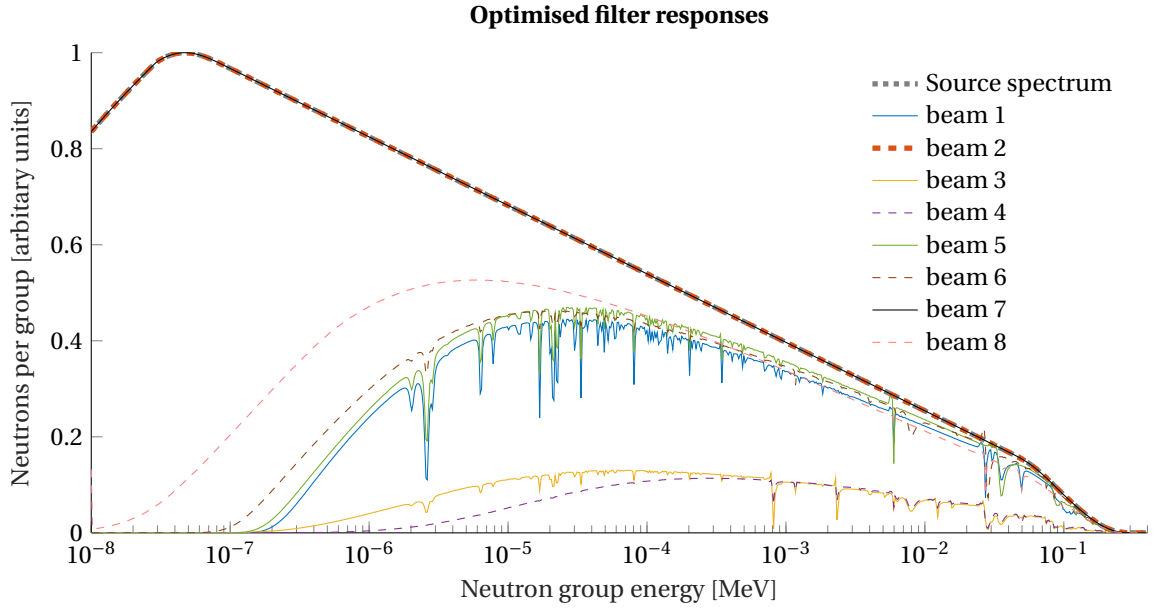
Figure 9.1: The 8 optimised filters their responses of the input fluxes from the beams shown in Figure 7.1. Not all beams were chosen to be filtered and if filtering was used, this was mostly done to block thermal neutrons. Beam 1 and 5 are most predominantly used in the treatment plan.

an upper boundary of that what is to be expected in this chapter. However, the practical implementation of the treatment plan resulting from this chapter would at least be possible due to the realistic spectra.

Since the types of spectra that are available or suited for GdNCT are unknown, a placeholder input spectrum was used like that used for the filter optimisation, see Figure 8.7. This input spectrum itself is not taken from any where in particular, however it does provide some regularisation on the higher energetic neutrons and should provide a good proof of concept. Moreover, the integrated flux of this spectrum could also be chosen arbitrarily, however, it is not yet known what types of fluxes are available of the source spectra that are suitable for GdNCT. Therefore, unit integrated flux was chosen that later would be rescaled to have the total treatment time be one hour. Penalisation of the treatment time was done by adding a regularisation term to the cost function of Chapter 7, penalising high values for the 8 continuous irradiation times parameters. No constraint was set to the treatment time as first a treatment plan which could provide tumour control at an accepted normal tissue complication risk was required before adding more secondary constraints.

Another downside of the method in Chapter 7 was the inability to account for contaminating gammas as providing these to the algorithm to tune would potentially lead to photon treatment instead. However, due to the filter estimation method as introduced in Chapter 8, information about the gamma production or passthrough in the filter is unknown as well. Therefore, this Chapter also excludes these contaminating gammas.

9.3. Resulting treatment plan

The preprocessed downsampled beamlets from Chapter 7 were used again for this chapter.

After 70 CPU hours and 130000 iterations the optimisation stopped due to reaching the maximum number of iterations as this optimisation method lacks any other stopping criteria. However, thousands of neighbours of this final optimum and several routes from the final optimum have been explored but all ended back at the same final point. Therefore, it can be stated that at least a local minimum has been found. Constraints were satisfied by definition and only two constraints were binding; the 90th percentile of dose to the rectum and the 95th percentile dose to other healthy tissue both were 20 Gy. The 90th percentile dose to the bladder was 18.6 Gy, instead of the allowed 20 Gy. The non-binded constraint shows that the "filter first" method has less freedom then the "spectrum first" method and can make less use of the allowed healthy tissue doses.

For different treatment time regularisation parameters, the optimiser found different treatment plans. For $5.17 \cdot 10^{15}$ source neutrons it found an optimal treatment plan with a peak bulk tumour dose of 28.7 Gy, a peak
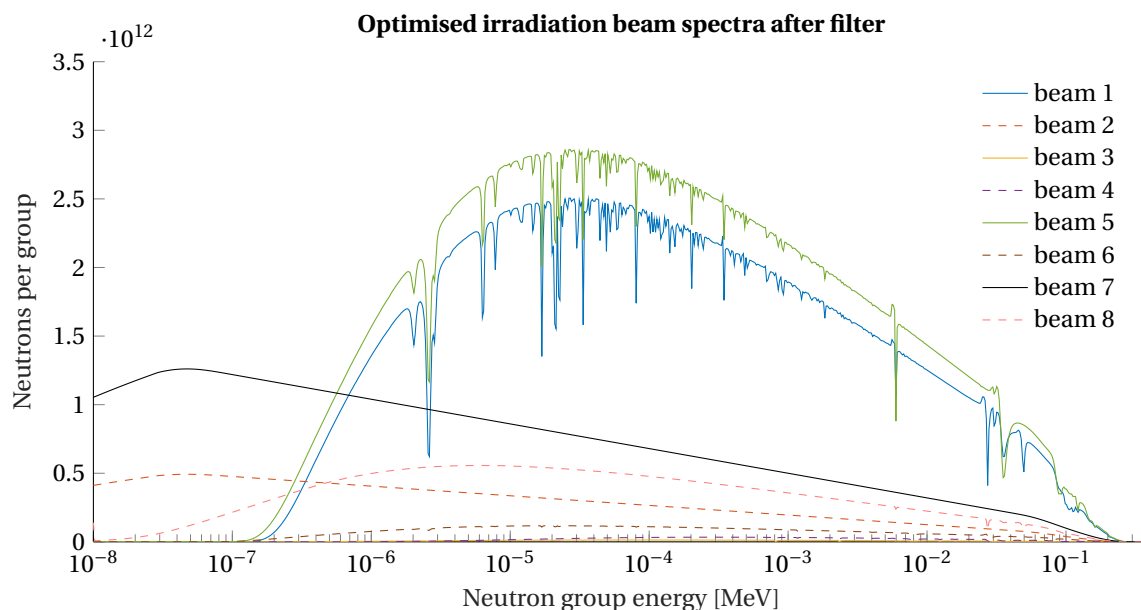
Figure 9.2: The 8 indirectly optimised time integrated spectra of the beams shown in Figure 7.1. The problem is nearly symmetric aside from the metastases, this symmetry is also visible in the resemblance of opposite beam spectra in the most predominant beams; 1 and 5.

shallow metastasis dose of 45.8 Gy and a peak deep metastasis dose of 37.8 Gy. However, the treatment plan detailed in this section used $6.86 \cdot 10^{15}$ source neutrons yielding a peak bulk tumour dose of 30.2 Gy, a peak shallow metastasis dose of 48.2 Gy and a peak deep metastasis dose of 38.8 Gy. The $6.86 \cdot 10^{15}$ source neutrons needed, yielded in $3.29 \cdot 10^{15}$ neutrons after filtering. Thus a flux of $24.3 \cdot 10^9$ neutrons cm^{-2} s^{-1} is needed to deliver this treatment plan within one hour.

The resulting dose distribution of this treatment plan is visualised in Figure 9.3 for the central plane in the phantom and for a lower plane holding the metastasis. The dose volume histograms of the organs-at-risk and the tumours for this treatment plan are shown in Figure 9.5. The constraints are visualised in the dose volume histogram as well, showing the two binding constraints and one non-binding constraint. The 8 different optimised filters their output is shown in Figure 9.1. By using these beams for different amounts of time these spectra can be scaled relative to each other. The final time integrated spectra that were used to calculate the treatment plan in Figure 9.3 are shown in Figure 9.2. Note that the spectra in Figure 9.2 were not directly optimised for but indirectly through the filter optimisation.

The two beams closes to the prostate (beam 1 and 5) were used the most in this treatment plan. For these two beams the thermal dose component added dose above the allowed 20 Gy without adding as much value as higher energies did and were therefore filtered out. The other beams were used much less in this treatment plan. How small the added value of a beam might be, the algorithm gains nothing from not using the beam, therefore these further located beams are present in some amount as they do contribute minute amounts to the tumour dose and dose to healthy tissue is not penalised. Some beams have not been filtered, as at the thermal hot spot of these beams the 20 Gy constraint was not a limiting factor and therefore the algorithm gained nothing with filtering these thermal neutrons out if it meant loosing some of the faster neutrons in the process.

Profiles through the tumours showing the dose differentiation are plotted in Figure 9.4. For this treatment plan the tumour cell dose in the bulk tumour ranged between 19.5 - 30.2 Gy while this was 19.6 - 28.7 Gy for the healthy cells within the same region, yielding in a maximal dose differentiation of about 5%. In the metastasis the tumour density was 100% and the doses to healthy cells have no significance there but they do form a good indication of what would happen to a cluster of healthy cells. In the shallower metastasis (Figure 9.3 B), the tumour cell dose ranged between 18.4 - 48.2 Gy and the theoretical dose to healthy cells in that region was 18.5 - 24.7 Gy with dose differentiations of up to 95%. In the deeper metastasis (Figure 7.3 A), the tumour cell dose ranged between 15.8 - 38.8 Gy and the theoretical dose to healthy cells in that region was 15.9 - 20.9 Gy with dose differentiations up to 86%.
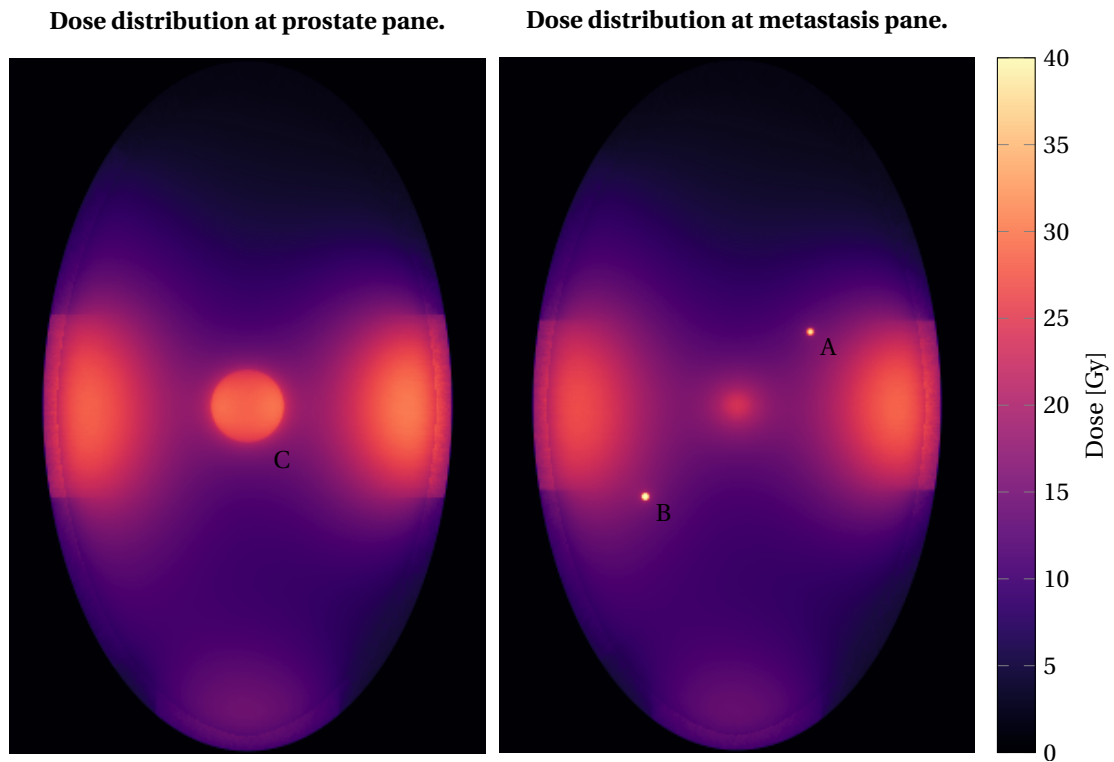
Figure 9.3: The resulting treatment plan using the "filter first" approach and treatment time penalisation. The image shows the dose components after post-processing. For the gadolinium dependent dose components the dose as is received in tumour cells is shown, i.e. inside tumour regions the dose shown is to tumour cells, outside it the dose shown is to healthy cells. Metastases (A) and (B) contained 700 ppm of ^{157}Gd at a tumour cell density of 100% and received respectively about 48.2 Gy and 38.8 Gy of peak dose. The bulk tumour (C) containing 700 ppm of ^{157}Gd at a tumour cell density of 50% received about 19.5 Gy to 30.2 Gy in the tumour cells. The absence of fast neutrons is apparent compered to the treatment plan found in Chapter 7. All doses are absorbed doses.

Dose profile through bulk tumour centre.

Dose profile through shallow metastasis centre.

Dose profile through deep metastasis centre.
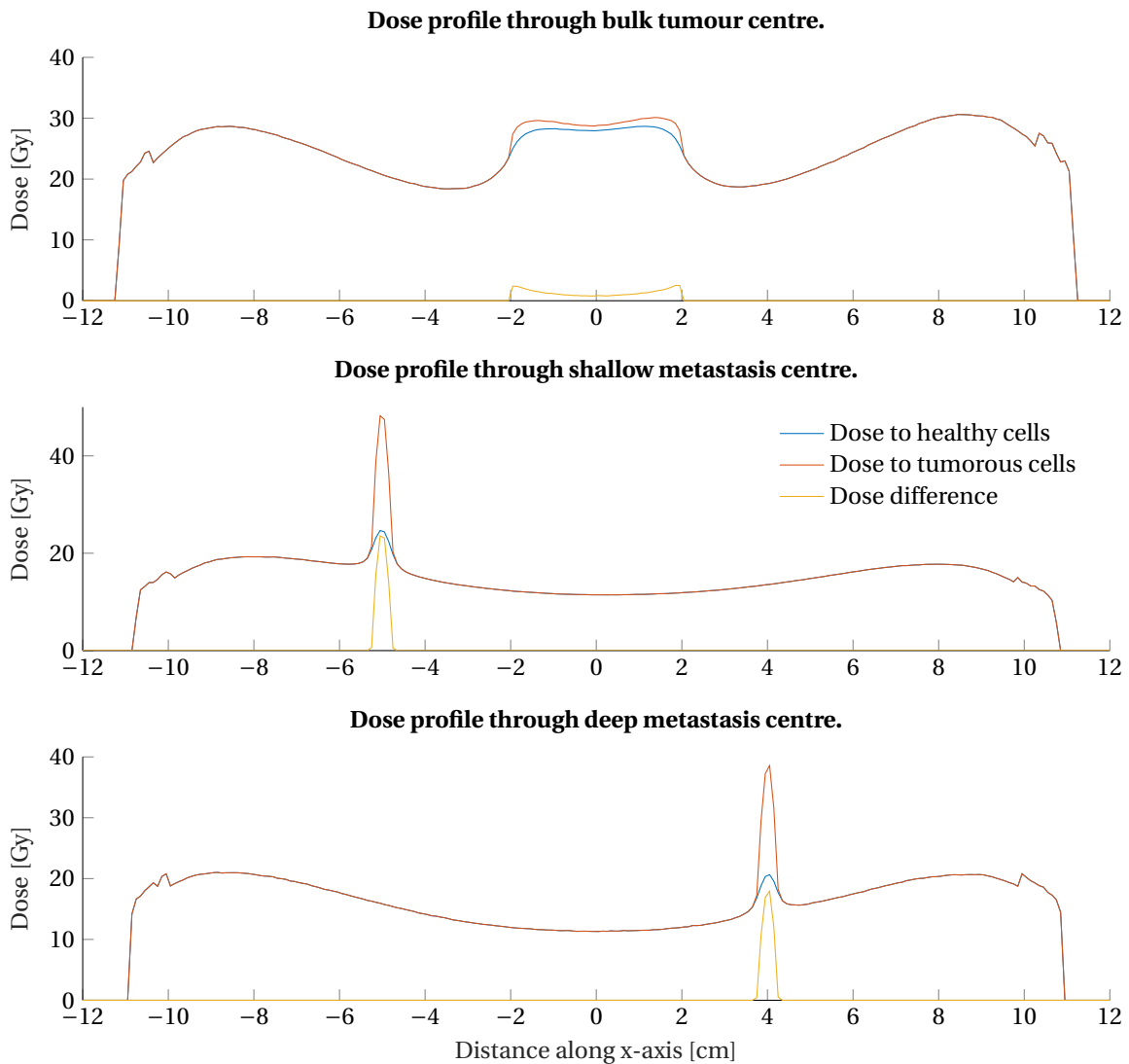
Figure 9.4: Off-axis profiles, parallel to the x-axis, through the metastases and bulk tumour. The bulk tumour, contained 700 ppm of ^{157}Gd at a tumour cell density of 50%. In the metastasis the tumour density was 100% and the doses to healthy cells have no significance there but they do form a good indication of what would happen to a cluster of healthy cells. All doses are absorbed doses.
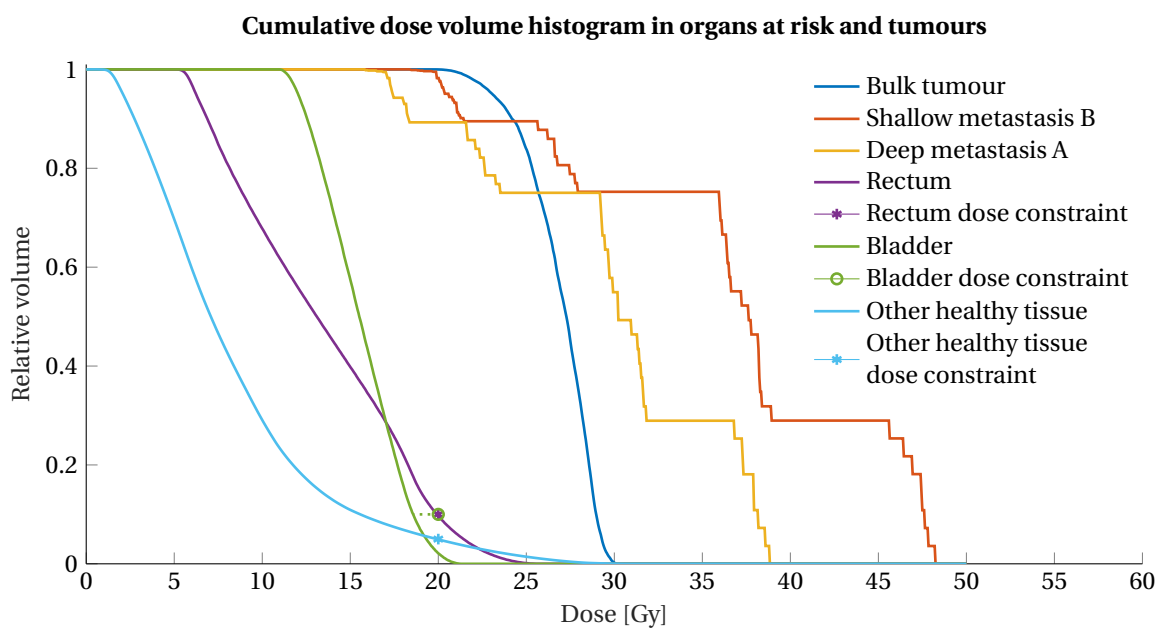
Figure 9.5: The minimal dose that is received by different relative volumes is shown in this dose volume histogram. The 2 binding constraints are shown as well. For the higher located bladder, this upper constraint was not reached as there was too little incentive or flexibility of the treatment plan to do so.

10

Conclusion

In the research to GdNCT several strong and weak points to this modality were discovered or confirmed. In addition, several details important to the dose calculations for such modalities have been identified and solutions to them have been developed. More work has to be done to make this modality a reality and I hope this thesis forms one of the building blocks to do so.

For a mostly thermal to epi-thermal treatment plan, the treatment plan was expected to be very robust to the relative position of the patient to the beam. This is because any strong gradients to the dose distribution are due to properties of the body such as gadolinium concentration, and not properties of the beam such as direction. For fast neutrons, the beam does retain direction and a slight offset in the beam direction would cause a different dose distribution. In addition it was observed that a small relative change in beam energy does not lead to a significant different dose distribution, unlike in proton therapy where higher energies means overshooting the target. This makes this method overall very robust if no emphasis on fast neutrons is made in the spectrum.

The thermal flux and thus gadolinium neutron capture rate is usually larger before hitting the tumour providing any undetected gadolinium containing tumour cells automatically with a dose boost larger than at the main tumour when using a single beam. For beams from opposite directions, however, this extra dose becomes insignificant due to the extra distance and thermal flux decay. In future work a perturbation study could be performed on treatment plans to see in what regions these undetected tumorous cells also will receive a high enough dose. This perturbation study will have to account for the different leakages observed for different tumorous mass fractions. In the metastasis tested in this thesis, voxels on the edge of the tumour often contained so little gadolinium that a large leakage of their electrons was assumed. Hypothesising on this outcome, this perturbation study could see very little added dose in the perturbations keeping in mind the large leakages of electrons in single cell sizes clusters. The result of such a perturbation study could therefore by highly dependent on the CBE factor of the Auger electrons that do not leave the cell. If this modality proofs successful in providing significant dose in such small clusters it could then be applied as an adjuvant therapy, after prostatectomy for example, where no addition tumour cells can be detected but are suspected. Treatment optimisation would then involve a statistical view of where these cells are expected and the flux needed there to provide significant dose boost would then be optimised for.

In conventional radio therapy, the prostate will see an identical absorbed dose as the tumour cells spread out over said prostate. However, in chemically targeted GdNCT it is possible to provide slightly lower dose to the healthy cells compared the tumours cells within the same area. This is due to the high specificity of the tumour-selective compound and the short range of some of the reaction products. This effect was observed to be up to 100% in some regions of the treatment plan with high fluxes of thermal neutrons. For lower tumorous fractions found at the tumour's edges or in very low tumour density prostates, this differentiation could drop to zero or even slightly below zero. In our treatment plans this was observed in the low tumour edge doses, which do spare healthy tissue but do not provide good tumour control. Unfortunately, the use of margins in this modality is impossible to to the chemical targeting.

The calculated treatment plans were not able to provide a adequate therapeutic dose in any voxel, even under very weak constraints on the doses to organs at risk. As this is a basic requirement that treatment

modalities are expected to adhere, it suggests that GdNCT is not a viable treatment modality for the deeper and larger tumours. Again pointing towards using PSMA GdNCT as adjuvant therapy or to combine it with traditional therapies that complement the short comings of GdNCT.

There could, however, be a case where GdNCT could potentially supply a better dose to the tumour. When moving from prescribed dose to prescribed biological effect, there is a possibility that the biological effect of the gadolinium electrons could be greater than what conventional radiation weighting factors would suggest. This could mean that 1 Gy of typical background radiation could be less harm-full to the healthy tissue than 1 Gy in the tumour. However, the neutrons that mainly add to the unwanted dose have a relatively large radiobiological effect compared to that of photons as well, meaning that the two could potentially cancel out. Additionally differentiations of zero percent or lower have been observed, meaning that in those regions the CBE of the gadolinium electrons will not see significant positive effect.

Moreover, neutrons have a very bad penetration into the tumour as the inner areas are blocked by the gadolinium in the outer areas. This is visible in the short range gadolinium electron dose deposition which is most predominant near the edges of the tumour. Although the photons produced in the bulk tumour provide most of their dose to the centre of the bulk tumour, this is not because most photons were created there but rather the build-up effect. Now the mainly central dose of the photons and mainly edge dose of the gadolinium work together to provide a more homogenous dose than any on their own. If, however, the gadolinium electrons are expected to be many times more effective in causing biological damage than photons, the added benefit is mainly to the outer half of the tumour. Meaning that even for this optimistic biological effectiveness, bulk tumours would still see insufficient dose to their centre. For adjuvant therapy, after prostatectomy or prior irradiation, the tumour is only expected to be present in very small clusters were this is less of an issue. In such case, the potential higher radio biological effectiveness of the gadolinium electrons could be greatly beneficial, provided that the dose leakage in these clusters is low.

It was also shown, that enabling electron transport is important for GdNCT dose calculations. Without it, doses to the tumour could be overestimated. Up till now, no literature was published that performed GdNCT dose calculations with the electron transport. The kernel based dose deposition approximations were used to approximate electron transport, requiring less computation time. This method, however, is only valid in homogeneous media.

An important detail of dose calculations in chemically targeted radio therapy in general, is the distinction between targeted and non-targeted cells needs to be made. This is especially the case for short range reaction products (like gadolinium electrons), high specificity to the targeted cells (like PSMA) and when the voxels are expected to contain a mixture of targeted and non-targeted cells (typically so in the prostate). Dependent on how much of the total dose relies upon these particles, a significant dose difference could be seen when properly accounting for this effect.

The treatment plans obtained by optimising beam weights was shown to not easily be applied in practice as the spectra were impossible or at least difficult to obtain with filtering alone. Instead direct filter based optimisations were needed to assure a practical treatment plan. The simplified neutron filter model developed for this provided the final puzzle piece to implementing this type of treatment planning.

Initially this thesis set out to perform treatment planning on patients after prostatectomy as well, only irradiating metastasis or as adjuvant treatment. However, due to time constraints, this was never done. Although, based on several of the conclusions made in this section, such treatment plans could potentially be of a high enough quality to be implemented in real life since the deep bulk tumours form the main obstacle for GdNCT. I therefore recommend that further research would investigate such cases. In addition, further research into the exact quantification of the biological effectivenesses involved in this modality are also needed.

A
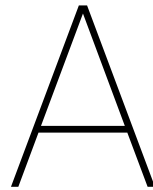
Appendix: Implementation of fluxed based reaction rate and dose calculations

A.1. Comparison of different dosimetry implementations

To compare all the different implementations in this chapter, a standardised geometry will be used on which the different implementations are applied on.

An isotropic pure thermal neutron source is placed in the centre of a 4 x 4 x 4 meter cube of Soft Tissue equivalent material (IRCP four component Soft tissue). To this material 700 ppm Gd[157] is added. Each tally type is assigned to the whole cube and each `FMESH` tally type is overlaid such that the edges equal that of the cube. The size of the cube is chosen such that no energy leakage is expected. This will cause the total photon kerma to equal the real photon dose via electrons. The geometry as provided to MCNP is given by the following code snippet.

```
Cube
1 2 -1    100 -200 300 -400 500 -600    imp:n,p,e=1
2 0     #(100 -200 300 -400 500 -600)   imp:n,p,e=0

100   px -200
200   px 200
300   py -200
400   py 200
500   pz -200
600   pz 200
c Soft Tissue (IRCP 4 component) + 700ppm Gd-157
M2    1001.80c  -0.101172         $ H-1 and mass fraction
      6000.80c  -0.111000         $ C and mass fraction
      7014.80c  -0.026000         $ N-14 and mass fraction
      8016.80c  -0.761128         $ O-16 and mass fraction
      64157.80c -0.0007           $ Gd-157 and mass fraction 700ppm
      nlib=.80c elib=.03e plib=.12p
MT2 lwtr.20t
c pure Gd-157 for isotope specification
M3    64157.80c 1 $ Gd-157
```

Coupled neutron, photon and electron transport was used. Cut off values were chosen to match the values to be used in longer calculations. Since F6 tallies include non-transported particles and F4 tallies not, the energy cut-off should be low as the equivalence of these two tallies is being tested. Due to computational time restrictions they should not be too lower either. This was provided to MCNP in the form of the following code snippet.

```
mode N P E
cut:e j 1e-3 $ electron cut-off below 1keV
cut:p j 1e-3 $ photon cut-off below 1keV
```

A.2. Different implementations of reaction rate calculation

Mesh calculations allow us to define a 3d lattice of voxels without defining each of the voxel separately in the geometry of the problem. The dose of each of the 3d (rectangular) volumes is then calculated by MCNP. The FM card when used in an FMESH tally can be prefixed by a plus sign. The material number should than be replaced with a material number corresponding to the isotope of interest. MCNP will then calculate the atomic fraction of the specified isotope in the event material. A flux based reaction rate calculation in a mesh for this reaction type could be implemented as is done in the following code snippet.

```
c The Gd neutron capture rate
FMESH304:n ORIGIN=-200 -200 -200 IMESH=200 IINTS=1
     JMESH=200 JINTS=1 KMESH=200 KINTS=1 OUT=CF FACTOR=1
+FM304 -1 3 102
c -------------------------------------------------------
c  -1 = atomic fraction
c   3 = use material 3
c 102 = use cross section for (n,y) reaction
c -------------------------------------------------------
c output = 1.47812E-08 g^-1 src.n.^-1 +-0.97%
```

If no mesh is used but the dose of a volume as defined in the geometry is to be known then the flux based reaction rate calculation could be done using an F4 tally. In a normal F4 tally one would have to manually specify the cross section to be used and with what atomic fraction to scale the cross section over the whole geometry. In that case the specified reaction probability is constant throughout the problem and thus is not valid in regions that differ from the specified material in composition. An example implementation is provided in the following code snippet.

```
c Gd-157(neutron,gamma)
F204:n 1
FM204 ((-2.7959469E-05 3 102))
c -------------------------------------------------------
c output = 1.47378E-08 g^-1 src.n.^-1 +-0.97%
```

The differences in output here are explained by the different data MCNP uses to calculate the atomic fractions compared to what I used here.

A.3. Different implementations of neutron dose calculation

The neutron dose in the MCNP F6:n tally is specified as the total Q-value of neutron interactions minus the energy of the photons transported away. In the F6:n tally, MCNP already performs temperature correction and the multiplication with the appropriate cross-sections and heating numbers. The F6 tally works on a single volume as defined in the geometry. An example implementation is given in the following code snippet.

```
c Neutron kerma (direct)
F46:n 1
c -------------------------------------------------------
c output = 3.14732E-11 MeV g^-1 src.n.^-1 +-1.02%
```

When an independently defined mesh is desired for the dose description, a FMESH tally could be used. The FMESH allows us to place a wild card for the material number. MCNP will then choose the material in which the event takes place.

```
c Neutron kerma mesh (flux-to-kerma)
```

```
FMESH7144:n ORIGIN=-200 -200 -200 IMESH=200 IINTS=1
      JMESH=200 JINTS=1 KMESH=200 KINTS=1 OUT=CF FACTOR=1
FM7144 -1 0 1 -4
c ---------------------------------------------------------
c -1 = atomic fraction
c  0 = use event material
c +1 = temperature corrected total neutron cross sections
c -4 = total average neutron heating
c ---------------------------------------------------------
c output = 3.14732E-11 MeV g^-1 src.n.^-1 +-1.02%
```

Although similar to the FMESH, no wild card is allowed and the material is hard coded in the FM card. It is therefore only valid in the cells where the material is indeed the same. This requires the cells and the geometry to be aligned.

```
c Neutron kerma (flux-to-kerma)
F744:n 1
FM744 -1 2 1 -4
c ---------------------------------------------------------
c -1 = atomic fraction
c  2 = use material 2 (our cube material)
c +1 = temperature corrected total neutron cross sections
c -4 = total average neutron heating
c ---------------------------------------------------------
c output = 3.14732E-11 MeV g^-1 src.n.^-1 +-1.02%
```

The effect of using the temperature corrected cross sections over the uncorrected ones was less than 0.001%.

A.4. Different implementations of photon dose calculation

A direct calculation of the photon dose in a volume could be implemented as the following.

```
c Photon kerma (direct)
F36:p 1
c ---------------------------------------------------------
c output = 1.19667E-07 MeV g^-1 src.n.^-1 +-1.08%
```

In a mesh this could be implemented as a flux based photon dose mesh as is seen in the following code.

```
c Photon kerma mesh (flux-to-kerma)
FMESH134:p ORIGIN=-200 -200 -200 IMESH=200 IINTS=1 JMESH=200 JINTS=1
      KMESH=200 KINTS=1 OUT=CF FACTOR=1
FM134 -1 0 -5 -6
c ---------------------------------------------------------
c -1 = atomic fraction
c  0 = use event material
c -5 = total photon cross sections (+5 is illegal)
c -6 = total average photon heating
c ---------------------------------------------------------
c output = 1.20548E-07 MeV g^-1 src.n.^-1 +-1.08%
```

A non mesh analog for this is given by the following.

```
c  Photon kerma (flux-to-kerma)
F34:p 1
FM34 -1 2 -5 -6
c ---------------------------------------------------------
```

```
c -1 = atomic fraction
c  0 = use event material
c -5 = total photon cross sections (+5 is illegal)
c -6 = total average photon heating
c ---------------------------------------------------------
c output = 1.20548E-07 MeV g^-1 src.n.^-1 +-1.08%
```

A.5. Different implementations of electron dose calculation

The direct implementation of the electron dose in a single volume is given by the following code.

```
FC56 Electron dose direct
F56:e 1
c ---------------------------------------------------------
c output = 1.20150E-07 MeV g^-1 src.n.^-1 +-0.64%
```

Unlike that in the case of photons and neutrons, MCNP does not allow special multipliers in the FM card for electron tallies.

The flux-to-dose tables used here were added manually by using the DE and DF cards. The data used were the collision stopping powers for electrons for this specific material. The data was obtained by running the problem in MCNP with the `print 85` command which triggers the stopping power tables for all materials specified in the problem. One can increase the resolution of this table by adjusting the `efac` attribute on the `phys:e` card. The total stopping power was split in the collision stopping power and the radiative stopping power of which only the collision stopping power was used in this problem.

The collision stopping power includes energy loss by excitation of nuclei and, if the bounding energy is surpassed, ionisation of those nuclei. Since the stopping power already includes the energy of the ionisation electrons, those electrons should not be transported to avoid counting them again later on. To achieve this in MCNP, the knock-on electron production is disabled on the `phys:e` card.

```
phys:e 100. 6j 0 $ rnok = 0
```

The table does not include radiative stopping powers by bremsstrahlung, therefore this can be left enabled on the `phys:e` card since the energy electrons created by those bremsstrahlung photons have not been counted yet. The implementation of this method is given by the following code.

```
c Electron dose mesh (flux-to-kerma via DE/DF)
FMESH154:e ORIGIN=-200 -200 -200 IMESH=200 IINTS=1 JMESH=200 JINTS=1
      KMESH=200 KINTS=1 OUT=CF FACTOR=1
DE154 LOG
      1.0790E-03
      1.1766E-03
      1.2831E-03
      ...
      ... left out for space
      ...
DF154 LOG
      1.130E+02
      1.068E+02
      1.009E+02
      ...
      ... left out for space
      ...
c ---------------------------------------------------------
c DE  = energy points in MeV
c DF  = collision stopping power in MeV cm2/gram
c LOG = logarithmic interpolation
c ---------------------------------------------------------
c output = 1.19063E-07 MeV g^-1 src.n.^-1 +-0.65%
```

Although the deviation of the two methods is within the sampling error, the results are based on the same sampled events and therefore should be identical. This means that the deviation is either due to the lack of counting the cut-off electrons or interpolation errors. In the latter case, the lookup table resolution could be increased by adjusting the `efac` attribute on the `phys:e` card. In a validation, this added resolution slowed down the calculation significantly while only correcting a small part of the error. Additionally, having only one fixed table for the whole geometry can be a good approximation in GdNCT since up to 700 ppm ^{157}Gd concentration the stopping power values in the table do not change more than 0.05%.

Above electron energies of 100 MeV the collision stopping powers and the total stopping powers start to differ significantly. As an extra validation for this electron dose deposition estimation method, the source particles ware replaced with high energy electrons. Using the total stopping powers for these high energies showed a dose higher than the photon kerma which violates energy conservation while using the collision stopping powers did not, thereby validating the use of the collision stopping powers and the correct dis-/enabling of secondary particles.

B

Appendix: Validation of Monte Carlo simulated neutron capture

B.1. Cross Section Libraries

Neutron (ENDF/B-VII.1, room temperature)   To access the latest ENDF/B-VII.1 data for neutrons at room temperature (293.6 K) from the `xsdir` I use the `.80c` suffix that specifies room temperature and continuous data. Room temperature is the closest match for body temperature (310 K) by far since for many isotopes the next available temperature is 600 K.

Photon   For photon interactions, MCNP does not distinguish between the exact isotopes so, for example, `1001.12p` is converted to `1000.12p`. The suffix `.12p` points to the ENDF/B-VI Release 8 photo/electro-atomic and relaxation data from `xmc/eprdata12`. This library is the newest library available concerning photons and is recommended by MCNP as essential for low photon energy transport in MCNP6.

Electron   The newest `.03e` suffix from `xdata/el03` was used. This is also recommended by MCNP as essential for low electron energy transport in MCNP6. This is important as the Auger cascade following ^{157}Gd neutron capture are mainly low energy electrons.

B.2. ^{157}Gd evaluation

A snippet of the MCNP input file used to evaluate the ^{157}Gd(n,γ) reaction is as follows:

```
Gd-157 foil experiment
  1 0        -801: 803:-401: 402:-403: 404  imp:n,p,e=0  $ Void
100 0         801 -802  401 -402  403 -404  imp:n,p,e=1  $ Vacuum
101 1 -1     802 -803  401 -402  403 -404  imp:n,p,e=1  $ Gd foil

c Surfaces
801 py 0
802 py 1               $ neutron beam facing face of foil
803 py 1.0001          $ back face of foil
c
401 px -50
402 px  50
403 pz -50
404 pz  50

mode N P E $ the E flag is only used in the NPE run.
```

```
M1   64157 -1 elib=.03e plib=.12p nlib=.80c COND=-1 $ no conductor
dbcn 17j 2             $ enable double strangling of electrons
phys:e 100. 13j 0.01  $ use single-event mode below 10 keV
cut:p j 1.0e-06       $ 1 eV photon cut-off
cut:e j 1.5e-05       $ 15 eV electron cut-off
[... left out for space ...]
F424:n 101
FM424 ((-1 1 102)) $ 102 for (n,gamma)
F454:n 101
FM454 ((-1 1 105)) $ 105 for (n,proton)
F474:n 101
FM474 ((-1 1 107)) $ 107 for (n,alpha)
*F101:p (802 803)     $ Total photon outgoing energy
F106:p 101            $ Total photon deposition energy
*F201:e (802 803)     $ Total electron outgoing energy
F206:e 101            $ Total electron deposition energy
F306:n 101            $ Total neutron deposition energy
[... left out for space ...]
nps 1e7
print
```

B.3. ^{155}Gd evaluation

A few changes to the script described in Section B.2 let us do the dose calculations for ^{155}Gd.

```
Gd-155 foil experiment
[... unchanged ...]
M1   64155 -1 elib=.03e plib=.12p nlib=.80c COND=-1
[... unchanged ...]
```

B.4. Natural gadolinium evaluation

A few changes to the script described in Section B.2 let us do the dose calculations for ^{155}Gd and ^{157}Gd with their natural abundances. To differentiate between the two, the F424 tally is split into a ^{155}Gd and a ^{157}Gd dedicated tally.

```
Gd foil experiment
[... unchanged ...]
M1
     64155 -0.486
     64157 -0.514
     elib=.03e plib=.12p nlib=.80c COND=-1
M2   64155 -1
M3   64157 -1
[... unchanged ...]
F4214:n 101
FM4214 ((-0.4892232774 2 102)) $ Gd-155; 0.486*(155*0.486 + 157*0.514)/155
F4224:n 101
FM4224 ((-0.5108177834 3 102)) $ Gd-157; 0.514*(155*0.486 + 157*0.514)/157
[... unchanged ...]
```

B.5. ^{10}B evaluation

A few changes to the script described in Section B.2 let us do the same for BNCT. We are now interested in another reaction, namely ^{10}B(n,α). Since this reaction does not produce electrons, the E flag was omitted on the MODE card. From the JENDL-4.0 library we know that not only ^{10}B(n,α) reactions are possible for thermal

neutrons but also ^{10}B(n,p) and ^{10}B(n,γ). The respective MT reaction numbers are 107, 105 and 102 on the tally multiplier card which were already included in the input file described in Section B.2.

```
[... left out for space ...]
mode N P
M1
    5010 -1  $ boron-10
    elib=.03e plib=.12p nlib=.80c COND=-1
[... left out for space ...]
```

B.6. Results

B.6.1. ^{157}Gd reactions

Table B.1: ^{157}Gd foil tally results

Tally	Description	per source neutron	per (n,γ) reaction
F424	Total Gd(n,γ) reactions	9.25373E-02 (±0.01%)	≡1
F454	Total Gd(n,p) reactions	none	none
F474	Total Gd(n,α) reactions	1.73361E-10 (±0.01%)	almost none
F106	Photon energy deposition	1.54442E-05 MeV (±8.93%)	1.66897E-4 MeV (±8.93%)
*F101	Photon energy escaping	7.26456E-01 MeV (±0.12%)	7.85041 MeV (±0.12%)
*F101 + F106	Total photon energy	7.26471E-01 MeV (±0.12%)	7.85057 MeV (±0.12%)
Summary	Total photon energy from neutrons	7.26469E-01 MeV	-
Summary	Total photon energy per neutron collision[1]	-	7.82752 MeV
F206	Electron energy deposition (NPE mode)	9.53143E-07 MeV (±12.39%)	1.03001E-5 (±12.39%)
*F201	Electron energy escaping (NPE mode)	1.19202E-05 MeV (±26.43%)	1.28815E-4 (±26.43%)
*F201	Total electron energy (NPE mode)	1.2873343E-5 MeV (±24.49%)	1.3912E-4 MeV (±24.49%)
F306	Neutron energy deposition	2.44748E-06 (±0.01%)	2.44748E-06 MeV (±0.014%)
F306 + F101 + F106	Total Q-value	7.26473E-1 MeV (±0.12%)	7.85060 MeV (±0.12%)

Since neutron dose from the F6 tally includes all energy except for the photons and the photon energy is tallied separately, summing the two would give us the total average Q-value of all reactions due to the thermal neutrons with ^{157}Gd.

B.6.2. ^{155}Gd reactions

Table B.2: ^{155}Gd foil tally results

Tally	Description	per source neutron	per (n,γ) reaction
F424	Total (n,γ) reactions	2.33325E-2 (±0.00%)	≡1
F454	Total (n,p) reactions	none	none
F474	Total (n,α) reactions	2.55766E-11 (±0.00%)	almost none
F106	Photon energy deposition	3.07703E-6 MeV (±5.44%)	1.31877E-4 MeV (±0.00%)
*F101	Photon energy escaping	1.97401E-1 MeV (±0.24%)	8.46035 MeV (±0.00%)
*F101 + F106	Total photon energy	1.97404E-1 MeV (±0.24%)	8.46047 MeV (±0.24%)
Summary	Total photon energy from neutrons	1.97403E-1 MeV	-
Summary	Total photon energy per neutron collision[2]	-	8.48611E+00 MeV
F206	Electron energy deposition (NPE mode)	1.01089E-7 MeV (±42%)	4.33254E-6 (±42%)
*F201	Electron energy escaping (NPE mode)	1.74949E-6 MeV (±44%)	7.49808E-5 (±44%)
*F201	Total electron energy (NPE mode)	1.85058E-6 MeV (±43%)	7.93134E-5 (±43%)
F306	Neutron energy deposition	5.15411E-07 MeV (±0.00%)	2.20898E-5 MeV (±0.00%)
F306 + F101 + F106	Total Q-value	1.97404E-01 MeV (±0.24%)	8.46049 MeV (±0.24%)

The results of this experiment are shown in Table B.2. Again due to the low incidence of reactions other than (n,γ) we can assume that all energy came from (n,γ). Since no other material was present than ^{155}Gd, we can narrow this down to ^{155}Gd(n,γ) reactions.

---

[1] Assumed is that every "neutron collision" as stated in the MCNP summary is a ^{157}Gd(n,γ) reaction.
[2] Assumed is that every "neutron collision" as stated in the MCNP summary is a ^{155}Gd(n,γ) reaction.

B.6.3. Natural gadolinium reactions

Table B.3: Natural gadolinium foil tally results

Tally	Description	per source neutron	per (n,γ) reaction
F4214	Total Gd-155(n,γ) reactions	1.11325E-2 (±0.00%)	18.70%
F4224	Total Gd-157(n,γ) reactions	4.84041E-2 (±0.00%)	81.30%
F106	Photon energy deposition	9.41883E-6 MeV (±6.38%)	1.58202E-4 MeV (±6.38%)
*F101	Photon energy escaping	4.75460E-1 MeV (±0.15%)	7.98601 MeV (±0.15%)
*F101 + F106	Total photon energy	4.75469E-1 MeV (±0.15%)	7.98616 MeV (±0.15%)
Summary	Total photon energy from neutrons	4.75468E-1 MeV	-
Summary	Total photon energy per neutron collision[3]	-	7.96559 MeV
F306	Neutron energy deposition	1.52607E-6 MeV (±0.00%)	2.56325E-5 MeV (±0.00%)
F306 + F101 + F106	Total Q-value	4.7547E-1 MeV	7.98619 MeV (±0.15%)

The results of this experiment are shown in Table B.3.

B.6.4. ^{10}B reactions

Table B.4: B-foil tally results

Tally	Description	per source neutron	per (n,α) reaction
F424	Total B(n,γ) reactions	2.97229E-6 (±0.00%)	low
F454	Total B(n,p) reactions	3.36542E-9 (±0.00%)	low
F474	Total B(n,α) reactions	2.28472E-2 (±0.00%)	≡1
F106	Photon energy deposition	1.65508E-7 MeV (±5.67%)	7.24413E-6 MeV (±5.67%)
*F101	Photon energy escaping	1.02159E-2 MeV (±0.22%)	4.47140E-1 MeV (±0.22%)
*F101 + F106	Total photon energy	1.02161E-02 MeV (±0.22%)	4.47149E-1 MeV (±0.22%)
Summary	Total photon energy from neutrons	1.02161E-2 MeV	-
Summary	Total photon energy per neutron collision[4]	-	4.48580E-1 MeV
F306	Neutron energy deposition	5.35071E-2 MeV (±0.00%)	2.34195 MeV (±0.00%)
F306 + F101 + F106	Total Q-value	6.3723E-2 MeV	2.78910 MeV (±0.035%)

Since neutron dose from the F6 tally includes all energy except for the photons and the photon energy is tallied separately, summing the two would give us the total average Q-value of all reactions due to the thermal neutrons with ^{10}B. We knew that not only B(n,α) reactions were possible for thermal neutrons. However, as seen in the results, these other reactions have very low incidence. Therefore we can assume that the total Q-value is close to that of just B(n,α), see Table B.4.

B.7. Handling missing energy in MCNP

To cope with the missing energy (see Section 3.3) many methods are possible. The first method is to tally the neutron capture rate and multiplying it by the missing energy per neutron capture literature kerma values. For this, a method to obtain the reaction rates is needed. A mesh tally that would count this in MCNP is as follows:

```
c The Gd neutron capture rate
FMESH304:n ORIGIN=-200 -200 -200 IMESH=200 IINTS=1
     JMESH=200 JINTS=1 KMESH=200 KINTS=1 OUT=CF FACTOR=1
+FM304 -1 3 102
c -------------------------------------------------------
c  -0.05 = atomic fraction times 50 keV
c   3    = use material 3
c 102    = use cross section for (n,y) reaction
c -------------------------------------------------------
```

---

[4]Assumed is that every "neutron collision" as stated in the MCNP summary is a ^{10}B(n,α) reaction.
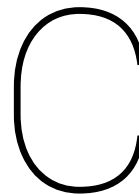
Appendix: Cell culture experiment simulation details

C.1. Transport settings

The simulation is performed using coupled neutron, photon and electron transport. For each experimental setting the experiment is done for a neutron source and a contaminating gamma source separately. The neutron run has an additional run to convert the ^{157}Gd(n,γ) and ^{155}Gd(n,γ) kerma (dose under Charged Particle Equilibrium assumption) to a real dose deposition without the Charged Particle Equilibrium assumption. In these calculations an isotropic electron start direction distribution is assumed and the particle starting positions are chosen according to the kerma distribution. Later, all transported energy is normalised to equal the deposited energy in the kerma approximation.

Using the same input file with different source specification and the cut-off energies allow us to perform the initial neutron source and separate contaminating gamma source calculations and the final simulation with the electron source within the cell layer. Both the initial neutron and photon runs were performed using the following settings:

```
cut:e j 2.0e-4 $ Electron cut-off below 200 eV
cut:p j 1.0e-5 $ Photon cut-off below 10 eV
```

The secondary transport of the low energy electrons from the Gd(n,γ) was performed with the lowest stable cut off energies, to capture the effect of even the shortest range electrons:

```
cut:e j 1.5e-5 $ Electron cut-off below 15 eV
cut:p j 1.0e-6 $ Photon cut-off below 1 eV
```

All simulations ran $1 \cdot 10^7$ histories to achieve reasonable statistics.

C.2. Material definition

All reported material specifications are applied uniformly over the volumes, i.e. gadolinium is assumed to be homogeneously distributed in the cell layer.

To account for the effects of bound hydrogen in neutron scattering, thermal scattering S(α,β) treatment cards are used. The .20t suffix points to the ENDF/B-VII.1 based continues thermal scattering laws, that are new to MCNP6.

To simulate the petri dish in the experiment, the Corning Falcon Bacteriological Petri Dishes with Lid was used. This petri dish was made from crystal-grade polystyrene. This material is defined as Polystyrene. The closest match for the thermal treatment of hydrogen is a polyethylene approximation. The material card is given as follows:

```
M1
    1001 -0.077421                     $ mass-fraction hydrogen-1
    6000 -0.922579                     $ mass-fraction oxygen-16
    elib=.03e plib=.12p nlib=.80c      $ newest libraries
MT1 poly.20t                           $ thermal treatment for hydrogen in polyethylene
```

The liquid in the container comprises of a water solution of mostly hydro-carbon rich materials, although exact quantities were hard to deduce from the provided information. The liquid was simulated as IRCU standard four component soft tissue material for which the material card is given as follows:

```
M2
    1001 -0.101172                     $ mass-fraction hydrogen-1
    6000 -0.111000                     $ mass-fraction carbon natural
    7014 -0.026000                     $ mass-fraction nitrogen-14
    8016 -0.761828                     $ mass-fraction oxygen-16
    nlib=.80c elib=.03e plib=.12p      $ newest libraries
MT2 lwtr.20t                           $ thermal treatment for hydrogen in light water
```

For the ^{157}Gd containing cell layer material the same material as used for the liquid was used with the correct mass fraction of ^{157}Gd depending on the experimental settings. The material card is given as follows:

```
M5
    1001  -<renormalised M2.1001>      $ mass-fraction hydrogen-1
    6000  -<renormalised M2.6000>      $ mass-fraction carbon natural
    7014  -<renormalised M2.7014>      $ mass-fraction nitrogen-14
    8016  -<renormalised M2.8016>      $ mass-fraction oxygen-16
    64157 -<fraction of Gd-157>        $ mass-fraction Gadolinium-157
    nlib=.80c elib=.03e plib=.12p      $ newest libraries
MT5 lwtr.20t                           $ thermal treatment for hydrogen in light water
```

For natural, non-enriched gadolinium, the contribution of the naturally occuring ^{155}Gd determines about 20% of the total energy deposition. Therefore the ^{155}Gd isotope is added as well. If natural composition is used than the ratio of both isotopes are 14.8% and 15.6% for ^{155}Gd and ^{157}Gd respectively. The remaining naturally occurring isotopes were not added as their cross sections where negligible. The material card is given as follows:

```
M6
    1001  -<renormalised M2.1001>      $ mass-fraction hydrogen-1
    6000  -<renormalised M2.6000>      $ mass-fraction carbon natural
    7014  -<renormalised M2.7014>      $ mass-fraction nitrogen-14
    8016  -<renormalised M2.8016>      $ mass-fraction oxygen-16
    64155 -<fraction of Gd-155>        $ mass-fraction Gadolinium-155
    64157 -<fraction of Gd-157>        $ mass-fraction Gadolinium-157
    nlib=.80c elib=.03e plib=.12p      $ newest libraries
MT6 lwtr.20t                           $ thermal treatment for hydrogen in light water
```

Additionally dummy materials are needed to specify isotopes later on. The material cards are given as follows:

```
M3   64155 1
M4   64157 1
```

C.3. Tallies

The used tallies were:

```
F16:p <cells separated by spaces> $ photon kerma
F26:e <cells separated by spaces> $ electron dose (from photons)
```

```
F46:n <cells separated by spaces> $ neutron kerma
F84:n <cells separated by spaces> $ energy-flux histogram
FM84 ((-1 4 102))                 $ conversion to Gd-157 capture rate
F94:n <cells separated by spaces> $ energy-flux histogram
FM94 ((-1 3 102))                 $ conversion to Gd-155 capture rate
```

The tally cells were thin slices, perpendicular to the incident beam. All tallies give energy in MeV per gram per source particle and were later converted into the dose rate per unit flux in Gy cm^2. Concentrations are reported in mass-ppm.

Bibliography

[1] Saleh M. Abbas and Andrew G. Hill. Prostatic sarcoma after treatment of rectal cancer. *World Journal of Surgical Oncology*, 5(1):82, Jul 2007. ISSN 1477-7819. doi: 10.1186/1477-7819-5-82. URL `https://doi.org/10.1186/1477-7819-5-82`.

[2] Gayane Abdullaeva, Gulnara Djuraeva, Andrey Kim, Yuriy Koblik, Gairatulla Kulabdullaev, Turdimukhammad Rakhmonov, and Shavkat Saytjanov. Evaluation of absorbed dose in gadolinium neutron capture therapy. *Open Physics*, 13(1), jan 2015. doi: 10.1515/phys-2015-0022.

[3] American Cancer Society. American Cancer Society. http://cancer.org, 2017. Accessed: 2017-12-12.

[4] Sangeeta Ray Banerjee, Ethel J. Ngen, Matthew W. Rotz, Samata Kakkad, Ala Lisok, Richard Pracitto, Mrudula Pullambhatla, Zhengping Chen, Tariq Shah, Dmitri Artemov, Thomas J. Meade, Zaver M. Bhujwalla, and Martin G. Pomper. Synthesis and evaluation of GdIII-based magnetic resonance contrast agents for molecular imaging of prostate-specific membrane antigen. *Angewandte Chemie International Edition*, 54(37):10778–10782, jul 2015. doi: 10.1002/anie.201503417.

[5] R. F. Barth. Boron neutron capture therapy of cancer: Current status and future prospects. *Clinical Cancer Research*, 11(11):3987–4002, jun 2005. doi: 10.1158/1078-0432.ccr-05-0035.

[6] Michael K Brawer. Update on the Treatment of Prostate Cancer: The Role of Adjuvant Hormonal Therapy. *Reviews in Urology*, 6:6–7, 2004.

[7] N. Cerullo, D. Bufalino, and G. Daquino. Progress in the use of gadolinium for NCT. *Applied Radiation and Isotopes*, 67(7-8):S157–S160, jul 2009. doi: 10.1016/j.apradiso.2009.03.109.

[8] Detlef Gabel, Katharina H. I. Philipp, Floyd J. Wheeler, René Huiskamp, and Rene Huiskamp. The compound factor of the 10 b(n,α) 7 li reaction from borocaptate sodium and the relative biological effectiveness of recoil protons for induction of brain damage in boron neutron capture therapy. *Radiation Research*, 149(4):378, apr 1998. doi: 10.2307/3579701.

[9] Giorgio Gandaglia, Alberto Briganti, Noel Clarke, R. Jeffrey Karnes, Markus Graefen, Piet Ost, Anthony Laurence Zietman, and Mack Roach. Adjuvant and salvage radiotherapy after radical prostatectomy in prostate cancer patients. *European Urology*, 72(5):689–709, nov 2017. doi: 10.1016/j.eururo.2017.01.039.

[10] A. Garretsen. Biological details of gdnct cell culture experiments [in conversation], 2018.

[11] Arundhati Ghosh and Warren D.W. Heston. Tumor target prostate specific membrane antigen (PSMA) and its regulation in prostate cancer. *Journal of Cellular Biochemistry*, 91(3):528–539, 2004. doi: 10.1002/jcb.10661.

[12] D. P. Gierga, J. C. Yanch, and R. E. Shefer. An investigation of the feasibility of gadolinium for neutron capture synovectomy. *Medical Physics*, 27(7):1685–1692, jul 2000. doi: 10.1118/1.599037.

[13] John Timothy Goorley. Boron Neutron Capture Therapy Treatment Planning Improvements. Master's thesis, 1998.

[14] John Timothy Goorley. *A Comparison of Three Gadolinium Based Approaches to Cancer Therapy*. PhD thesis, 2002.

[15] T. Goorley, M. James, T. Booth, F. Brown, J. Bull, L. J. Cox, J. Durkee, J. Elson, M. Fensin, R. A. Forster, J. Hendricks, H. G. Hughes, R. Johns, B. Kiedrowski, R. Martz, S. Mashnik, G. McKinney, D. Pelowitz, R. Prael, J. Sweezy, L. Waters, T. Wilcox, and T. Zukaitis. Initial MCNP6 release overview. *Nuclear Technology*, 180(3):298–315, dec 2012. doi: 10.13182/nt11-135. URL `https://doi.org/10.13182%2Fnt11-135`.

[16] Tim Goorley, Robert Zamenhof, and Hooshang Nikjoo. Calculated DNA damage from gadolinium auger electrons and relation to dose distributions in a head phantom. *International Journal of Radiation Biology*, 80(11-12):933–940, jan 2004. doi: 10.1080/09553000400017564.

[17] H. Grady III Hughes. Quick-start guide to low-energy photon/electron transport in MCNP6. Technical report, apr 2013. URL `https://doi.org/10.2172%2F1077005`.

[18] Esam M.A. Hussein. TRANSPORT. In *Radiation Mechanics*, pages 247–310. Elsevier, 2007. doi: 10.1016/b978-008045053-7/50005-7. URL `https://doi.org/10.1016%2Fb978-008045053-7%2F50005-7`.

[19] George A. Miller, Nolan E. Hertel, Bernard W. Wehring, and John L. Horton. Gadolinium neutron capture therapy. *Nuclear Technology*, 103(3):320–331, sep 1993. doi: 10.13182/nt93-a34855.

[20] V.N. Mitin, V.N. Kulakov, V.F. Khokhlov, I.N. Sheino, A.M. Arnopolskaya, N.G. Kozlovskaya, K.N. Zaitsev, and A.A. Portnov. Comparison of BNCT and GdNCT efficacy in treatment of canine cancer. *Applied Radiation and Isotopes*, 67(7-8):S299–S301, jul 2009. doi: 10.1016/j.apradiso.2009.03.067.

[21] Victor Alexander Nievaart. *Spectral Tailoring for Boron Neutron Capture Therapy.* PhD thesis, 2007.

[22] NRG. Neutron metrology results of hfr-hb5 neutron beam [mail contact], 2018.

[23] Koji Ono. An analysis of the structure of the compound biological effectiveness factor. *Journal of Radiation Research*, 57(S1):83 – 89, 2016. doi: 10.1093/jrr/rrw022.

[24] J. Plomp. Neutron spectrum delft [mail contact], 2018.

[25] Author Jean-pierre Pouget, Lore Santoro, Laure Raymond, Nicolas Chouin, Manuel Bardiès, Helena Huguet, David Azria, Pierre-olivier Kotzki, Monique Pèlegrin, Eric Vivès, Jean-pierre Pouget, Lore Santoro, Laure Raymond, Nicolas Chouin, Manuel Bardie, and Eric Vive. Cell Membrane is a More Sensitive Target than Cytoplasm to Dense Ionization Produced by Auger Electrons. *Radiation Research*, 170(2): 192—-200, 2008. doi: 10.1667/RR1359.1.

[26] Charles R. Pound. Natural history of progression after PSA elevation following radical prostatectomy. *JAMA*, 281(17):1591, may 1999. doi: 10.1001/jama.281.17.1591.

[27] V.M. Pusenkov, A. Schebetov, H.P.M. Gibcus, R.M. Gommers, F. Labohm, V.O. de Haan, and A.A. van Well. Numerical calculation of neutron fluxes at the exit of a complex neutron-guide system at IRI, delft. *Nuclear Instruments and Methods in Physics Research Section A: Accelerators, Spectrometers, Detectors and Associated Equipment*, 492(1-2):105–116, oct 2002. doi: 10.1016/s0168-9002(02)01292-5. URL `https://doi.org/10.1016%2Fs0168-9002%2802%2901292-5`.

[28] Hayley Reynolds, Scott Williams, Alan M. Zhang, Cheng Soon Ong, David Rawlinson, Rajib Chakravorty, Catherine Mitchell, and Annette Haworth. Cell density in prostate histopathology images as a measure of tumor distribution. 9041, 02 2014.

[29] C. Salt, A. J. Lennox, M. Takagaki, J. A. Maguire, and N. S. Hosmane. Boron and gadolinium neutron capture therapy. *Russian Chemical Bulletin*, 53(9):1871–1888, sep 2004. doi: 10.1007/s11172-005-0045-6.

[30] Rupert K Schmidt-ullrich. Molecular targets in radiation oncology. *Oncogene*, 22(37):5730–5733, 2003. doi: 10.1038/sj.onc.1206662.

[31] Jiri Stepanek. Emission spectra of gadolinium-158. *Medical Physics*, 30(1):41–43, dec 2002. doi: 10.1118/1.1528176.

[32] Hélio Yoriyaz, Maurício Moralles, Paulo de Tarso Dalledone Siqueira, Carla da Costa Guimarães, Felipe Belonsi Cintra, and Adimir dos Santos. Physical models, cross sections, and numerical approximations used in MCNP and GEANT4 monte carlo codes for photon and electron absorbed fraction calculation. *Medical Physics*, 36(11):5198–5213, oct 2009. doi: 10.1118/1.3242304. URL `https://doi.org/10.1118%2F1.3242304`.

[33] Ning J. Yue, Kent Lambert, Jay E. Reiff, Anthony E. Dragun, Ning J. Yue, Jay E. Reiff, Jean St. Germain, Susan M. Varnum, Marianne B. Sowa, William F. Morgan, Susan M. Varnum, Marianne B. Sowa, Grace J. Kim, William F. Morgan, James H. Brashears, Lydia T. Komarnicky-Kocher, Claudia Rübe, Anthony E. Dragun, Christin A. Knowlton, Michelle Kolton Mackay, Christin A. Knowlton, Michelle Kolton Mackay, James H. Brashears, Hedvig Hricak, Oguz Akin, Hebert Alberto Vargas, Darek Michalski, M. Saiful Huq, James H. Brashears, Brandon J. Fisher, James H. Brashears, Filip T. Troicki, Jaganmohan Poli, Mary Ellen Masterson-McGary, Luther W. Brady, Michael L. Wong, Edward J. Gracely, Edward J. Gracely, Daniel Yeung, Jatinder Palta, John P. Christodouleas, Yan Yu, Laura Doyle, Timothy Holmes, Claus Rödel, James H. Brashears, Carsten Nieder, Johannes A. Langendijk, George E. Laramore, Jay J. Liao, Jason K. Rockhill, Lydia T. Komarnicky-Kocher, Erik Limbergen, Stephan Mose, John P. Lamond, Brandon J. Fisher, Larry C. Daugherty, Robert H. Sagerman, Caspian Oliai, Mary Ellen Masterson-McGary, Brandon J. Fisher, and Larry C. Daugherty. Relative biological effectiveness (RBE). In *Encyclopedia of Radiation Oncology*, pages 748–748. Springer Berlin Heidelberg, 2013. doi: 10.1007/978-3-540-85516-3_584.

Feasibility of Gd-PSMA Neutron Capture Therapy for post treatment prostate cancer: A literature study

Diederik Feilzer[1,*]

[1]MSc. BME Student, TU Delft, The Netherlands
[*]diederikfeilzer@gmail.com

ABSTRACT

Purpose: The recurrence of prostate cancer after initial radiotherapy or surgery is high. The use of adjuvant therapy, an additional treatment performed before any evidence of failure of the first treatment, could reduce recurrence. Recently, a highly selective prostate tumor searching Magnetic Resonance Imaging (MRI) contrast agent containing Gadolinium (Gd) was created. The compound targets the Prostate Specific Membrane Antigen (PSMA) as found on prostate tumors and metastasis. Since even natural occurring Gd has a very high affinity for capturing neutrons, the Gadolinium PSMA (Gd-PSMA) contrast agent is here considered as a potential neutron capture agent for Neutron Capture Therapy (NCT) to be used as adjuvant or last-resort treatment for these previously treated patients.
Methods: Existing literature has been searched in various databases regarding the biological distribution (both macro- and microscopic) of Gd-PSMA (or similarly Gallium PSMA (Ga-PSMA) and Lutetium PSMA (Lu-PSMA)), the biological effects of the reaction products in Gadolinium NCT (GdNCT) (in vitro/silico) relative to their micro distribution; and the overall efficacy of GdNCT in various tumors and geometries. These results were combined to make predictions about the feasibility of the novel Gd-PSMA NCT about which no literature currently exists.
Results: Gd-PSMA NCT shows to be promising in its ability to spare organs at risk in vicinity of the tumor. Delivering sufficient thermal neutrons to a depth of 13-15 cm to reach the prostate while minimizing side effects could prove difficult compared to the shallower tumors more common in older applications of NCT. An expected advantage ratio of 1.9 to 5.6 is expected for larger bulk prostate tumors when irradiating from multiple directions while a significant improvement on that is expected for shallower and smaller metastasis. Assumed here is a compound corrected relative biological effectiveness (RBE) weighting factor (or Compound Biological Effectiveness (CBE)) of 1 to 5 for the electrons created in the Gd neutron capture reaction. Delivery of uniform dose profiles in larger bulk tumors is difficult. This is due to the self-shielding effects where outer tumor shell captures most of the neutrons before arriving in the center and the inability of precise aiming of the beam due thermal scattering.

1 Introduction

1.1 Introduction to Radiotherapy

In radiotherapy (RT), ionizing radiation is used to damage and kill malignant cells (i.e., tumor cells), thereby suppressing overall tumor growth. An important target for the ionizing radiation herein is the DNA. In radiotherapy the radiation is conformed to tumor cells thereby minimizing dose to healthy tissue preventing deterministic side effects and minimizing the possibility of stochastic late side effects such that the benefits outweigh the risk. The different RT approaches can be divided into two groups: external beam RT and internal RT.

In **external beam RT**, the radiation is generated outside the body and geometrically aimed towards the tumor. The radiation could be delivered in the form of photons, protons or even neutrons. At higher energies, all these beams can preserve their beam shape, some beam broadening aside, allowing them to be aimed towards the tumor. Photons are often used as they are the most easily generated, although protons are becoming a more promising choice of radiation. The added benefit of protons is that most of their energy is deposited at the end of their track. This results in a local peak, named the Bragg Peak, of higher dose which can be tuned with the beam energy. To make geometrically targeted RT treatments robust against alignment errors or patient movement, margins are often added to the irradiated area to assure full tumor coverage.

In **internal RT** the radiation can come from small surgically placed radioactive implants in or near the tumor as in brachytherapy; or from injected radioactive isotopes as in radioligand therapy (RLT). In RLT the radioisotopes can either be injected locally or intravenously. When this is done intravenously, the radioisotopes are often attached to molecules which

increase their uptake from the bloodstream in several specific tissue types such as the tumor. Whenever the placement of these isotopes is mitigated by such molecules we speak of chemical targeting. In chemical targeting a **tumor-selective** uptake is desired, i.e., the concentration associated with the tumor cells relative to the healthy cells should be preferably high. Chemical targeting is more robust against movement of the patient and other geometrical errors than external beam RT. It is also less dependent on knowing the location of the tumor cells while it is heavily dependent on the degree of the drug's selectivity towards the tumor cells.

1.2 Introduction to Neutron Capture Therapy

Neutron Capture Therapy (NCT) combines both RLT and external neutron beam therapy into one. Here the radioactive isotope as would be used in RLT is replaced with an agent that has a high affinity for capturing neutrons and consequently releasing the reaction energy locally. An external neutron beam delivers the complementary neutron flux at the position of the target volume. Just like in RLT, the neutron capture agent could be locally injected at the target volume[1] or chemically targeted to the tumor using a tumor-selective compound[2]. In addition to the aforementioned benefits of chemically targeted RT, the irradiation in chemically targeted NCT due to the neutron capture products is spatially confined to both the neutron irradiated area and the neutron capture agent containing/neighboring cells. Thus any undesired build up of the isotope in, for example, the kidneys or liver does not cause toxicity as long as they fall outside the neutron beam. Additionally, the irradiation can be timed with the optimal biological distribution of the drug as supposed to RLT where irradiation happens from the injection time to a few effective half-lives after that.

1.3 Historical Neutron Capture Therapy

From the first mention of NCT in 1936 to the present day, the main isotope investigated as a potential neutron capture agent was Boron 10 (B-10) because of its high affinity for capturing thermal neutrons (3838 barn[3,4]) and its local energy deposition due to the short range reaction products[5,6]. The main difficulty in Boron NCT (BNCT) clinical trials was the absence of any B-10 containing drugs that showed both low toxicity and high tumor-selective uptake[6]. Without this tumor-selective uptake there was no advantage over regular neutron beam therapy. Eventually, two candidates were found that satisfied both conditions after which more clinical trials followed[6]. These trials mainly tried to asses the potential of BNCT in treating brain melanomas[6]. A down side of BNCT was the inability to monitor B-10 levels. Instead rules of thumb were necessary, relating the B-10 concentration in blood to the intratumoral concentration.

Gadolinium (Gd) was investigated, starting in the late 1980s[4], as an alternative neutron capture agent for NCT. Gadolinium-157 (Gd-157) was mainly considered due to its 66 times higher affinity for capturing neutrons of 255000 barn[4] compared to B-10. However, the consensus is that Gadolinium NCT (GdNCT) can only reach its full potential if there is a tumor specific drug that internalizes the Gd towards the DNA or other molecular targets to fully use the short-range high-energy particles produced[7–9].

1.4 Neutron interactions and dose deposition in tissue

The behavior of neutrons in the body is heavily dependent on their energy. Mostly high energetic neutrons will not undergo capture reactions until they have been slowed down enough. This process of slowing down neutrons is called moderation and occurs mostly by elastic neutron collisions with light weight nuclei, primarily hydrogen. Fast neutrons can also knock the proton out of hydrogen atoms, leaving only a single electron. About half the energy of the neutron is transferred to the proton[3]. This single reaction is responsible for about 90% of the local charged particle energy deposition, further denoted as **kerma**, in tissue due to neutrons between 600 eV and 3 MeV[10]. When neutrons have slowed down enough in their energy as they go deeper into the body, the neutron capture reactions become more likely. The ^{14}N(n, p)^{14}C neutron capture reaction contributes 96% of the thermal neutron kerma with its 620 keV short range protons[10]. The kerma value excludes the energy of photons produced directly in these reactions. Although the kerma of the ^{1}H(n, γ)^{2}H reaction is relatively low, it is the main contributor for the photon dose. This reaction produces 2.224 MeV photons which are deposited over a larger volume and could even leave the body[10]. The thermal neutron flux increases in the first 3 to 4 cm into the body as more high energy neutrons lower in energy[7]. But, since thermal neutrons are more likely to undergo reactions, the thermal flux lowers exponentially from that point on as they travel deeper into the body.

1.5 Biophysics of Neutron Capture Therapy with Boron and Gadolinium

In BNCT, the reaction that causes the most damage to the tumor is the ^{10}B(n, α)^{7}Li neutron capture reaction with high cross section of 3838 barn[3,4]. The recoil nucleus will emit a 0.48 MeV photon 96% of the time, leaving 0.84 MeV for the nucleus itself and 1.47 MeV for the alpha particle[3]. Here, the ranges are 9 μm and 5 μm respectively. Compared to a typical cell diameter of 10 μm, this means that only cells containing or neighboring the compound will receive dose from these particles. The biological effect of these particles that deposit a large amount of energy over a short distance is much larger than, for example, that of the photon also produced. This energy deposition over distance is referred to as Linear

Energy Transfer (LET). However, since the most damaging radiation does not exceed beyond $< 10 \mu m$, the success of this therapy method is highly depended on the availability of tumor specific drugs that preferably enables internalization of the compound within the cell.

For GdNCT the reaction responsible for tumor damage is the $^{157}Gd(n, \gamma)^{158^*}Gd$ reaction which has a 66 times higher cross section of 255000 barns[10] relative to the $^{10}B(n, \alpha)^7Li$ reaction in BNCT. Here, the resulting exited nucleus will emit prompt gammas ranging from 0.079 to 7.88 MeV averaging at 2.2 MeV[10]. For smaller geometries the gamma component in GdNCT will leave the body. In larger tumors the gammas can help to increase the tumor dose as tumor cells have more and more neighbors from which they can receive these gammas. The kerma component of the resulting $^{158^*}Gd$ decay consists of the high LET internal conversion electrons (45 to 66 keV[10–12]), the following high LET complex Auger electron cascade (5 to 9 keV in total[10, 11]) and many soft X-rays (10.7-38.4 keV in total[10, 11]). Due to the extreme short ranges of the Auger electrons in particular, it is important look at the micro distribution of these Auger sources since their biological effectiveness depends heavily on their distances to biological targets. The internal conversion electrons have a larger range, extending multiple cell layers, which could provide cross fire from Gd positioned outside the cell or in neighboring cells. These large differences in energies, LET and ranges of the particles produced in GdNCT makes it hard to estimate the level of cell damage that they produce.

Gd also has a high affinity for photon interactions and, for neutrons above 6 MeV, it can also undergo neutron capture reactions were α particles or protons are produced. These other reactions, however, have a very low Q-value and neutrons above 6 MeV will have many orders of magnitude lower flux, especially at deeper sites[5]. This makes these other reactions not of importance in the assessment of GdNCT.

1.6 Computational dosimetry in compound delivered radiation

To relate absorbed doses to tissue damage or hazard in the radiation safety field, many different types of correction factors are applied. The physical or absorbed dose is equal to the total amount of energy per unit mass. A particle that delivers much energy over an extremely short distance could induce more complicated cell damage which is more difficult to repair. This effect is usually taken into account by a radiation weighting factor, the relative biological effectiveness (RBE)[13]. This factor holds the relative biological damage capable from a particle compared to that of a photon. An absorbed dose corrected by this factor is called a (photon) equivalent dose[13]. To account for the differences in importance and radio sensitivity of different organs, tissue weighting factors could be applied giving the effective full body dose.

However, in RT the goals and situations are very different from the radiation safety field. In conventional RT, absorbed dose calculations are made on macro scale. This means that the energy deposition in any cell organelle sized region could be seen as being Poisson distributed, on average matching the dose on macro scale. Since molecular targets in similar cells have similar volumes and sensitivity, a direct correlation with macro scale effective dose and local cell damage exists. This does not hold when biological targeting compounds are used to deliver the radiation[14]. For example, a 20 nm range electron from a compound bound to the cellular membrane will never cause a direct hit to DNA while a DNA incorporated compound could. This illustrates that similar doses on macro scale could yield very different results on a cellular scale.

Tissue weighting factors, used in radiation safety and conventional RT are defined on a macro scale (skin, liver, heart) since the doses are often smoothly distributed on this scale. To account for the much more inhomogeneous distribution of the energy deposition as found in compound delivered radiation, these factors would have to be defined on a much smaller scale. To derive such factors about the radio sensitivity of the different organelles in the cell is quite difficult as a lot of research is still going on into which molecular targets are more sensitive to radiation[15, 16]. In addition, the relative concentrations of these compounds at all different organelles must be known which is often not the case. A more practical way to account for these effects is to define a new factor that relates the absorbed dose on macro scale directly to the effective cell dose on macro scale. Such a factor is the Compound Biological Effectiveness (CBE) factor[14, 17]. This factor can be determined experimentally for each type of cell without knowing the exact micro distribution or radio sensitivity of all organelles. A group of cells could be given a known amount of the compound. Then absorbed dose calculations on macro scale can be made. On that scale the absorbed dose is independent of micro distribution effects. The observed outcome, like cell death, is then related to the same measure in a photon irradiated control with an absorbed dose such that the outcomes are equal. The factor that scales the absorbed compound dose to the equivalent absorbed photon dose is the CBE. The resulting CBE can then convert an absorbed dose on macro scale to the effective dose on macro scale, omitting the difficult to handle cell-scale. The CBE could also be calculated from cell scale simulations. For that, a biological distribution of the radiation sources need to be defined and the damage to different biological targets needs to be kept track of. This damage can be due to direct hits or chemical interactions with radicals produced by the radiation source. As the exact importance of biological targets in oncology is still not concise[15, 16], the quality of these simulation results is difficult to asses.

For the two main BNCT drugs, these CBEs have been measured[5, 17, 18]. Since the compound behaves differently in blood than in tumor cells, these two each have their own CBE[5, 17].

1.7 Prostate targeting Gadolinium delivery agent (Gd-PSMA)

Gd is traditionally used as a contrast agent in Magnetic Resonance Imaging (MRI)[2]. Here the actual injected ion, Gd^{3+}, can be toxic. The ion is therefore shielded from the body by wrapping it in other molecules covering the ion and inhibiting it from causing damage. An example of a Gd^{3+} holding MRI contrast agent often used in MRI named Gd-DTPA[19]. Another example of such a contrast agent is named Gd-DOTA of which many alterations exist[2].

Recently, such Gd-containing agents were bound to a ligand which has a high affinity for the Prostate Specific Membrane Antigen (PSMA) as presented on the membranes of prostate cells by Banerjee et al.[2]. PSMA is mostly presented on the cell membrane of active prostate cells and the expression of this antigen increases when the cell becomes malignant. Metastasis originated from the prostate will also be targeted by this new compound since they present PSMA as well. After binding to the PSMA on the membrane, the cell will engulf a significant fraction of the PSMA-targeting Gd-containing ligand and internalize[20]. Here most will move towards the vicinity of the nucleus[2,20]. Although, this development was not intended to be used as an NCT delivery agent, the tumor-selective uptake and the Gd contained in the compound make it an excellent candidate for a Gd delivery agent in NCT for the explicit purpose of treating prostate tumors. It is worth noting that no prior research named any PSMA targeting compound as a potential delivery agent of Gd in NCT. Neither did any research contain clinical or computational studies using any NCT in treating prostate cancer.

1.8 Conventional treatments for prostate cancer

Depending on the stage of the tumor development, several treatments are available. If the tumor is not thought to exceed the prostate then either surgery, Brachytherapy or external beam radiotherapy can be used. These treatments can in that case be curative although in many cases they are not[21]. If the tumor is suspected to have spread, hormone therapy is often used to suppress hormones that stimulate tumor growth, effectively shrinking the tumor. Hormone therapy is not curative and is often used as additional (**adjuvant**) therapy after other treatments or in combination with other treatments[22,23]. RT can also be used as additional or adjuvant therapy after an initial therapy. This extra round of radiation can help reduce recurrence at the cost of added risk of side effects to radiation[24]. Such adjuvant therapy can be prescribed before any signs of left behind tumor cells or it can be delayed until first signs of recurrence. The effect of such a delay however is unknown[24].

1.9 GdNCT as possible application to treat prostate cancer

Since the prostate cancers and metastasis present PSMA on their membranes proportional to their activity, PSMA targeting molecules could be very useful in delivering treatments to the cancerous cells. There is not yet a PSMA targeting Boron complex available, making BNCT not yet viable in treating prostate cancer. However, with the recent discovery of a PSMA targeting Gd containing molecule, it is possible to deliver Gd right to the cancerous cells, and potentially into the cells[2]. GdNCT is then possible to treat these types of cancer. As this is a novel approach, no literature is available on the matter. The remainder of this literature study will try to asses the efficacy and feasibility of using Gadolinium PSMA (Gd-PSMA) NCT as a possible adjuvant or secondary therapy using the literature on different aspects of GdNCT and PSMA.

2 Methods (and Materials) used to review literature

2.1 Literature search methods

To asses **the efficacy of Gd-PSMA NCT for post treatment prostate cancer patients** a literature study has been performed investigating all separate components of this novel method. Existing literature is gathered from various databases; including Scopus, Google Scholar, crossRef and MedPub. The topics of interest contained the following:

1. **Biological effectiveness of GdNCT reaction products relative to their micro distribution.** Both cell culture studies and cell scale simulations about the biological damage following gadolinium neutron captures at various positions in and around the cell have been accepted. Additionally, papers describing the effect of other similar auger emitters were also accepted.

2. **Expected biological distribution of Gd-PSMA** (or similarly Gallium PSMA (Ga-PSMA), Lutetium PSMA (Lu-PSMA)). Cell culture studies describing the micro distributions of the Gd at various times and cell lines have been accepted. Combined with the results from topic 1, the micro distribution should give insight into the biological effectiveness of Gd-PSMA NCT. Studies that describe the macro distributions and tumor-selectivity are included as well to be used in the assessment of the quantity of gadolinium deposited in organs at risk within regions of high neutron fluxes.

3. **Overall efficacy of GdNCT** in various tumors and larger geometries. Animal studies, phantom studies and computer studies for different geometries, tumor types and delivery mechanisms have been accepted. By adapting the results to

depths as those found in prostate cancers and metastases and the increased efficacy by using Gd-PSMA as a delivery agent, an estimation of the overall efficacy of Gd-PSMA NCT for prostate tumors can be made.

Results from these topics will be combined to make predictions about the efficacy and feasibility of the novel Gd-PSMA NCT about which no literature currently exists.

2.2 Literature comparing methods

The reported outcomes of the reviewed studies will be converted to a standard form where possible. This allows for the outcomes to be easily compared. In the case of cell culture studies reviewed in section 3.1.1, it is assumed that all cell cultures were irradiated with the same neutron spectrum, gamma contamination and geometry. Additionally, the cell cultures themselves are assumed to be similar in their sensitivity to irradiation. Reported outcomes will be converted to the effect of the irradiation with Gd relative to the effect in a control with out Gd for equal irradiation time, denoted as R. For a Gd concentration equal to zero this relative effect is assumed one ($R = 1$), i.e., no added effect compared to the control. If no self-shielding occurs, this is expected to rise linear with the Gd concentration, denoted as [Gd]. Therefore, the *added relative effect due to Gadolinium normalized for Gd concentration* (denoted as f) can be calculated from the reported outcomes. These assumptions translate to the model as described in equation 1 in which a physical lower bound is also included.

$$R = 1 + f \cdot [\text{Gd}] \geq 0 \tag{1}$$

Under these assumptions f is a constant number that could be fitted from outcomes as reported in the reviewed literature. A non-constant f, however, would indicate the falsehood of one or more of these assumptions. The human scale GdNCT simulations reviewed in section 3.3.2 can in some cases be compared by extrapolating the reported outcome from the various tumor depths to that of a typical prostate at 13 cm. This extrapolating is done by assuming the peak tissue dose to remain the same and to adjust the neutron capture dose with a flux depression factor. This flux depression factor is the relative thermal flux between the reported tumor depth and 13 cm. The factor is taken from the respective paper or, if flux profiles are not reported, from other papers.

3 Results

3.1 Biological effectiveness of GdNCT reaction products relative to their micro distribution

3.1.1 Cell culture studies with Gadolinium: Methods and Results of reviewed papers

Papers in this section all involve a cell suspension in a solution containing various amounts of a Gd in MRI contrast agents. Franken et al., Tokuuye et al. and Salt et al. have used the commercially available agent, Gd-DTPA, in their GdNCT cell culture studies. This agent is designed as an MRI contrast and is therefore not enriched in these studies beyond the 15.65% natural occurrence of Gd-157 although much higher concentrations of Gd-157 are commercially available[7]. In a suspension, Gd-DTPA will give very little internalization of Gd within the cell (five times lower concentration in- than outside the cells) and almost no internalization into the nucleus[4]. Of other Gd delivery agents used in Hofmann et al. (Gadobutrol) and Akine et al. (Gadopenetate), the micro distributions are less well known.

The model as specified in equation 1 is fitted to the GdNCT cell culture papers listed in this section. The individual values in terms of the fitted f are also reported in brackets as the publication year in parentheses. Calculated f-values compared to the concentration used in the experiment from these papers are also plotted in Figure 1.

Franken et al.[25] found the effect in "human SW-1573 cells (squamous cell lung carcinoma)" in a 393 ppm Gd-DTPA solution to be 2.3 times more effective than the same neutron fluence without the Gd. The Local Effects Model was fitted to the survival curve: $S = \exp(-\alpha D - \beta D^2)$. Here, the cell survival, S, is put in terms of the absorbed dose, D, and two fit parameters, α and β. No significant β was able to be calculated in both the control and Gd case. This means that the effect is close to log-linear on the surviving fraction plot and the relative enhancement factor, R, is constant in these dose ranges. [$f = 3.3 \cdot 10^{-3}$ ppm^{-1}] (2006)

Tokuuye et al.[26] found a 1.5 times higher cell killing effect in Chinese hamster cells suspended in an 800 ppm Gd-DTPA solution than with a solution of the B-10 holding drug, BSH, with equal molarity Boron to Gadolinium. Since here a non-zero β is fitted to the data in the Local Effects Model, the relative enhancement factor, R, is not constant over the whole dose range. When compared to the control, the relative effectiveness, R, varies around 5.7 ± 0.2. [$f = 5.9 \cdot 10^{-3} \pm 0.3 \cdot 10^{-3}$ ppm^{-1}] (2000)
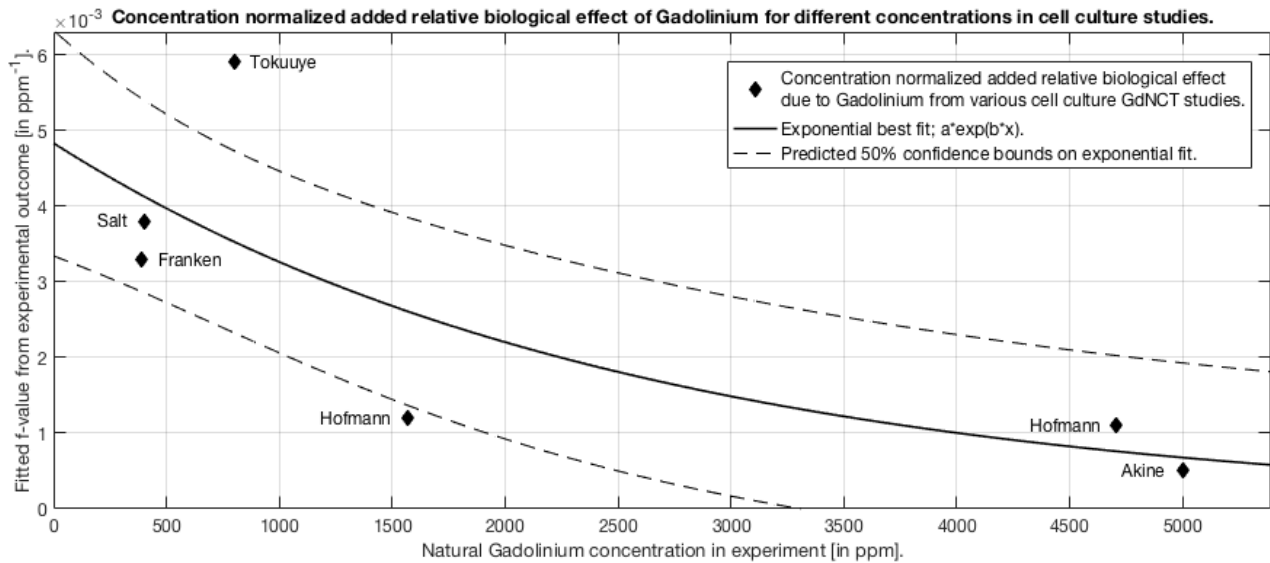
Figure 1. The concentration normalized added biological effect of Gadolinium on neutron irradiation. A clear trend is visible which is highlighted by the exponential fit with 50% confidence bounds. If however a linear fit is more appropriate, even negative f-values could become possible for high enough concentrations.

Salt et al.[4] found the effect in glioblastoma spheroid cell clusters suspended in a 400 ppm Gd-DTPA solution to be 2-3 times more effective than the same neutron flux without the Gadolinium. [$f = 3.8 \cdot 10^{-3} \pm 1.3 \cdot 10^{-3}$ ppm^{-1}] (2004)

Hofmann et al.[27] used a "melanoma cell line of human origin" (Sk-Mel-28) in a Gadobutrol suspension of 1570 ppm and 4710 ppm. A 0 ppm control gave 20% cell kill. In the gadolinium experiments, a 1570 ppm concentration gave 48% cell-kill, while three times that concentration gave 74% cell-kill compared to the controls without Gadobutrol. This converts to $R = 2.9$ for 1570 ppm and $R = 6.0$ for 4710 ppm. [$f = 1.2 \cdot 10^{-3}$ and $1.1 \cdot 10^{-3}$ ppm^{-1} respectively] (1998)

Akine et al.[28] showed that neutron irradiation of 5000 ppm natural Gd (Gadopenetate) containing Chinese hamster cells resulted in a 3.5 times lower irradiation time to reach 10% cell survival compared to without Gd. The 10% survival dose from x-ray irradiation was 9.1 Gy while only 1.9 Gy was necessary in GdNCT. It was suspected that this is mostly due to the electrons. The RBE of these electrons were reported to be unknown at that time. [$f = 0.5 \cdot 10^{-3}$ ppm^{-1}] (1992)

The large range in f-values support that the effects of Gd on neutron irradiated cells can vary by more than a factor of 5 in different cell lines, geometries, beam spectra, concentrations or Gd-compounds, even after normalizing for concentration. These were the assumptions under which f was presumed to be a constant in section 2.2. The strongest dependent variable seems the concentration of natural Gd used in the experiment (see Figure 1), most likely due to the self-shielding effect. From this its reasonable to assume that a monotonically decreasing function could capture this f-value dependency on the concentration. In Figure 1, an exponential function is fitted to the data which would drop to zero for higher concentrations, i.e., no added effect. This model, however does not allow negative f-values, i.e., negative added effect due to shielding of most neutrons. In theory such values are perfectly acceptable as long as the physical lower bound of $R = 0$ is satisfied (see Equation 1) which translates to $f \cdot [\text{Gd}] > -1$. Although, there is not yet enough data available to fit a more complicated model to the data.

The last study by Martin et al. does not involve cell cultures but is included in this "Cell culture" section. This because the experiment involved a biological model of the cell nucleus with using real DNA:

Martin et al.[8] used plasmid DNA suspended in a 393 ppm natural and enriched Gd containing solution as surrogate for a cell nucleus. They demonstrated that in low salt conditions, more Gd bonded to DNA which increased the DNA damage. This further demonstrates the effectiveness of the Auger electrons at short ranges. Additionally, enriching from 15.7% to 79.7% Gd-157 showed significant more cell kill. It was not mentioned whether this effect was proportional to the actual Gd-157 concentration. (1989)

3.1.2 Cell culture studies on Gd equivalent auger emitters: Methods and Results of reviewed papers

The electron spectrum from Iodine-125 (I-125) decay are thought to be similar to those of Gd-157 after neutron capture[29]. It could therefore be useful to understand the biological effect of these particles relative to their bio-distribution.

Howell et al.[30] reviewed literature for the radiobiological effectiveness of Auger emitters within various locations in the cell. Auger emitters located in the cytoplasms or outside the cell showed effects similar to low LET radiation of the same dose, this indicates a CBE factor around one. For auger emitters within the cell nucleus CBE values of 7-9 are reported. If the Auger emitter is incorporated in DNA the effects are stronger than that of intracellular alpha radiation which would mean a CBE of 20. (1993)

Balagurumoorthy et al.[31] show that the double stranded break (DSB) yield of a DNA incorporated I-125 decay decreases with distance to the DNA strand. Using various length molecules that bind the I-125 to DNA a relation between distance and DSB yield was made. A decay at 10.5 nm distance gives on average 0.52 ± 0.01 DSBs, all from direct hits to DNA. A decay at 12.0 nm lowers this to 0.24 ± 0.03 DSBs. Due to the range of the auger electrons, any decay at 13.9 nm results in 0.18 ± 0.02 DSBs caused by ·OH radicals. (2012)

Bishayee et al.[32] tested the effects of various DNA bound radioisotopes including I-125. The biological effects of DNA bound I-125 were found to be analogous to a CBE of 22 ± 2. (2000)

3.1.3 Cell scale computer simulation studies on the effect of GdNC: Methods and Results of reviewed papers

Electrons carry only about 0.6% of the total energy released in a ^{157}Gd(n,γ) reaction[29]. However, their high LET and local energy deposition makes their contribution to the overall biological effectiveness important. Several cell scale simulations were done to asses the biological damage of the ^{157}Gd(n,γ) reaction. Due to the short range of these electrons, all studies specified the micro distribution of the Gd.

Enger et al.[9] used nucleus dose as a measure of effect. They calculated, using a simple spherical cell model, that the electron dose to the cell nucleus drops from $8.88 \cdot 10^{-3}$ to $4.04 \cdot 10^{-4}$ Gy per ^{157}Gd(n,γ) reaction with all Gd in the nucleus and all Gd in the cytoplasm respectively. These doses exclude cross fire from other cells with Gd nor are any other secondary effects such as radical production accounted for. (2013)

Cerullo et al.[7] calculated the RBE of the electrons created in ^{157}Gd(n,γ) reactions according to ICRU 40 standards. Using a simple cylindric DNA model of 3 nm radius and the PENELOPE software package they found that the RBE varies with location relative to the DNA-cylinder from 12.6 at the center of the cylinder to 1.46 when just in the proximity of the DNA. However, only direct hits were taken into account while beyond the range of the Auger electrons, more damage could occur by radicals diffusing to, and reacting with DNA. The here reported RBE factors are compound specific, and can therefore be used as CBE factors under the distribution assumptions made in this paper. (2009)

Goorley et al.[29] calculated the number of DSB and single stranded break (SSB) from a ^{157}Gd(n,γ) reaction occurring within the cell nucleus using a more detailed model of DNA. Both direct hits and indirect hits from radicals diffusing into the DNA volume where counted for different types of radicals. An average within nucleus event reportedly resulted in 1.56 ± 0.16 SSBs and 0.21 ± 0.04 DSBs from an average source-target distance of about 40 nm. The DSB rate however matches more closely to the aforementioned results by Balagurumoorthy et al. at a distance of 12 nm. This affirms that although the average distance was 40 nm, mostly events closer to the DNA (< 12 nm) dominated the damage. (2004)

3.2 Expected biological distribution of Gd-PSMA

3.2.1 Papers on micro metabolic properties of PSMA targeted ligands

Banerjee et al.[2] were able to couple a PSMA targeting ligand to one, two and three Gd^{3+} containing MRI contrast agents, further denoted as Gd_{1-3}-PSMA. The compounds created by them formed the main reason for researching Gd-PSMA NCT. They showed that their Gd_3-PSMA molecule had 11 times higher uptake in PSMA presenting cells than non-presenting cells. Using fluorescent imaging, it is visible that the bulk of the internalized fraction is located in the vicinity of the nucleus (see Figure 2). After 24 hours most of the remains in the blood and bladder will have been excreted, while due to the internalization, the tumor concentrations have a much lower biological half life. (2015)

Ghosh et al.[20] describes the internalization process of PSMA bounded antibodies. The PSMA by itself has a tendency to be internalized spontaneously but this effect is enhanced by 200% following the binding of certain PSMA antibodies. The antibody induced internalization of the PSMA including the bounded molecule happens via clathrin coated
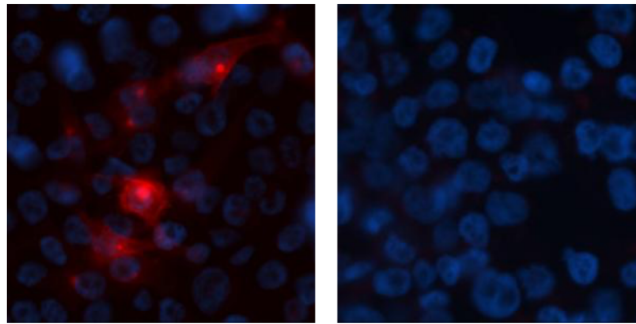
Figure 2. The PSMA targeting compound's biological distribution in a PC3 PIP cell line expressing PSMA (left) and non-PSMA expressing FLU cell line (right). In both 4 nM Gd_3-PSMA was present (equivalent to 12 nM Gd). The Gd_3-PSMA, stained with Rhodamine fluorescence is seen here in red while cells, stained with DAPI are seen here in blue. Note: the focal plane extends a few cell layers. Image taken from Banerjee et al.[2].

pits after which the PSMA can end up in lysosomes through late endosomes or pass through the recycling endosomal compartment which is in the vicinity of the nuclear membrane. It is presumed that the ligands used in Gd_{1-3}-PSMA from Banerjee et al.[2] are capable of inducing internalization as well. (2004)

3.2.2 In vivo imaging of different PSMA contrast agents

PSMA can be bounded to other atoms than Gd like Gallium-68 (Ga-68) and Lutetium-177 (Lu-177). In most papers reviewed in this section Ga-68 bounded PSMA is used in Positron-emission Tomography (PET) and Computed Tomography (CT) to visually inspect the distribution of PSMA in presenting cell clusters. A possible follow up treatment could be RLT. Here, the radioisotope Lu-177 bounded PSMA can be used, which in theory should target the same regions as was visible in the pre-treatment images. This therapy using Lu-177 is as of recently also available in the Netherlands at the University Medical Center of Utrecht. To asses the potential biological distribution of Gd-PSMA, the higher quality PET/CT images are used. Here Ga-68 bounded PSMA is viewed as a surrogate to Gd-PSMA. In addition to reviewing the papers for relevant quantitative data, some images from the reviewed papers are also put in this review (see Figure 3). Differences in the specific molecules used to bind these isotopes to the tracer could yield some difference in the biological distribution. This effect is assumed to be small here. Most neutron flux is expected in the lower abdomen, therefore the literature overview is narrowed to that region.
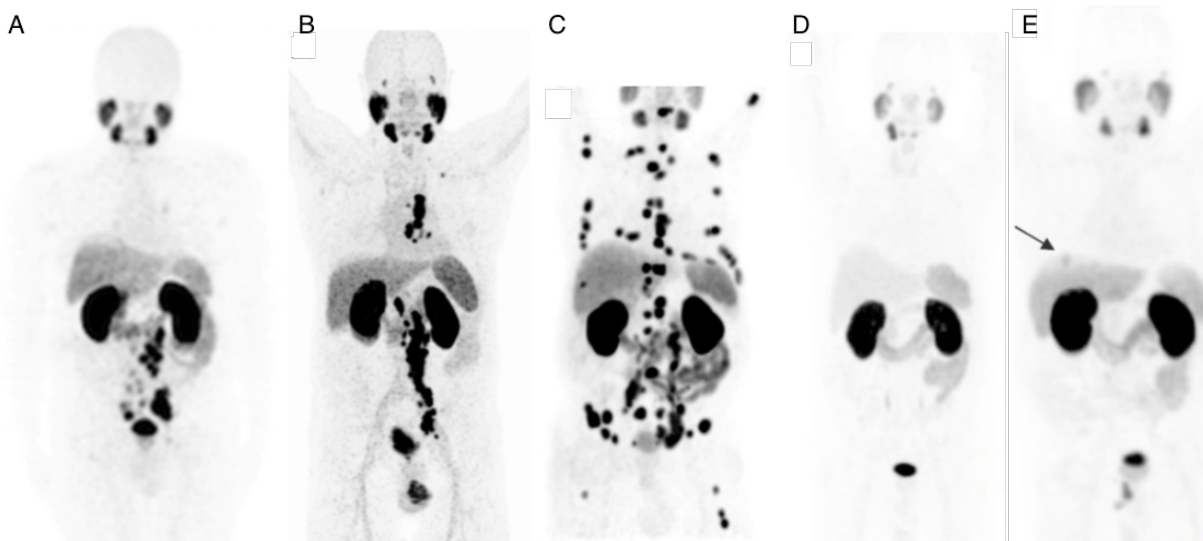

Figure 3. Aligned PET/CT images of prostate cancer patients injected with Ga-68 bounded to a PSMA targeting compound. Image is composed from various cropped source images and aligned; A: Sathekge et al.[33], B-C: Baum et al.[34], D-E: Prasad et al.[35]

Prasad et al.[35] quantitatively investigated the uptake of Ga-68-PSMA-HBED-CC in patients groups with various stages of prostate cancer. Results were reported in median Standardized Uptake Values (SUVs) 50 minutes after injection. Here, SUV is the activity per volume (in a small region of interest) relative to the injected activity per whole body volume. The size of the patient group for each cancer stage for which the average score is reported is denoted by n. Highest peak uptake of the tracer was found in the kidneys, 49.6 (n=101). Second highest non-tumor peak uptake in the abdomen was in the duodenum 13.8 (n=101). For different tumors median values of peak SUV were found to be: primary tumor (n = 35), 10.2; locally recurrent prostate cancer (n = 8), 5.9; lymph node (n=166), 6.2; bone (n=157), 7.4; other metastases (n=3), 3.8. In Figure 3 D and E, images from two patients of this paper are shown. (2016)

Kulkarni et al.[36] reported the kinetics of Lu-PSMA among a group of patients. Unfortunately, for each organ or lesion type, the data was specified as percentage of injected activity in that organ as supposed to concentration. What was included, however, were the absorbed doses during irradiation for two different Lu-PSMA compounds: Whole body, 0.03 and 0.04 mGy/MBq; Kidneys, 0.9 and 0.8 mGy/MBq; Bone lesions, 4.3 and 2.9 mGy/MBq; Lymph node lesions, 7.5 and 5.9 mGy/MBq. Note: These absorbed doses from radio ligand therapy are from injection to excretion where NCT can time irradiation with optimal biological distribution, hopefully arriving at better ratios. (2016)

Baum et al.[34] also reported kinetics of Lu-PSMA among a group of patients as percentage of injected activity. Here too the absorbed dose per organ was given: Whole body, $\sim$0 mGy/MBq; Kidneys, 0.8 mGy/MBq; Bone lesions, 3 mGy/MBq; Lymph node lesions, 4 mGy/MBq. The results match quite well with those of Kulkarni et al. in this section. (2016)

Fendler et al.[37] did not include quantitative details about biological distribution in humans as it was not their primary objective. However, two Lu-PSMA images, 18 and 24 hours after injection, still show uptake in the patient's kidneys while no other organs at risk seem to have an uptake comparable to the prostate and metastasis (From Figures similar to those in Figure 3). (2017)

Sathekge et al.[33] did not include quantitative details about biological distribution in humans either. However, the biological distribution of Bi-213-PSMA-617 was imaged showing higher uptake in the patient's kidneys, prostate and metastasis compared to the rest of lower abdomen, see Figure 3 A. (2017)

3.3 Overall efficacy of Gd Neutron Capture Therapy

Much of tumor damage originates from the actual particles produced in the neutron capture reaction with Gd-157. The neutron energies for which these captures are likely to happen are in the thermal to epithermal range. However, along the path traversed in the body before arriving at the tumor neutrons undergo moderation. This is the lowering of energy due to particle interactions in the tissue. Thus, deeper tumors need higher incident energies to achieve the same neutron spectrum at the tumor location. This could increase unwanted background dose to healthy tissue. To asses the doses in healthy tissue compared to those in the tumors it is therefore important to not only look at the cell level but to consider the whole irradiated geometry. The next papers consider these whole geometries in either animals, phantoms or computer simulations.

3.3.1 Animal GdNCT studies: Methods and Results of reviewed papers

The following studies were performed on groups of tumor bearing mice or dogs. Here standard non-enriched MRI contrast agents containing Gd were used.

Dewi et al.[38] studied mice with colon carcinoma tumors. Here the Gd containing MRI contrast agent Gadoteridol entrapped in liposomes was used. An improvement of the tumor to blood ratio over 24 hours was observed. However, both the non-injected control and the injected groups were irradiated for one hour starting at the 2 hour mark after injection, leaving only a 0.7 tumor to blood ratio. This time was chosen because it showed the highest absolute concentration in the tumor of 40 ppm. Two non-irradiated control groups were given either one or no injection. A third control group was irradiated without Gd. A four times lower growth was observed in the GdNCT group as supposed all three control groups demonstrating the additional effect of Gd on top of neutron irradiation. (2013)

Dewi et al.[39], in a second study, again used mice with colon carcinoma tumors. The agent used was the Gd-DPTA MRI contrast agent contained in nanoparticles. The agent was injected into the tail vain. No control group was used without Gd injections. Two groups received either a single injection or multiple injections at 10 hour intervals. A tumor to blood ratio of an average 2.4 was measured at the 24 hour mark for the single injection group. Uptake in the liver and spleen was significantly higher than in the tumor, even after 24 hours. At irradiation time (24 to 25th hour mark) a concentration of

8 ± 1 ppm Gd was measured in the tumor in the single injection group. The irradiated group of mice showed four times the tumor growth suppression compared to the non-irradiated control group. However, while the multiple injection group received a higher concentration, the difference in results were non significant. Since the study lacked a control group that underwent neutron irradiation without Gd, it is not known what the added benefit of the Gd was compared to neutron irradiation alone. (2015)

Hofmann et al.[27] showed that, in mice, intratumoral administration of 188 ppm Gadobutrol solution resulted in a homogeneously distributed Gd density on MRI images throughout the tumor. This remained even till after neutron irradiation was performed for 1 hour. The biological half-life was presumed equal to that of In-111-Butrol, 1 hour in general and up to 2.5 hours at injection site. The outcome was reported as the time to reach a certain tumor size in days after irradiation. The presence of Gd had a significant ($p < 0.01$) effect to the irradiation in delaying tumor growth time from 37 to 62 days. The irradiation itself without Gd present also showed delayed tumor growth ($p < 0.05$) compared to the non-irradiated controls, both with or without Gd. (1998)

Mitin et al.[1] showed that for 33 dogs, GdNCT using 10 ppm enriched intratumoral injected Gd-157 showed more self-shielding and higher normal tissue pigmentation than BNCT. However, since these were very shallow tumors, the geometry is not that different from that of mice. (2009)

3.3.2 GdNCT computer simulations: Methods and Results of reviewed papers

Many of the papers performed their macro dosimetry using Monte Carlo Computer Codes that perform coupled neutron and photon calculations, such as the MCNP4/5/6 and GEANT4 software packages. None of the papers transport electrons while this was possible in most of the software used at the time. The effect of this is that the dose due to photons is locally deposited at their interaction site instead of transporting the created electrons away. This transport of electrons could be seen as a smoothing operation on the dose matrix and ignoring that overestimates dose peaks. The complicated electron cascade following the $^{157}Gd(n,\gamma)^{158*}Gd$ reaction is not simulated properly in most popular codes and is therefore calculated via the neutron capture rate times a literature value for the kerma. For these types of neutron simulations it is important to account for that the thermal scattering of neutrons with hydrogen depends on the bond the hydrogen atom is in[40]. This behavior is already built in to MCNP and enabling it improves the accuracy of the simulations[9]. Tumors are of different sizes and loaded with different concentrations of Gd ranging from 30 to 1000 ppm Gd-157.

Enger et al.[9] used a real phantom with a shallow cylindrical tumor of 3 cm diameter, centered at 4.5 cm under the surface. By measuring the dose deposition using a foil and comparing it to simulations made in MCNP with the same geometry they confirmed the accuracy of the simulations. The thermal flux in the beam used in their simulations increased the first centimeters into the tissue via thermalization of faster neutrons and peaked at 3 cm and about halves every 2 cm beyond that peaking region. Several sized tumor centered at 4.5 cm depth were simulated with 2000 ppm natural Gd. The largest tumors showed 5 times higher dose than the background dose at that position with a lower dose at the far end of the tumor caused by shielding of neutrons at the near end. Extrapolating the thermal flux as function of depth displayed in the paper, the difference in thermal flux from this neutron source between a depth of 4.5 cm and 13 cm (typical prostate depth) is around a factor 16. This roughly decreases the neutron capture rate by a factor 16 as well for this particular beam. This would lower the advantage ratio to approximately 0.31. (2013)

Cerullo et al.[7] also found a negative effect of tumor depth on the advantage ratio in a bi-lateral beam setup. For a bulk tumor at 8 cm depth containing 700 ppm enriched Gd-157 and 10 ppm outside it the minimal tumor equivalent dose (absorbed dose adjusted with RBE factors) is 6 times higher than the peak equivalent tissue dose. While the paper focuses on tumor depths as found in head phantoms, the therapeutic ratio is calculated up to a tumor depth of 19 cm for small tumors using a mono lateral beam. From here it is evident that the therapeutic ratio at 13 cm is 9 times lower than at 8 cm in a mono lateral beam setup. After applying this factor 9, an estimation of the therapeutic ratio for a prostate tumor would be about 0.7 for a bi-lateral beam. A crude estimation of the therapeutic ratio for a single beam would be half that, 0.35. This low value could be improved if no gadolinium outside the tumor is present such as is presumed in Gd-PSMA after 24 hours. It is however worth noting that here a quite optimistic CBE of 10 was used for all electrons originating from the Gd-157 neutron capture reactions in calculating the equivalent doses. (2009)

Goorley[29] showed that the self-shielding in a 2.56 cm radius tumor with 350 ppm enriched Gd-157 in a mono lateral beam is quit big. The minimum tumor equivalent dose was found to be almost 80% lower than the maximal tumor dose. For a 1 cm radius tumor 9 cm deep with 1000 ppm enriched Gd-157 the dose contributions were given in min-max pairs: Auger, 0.21-0.8 Gy; Internal Conversion, 2.3-8.8; Photon, 5.2-8.5 Gy; Thermal Neutrons, 0.073-0.72 Gy; Fast Neutrons,

0.045-0.083; totaling to 7.82-18.9 Gy tumor dose with a peak tissue dose of 10 Gy. Earlier thesis work of Goorley[41] showed that at this depth and concentration the neutron capture photons form the majority of the photon dose. If we apply the flux depression as reported earlier[7] to these results we would expect a drop in tumor dose from 7.82-18.9 Gray to 0.87-2.1 Gy, giving an expected peak tumor to peak tissue equivalent dose ratio of 0.2 for a single beam. However a therapeutic ratio will be lower than that due to the large self-shielding behind the peak tumor dose. RBE values used were 2.5 for thermal neutrons and 1 elsewhere. (2004)

Gierga et al.[42] showed that for synovectomy BNCT performs better than GdNCT in both irradiation time and dose delivered to healthy tissue. Here the relative equivalent dose (RBE adjusted absorbed dose) contributions associated with 1000 ppm Gd-157 was: Auger + Internal Conversion, 39%; Photon, 52%; Thermal Neutrons, 3%; Fast Neutrons, 6%. Here an RBE of 3.8 is used for both neutron components and 1 elsewhere. (2000)

Miller et al.[12] was able to reach a tumor to peak normal tissue dose of 1.48 for a two bi-lateral epithermal neutron beams for an 8 cm deep tumor of 2 cm radius loaded with 100 ppm 80% enriched Gd-157. This ratio decreased to 1.33 for a smaller 1 cm radius tumor. Since here a tumor depth of of 8 cm is assumed as well, the same flux depression factor of 9[7] can be applied to estimate the therapeutic ratio for prostate cancer. This comes out to be 0.148 and 0.164 for a tumor of 1 and 2 cm respectively. (1993)

The estimations made in this section for the therapeutic ratio of prostate GdNCT using a single beam were 0.164[12], 0.31[9], 0.35[7] and <0.2[29]. The respective concentrations associated with these values were 100, 313, 700 and 1000 ppm equivalent enriched Gd. Although many aspect influence the effect, under 1000 ppm[29] the concentration seems to have a positive effect on the therapeutic ratio. That was already expected under the assumptions made in section 2.2. The decline of the added benefit of Gd for higher concentrations also agrees with the conclusion made in section 3.1.1. Whether the lower performance of the GdNCT in Goorley's[29] results were due to the extra high self-shielding or other aspects is unknown. It does indicate that for large tumors 1000 ppm might not be optimal.

4 Discussion and Conclusion

4.1 CBE factor of electrons from extra cellular Gd neutron capture.

Two computational papers[29,42] gave the dose contributions for a 1000 ppm enriched Gd concentration which compares to about 6400 ppm natural Gd. From all the cell culture studies, two[27,28] were performed with concentrations above 4000 ppm natural Gd. Due to the possible self-shielding, these two studies have the lowest f values. Extrapolating the trend in Figure 1 to 6400 ppm gives us an expected f-value of $-0.5 \cdot 10^{-3}$ to $1.5 \cdot 10^{-3}$ ppm^{-1}. From that we would expect that 1000 ppm enriched extracellular Gd-157 would locally enhance the effective dose by a factor 0 to 10. This only holds for tumor sizes similar to that of the Gd-containing volumes used to determine these f-values in section 3.1.1. For larger tumors, self-shielding effects could exceed that as found in papers reviewed in section 3.1.1 while the gamma component could increase by the build-up effect. If we use an RBE of 1.9 for these electrons and apply them and other RBEs to the dose contribution as given by Goorley[29] we can see this maximal factor of 10 in the equivalent dose. This gives us a range of 1 to 1.9 for the CBE factor of extra cellular Gd (since f-values were based on extra cellular concentrations). Other estimations have been made for the CBE for Gd. Goorley's thesis gives 5 as an upper bound to this value[41]. But improvement is expected for the CBE when the Gd actually internalizes like Gd-PSMA does.

4.2 CBE factor of the electrons from Gd-PSMA neutron capture.

From the biological micro distributions of Gd-PSMA we see that a significant fraction is internalized into the cell with the rest remaining in the vicinity of the cell membrane (see Figure 2). No Gd is transported into the cell nucleus. From Howell et al.[30], it seems that this micro distribution would not enable the full potential of the Auger electrons and a CBE of 1 is most suited for such electrons outside the nucleus. This factor then effectively incorporates an RBE of 1, tissue weighting factors and the sensitivity of different organelles weighted by the local relative Gd concentration. However, the distribution of Gd-PSMA is not uniform in the cytoplasms. More Gd is on the outer cellular membrane and in the vicinity of the nuclear membrane which form better targets than the cytoplasm[15,16]. This effectively makes the cell more sensitive to the same equivalent dose: i.e., the CBE for electrons from Gd-PSMA neutron captures is likely to be higher than 1. Future experiments will have to verify this. The best estimation for an upper bound on this CBE value is the most optimistic CBE like value used in papers reviewed here. This was a value of nearly 10, by Cerullo et. al.[7] derived in a cell scale simulation. The accuracy of cell scale computational studies is hard to asses due to the many assumptions made about the molecular targets. Unfortunately, none of the cell scale studies showed the effect of high concentrations near cellular membranes of

either Gd or other Auger emitters. These results are however still included in this literature review as new drugs could potentially get the Gd towards the DNA, in which case these papers do become relevant.

4.3 Therapeutic ratio of GdNCT for prostate tumors

From the estimations made in section 3.3.2 for the therapeutic ratio of prostate GdNCT using a single beam, it was visible that this depended positively on the concentration used up till a certain point. However, at the moment it is unknown what the maximal practical achievable concentrations of Gd-157 are in the Gd-PSMA form. When optimization and treatment planning is performed we can assume that the optimal reported therapeutic ratio of 0.31[9] should be achievable. This does not yet include the potential added effectiveness of internalized Gd as in Gd-PSMA and therefore should improve when the correct CBE factors are applied.

Cerullo et al.[7], although using an extremely high RBE, found that a bilateral beam delivers a better therapeutic ratio. Additionally, this should reduce the self-shielding effect. It could therefore be that irradiating from 6 directions, such that peak tissue doses do not increase significantly, a therapeutic ratio of 1.9 ($= 6 \cdot 0.31$) could be reached. About half the tumor dose is caused by electrons[29] an electron CBE of 5 could increase this ratio to 5.6. From the data available to me, using an upper bound on the electron CBE of 5[41] and a lower bound of 1[30], my best estimation for the therapeutic ratio of for bulk prostate tumors with 313 ppm Gd-157 using 6 beams is therefore 1.9 to 5.6. However, high self-shielding could proof providing a uniform dose to be difficult. For shallower, smaller metastasis the therapeutic ratio could potentially increase by quite a lot because of the higher flux[7,9] and lower diameter for self-shielding to occur along[29]. This method stands to gain most when future developments lead to internalization of the Gd into the nucleus of malignant cells.

5 Thesis Research plan

The thesis following this literature review will be part of a collaboration between NKI, NRG and TU Delft. My part in assessing whether Gd-PSMA NCT is a suitable treatment for prostate cancer will largely be computational. The project can be divided into three parts: simulation on cell-culture Gd-PSMA NCT experiment; treatment planning for GdNCT (potentially incorporating a new better measured value for the CBE); and neutron source filtering to optimize dose profiles of GdNCT for depths up to 13-15 cm. These are explained in detail below:

Many cell culture studies have been performed in Gd-suspensions were internalization of Gd is assumed to be negligible. The consequence is that only the effect of extra cellular Gd neutron captures is observed while other research shows that PSMA does get internalized were it could do more damage. To asses this improvement, a cell culture study with Gd-PSMA will be performed by NKI on which I will perform simulations. Details about the experiment itself are not determined yet. For my part on the simulations, I will perform coupled neutron, photon and electron transport simulations in the geometry of the experimental setup. Special attention will be paid to the electrons produced in the neutron capture reaction with Gd and consequences of the violation of the charged particle equilibrium in the cell layer. The simulations will compute the dose contributions from each radiation type such that a CBE can be fitted to the data that best relates the absorbed dose to the observed biological effective dose for the electrons in the Gd-PSMA neutron capture reaction.

For the treatment planning part, macro scale dose calculations will be performed in MCNP for a lower abdomen phantom including the prostate and several other organs. These macro scale dose calculations will incorporate the CBE as found in the cell culture study. Eventually the project will move towards creating a treatment planning algorithm that chooses the energy spectrum and intensities of multiple neutron beam positions and orientations. After surgical prostatectomy, the main tumor is no longer present but cells just outside the operated area or in metastases could still be present. To account for different tumor distributions due to different primary treatments, multiple of these distributions will be simulated and treatment planning will be performed on each of them. A possible outcome could be that Gd-PSMA NCT is only viable for shallower lymph node metastases or the removal of the remaining outer shell after prostatectomy or primary irradiation, while treating large bulk tumors with GdNCT is not viable due to heavy self-shielding.

Neutron sources and its filters will be optimize to deliver the spectra as calculated in the treatment planning part. It might be the case that these two parts (treatment planning and filter optimization) can however not be solved separately like in photon or proton therapy. In that case, the treatment planning part and neutron filtering will be investigated in conjunction.

Further plans will be made depending on developments during the project.

Abbreviations

B-10

Boron 10. 2, 5

BNCT

Boron NCT. 2, 4, 10, 11

CBE

Compound Biological Effectiveness. 1, 3, 7, 10–12

CT

Computed Tomography. 8

DSB

double stranded break. 7

Ga-68

Gallium-68. 8

Ga-PSMA

Gallium PSMA. 1, 4

Gd

Gadolinium. 1–12

Gd-157

Gadolinium-157. 2, 5, 6, 9–12

Gd-PSMA

Gadolinium PSMA. 1, 4, 5, 7, 8, 10–12

GdNCT

Gadolinium NCT. 1–6, 9–12

I-125

Iodine-125. 7

LET

Linear Energy Transfer. 2, 3, 7

Lu-177

Lutetium-177. 8

Lu-PSMA

Lutetium PSMA. 1, 4, 9

MRI

Magnetic Resonance Imaging. 1, 4, 5, 7, 9, 10

NCT

Neutron Capture Therapy. 1, 2, 4, 5, 7, 9, 12, 13

PET

    Positron-emission Tomography. 8

PSMA

    Prostate Specific Membrane Antigen. 1, 4, 7, 8, 12, 13

RBE

    relative biological effectiveness. 1, 3, 6, 7, 10–12

RLT

    radioligand therapy. 1, 2, 8

RT

    radiotherapy. 1–4

SSB

    single stranded break. 7

SUV

    Standardized Uptake Value. 9

References

1. Mitin, V. *et al.* Comparison of BNCT and GdNCT efficacy in treatment of canine cancer. *Appl. Radiat. Isot.* **67**, S299–S301 (2009). DOI 10.1016/j.apradiso.2009.03.067.

2. Banerjee, S. R. *et al.* Synthesis and evaluation of GdIII-based magnetic resonance contrast agents for molecular imaging of prostate-specific membrane antigen. *Angewandte Chemie Int. Ed.* **54**, 10778–10782 (2015). DOI 10.1002/anie.201503417.

3. Nievaart, V. A. *Spectral Tailoring for Boron Neutron Capture Therapy*. Ph.D. thesis (2007).

4. Salt, C., Lennox, A. J., Takagaki, M., Maguire, J. A. & Hosmane, N. S. Boron and gadolinium neutron capture therapy. *Russ. Chem. Bull.* **53**, 1871–1888 (2004). DOI 10.1007/s11172-005-0045-6.

5. Goorley, J. T. *Boron Neutron Capture Therapy Treatment Planning Improvements*. Master's thesis (1998).

6. International Atomic Energy Agency IAEA. Current status of neutron capture therapy. *Vienna* **IAEA-TECDOC-1223** (2001).

7. Cerullo, N., Bufalino, D. & Daquino, G. Progress in the use of gadolinium for NCT. *Appl. Radiat. Isot.* **67**, S157–S160 (2009). DOI 10.1016/j.apradiso.2009.03.109.

8. Martin, R. F., d'Chunha, G., Pardee, M. & Allen, B. J. Induction of DNA double-strand breaks by 157Gd neutron capture. *Pigment. Cell Res.* **2**, 330–332 (1989). DOI 10.1111/j.1600-0749.1989.tb00213.x.

9. Enger, S. A., Giusti, V., Fortin, M.-A., Lundqvist, H. & af Rosenschöld, P. M. Dosimetry for gadolinium neutron capture therapy (GdNCT). *Radiat. Meas.* **59**, 233–240 (2013). DOI 10.1016/j.radmeas.2013.05.009.

10. Abdullaeva, G. *et al.* Evaluation of absorbed dose in gadolinium neutron capture therapy. *Open Phys.* **13** (2015). DOI 10.1515/phys-2015-0022.

11. Stepanek, J. Emission spectra of gadolinium-158. *Med. Phys.* **30**, 41–43 (2002). DOI 10.1118/1.1528176.

12. Miller, G. A., Hertel, N. E., Wehring, B. W. & Horton, J. L. Gadolinium neutron capture therapy. *Nucl. Technol.* **103**, 320–331 (1993). DOI 10.13182/nt93-a34855.

13. Yue, N. J. *et al.* Relative biological effectiveness (RBE). In *Encyclopedia of Radiation Oncology*, 748–748 (Springer Berlin Heidelberg, 2013). DOI 10.1007/978-3-540-85516-3_584.

14. Barth, R. F. Boron neutron capture therapy of cancer: Current status and future prospects. *Clin. Cancer Res.* **11**, 3987–4002 (2005). DOI 10.1158/1078-0432.ccr-05-0035.

15. Pouget, A. J.-p. *et al.* Cell Membrane is a More Sensitive Target than Cytoplasm to Dense Ionization Produced by Auger Electrons. *Radiat. Res.* **170**, 192—-200 (2008). DOI 10.1667/RR1359.1.

16. Schmidt-ullrich, R. K. Molecular targets in radiation oncology. *Oncogene* **22**, 5730–5733 (2003). DOI 10.1038/sj.onc.1206662.

17. Ono, K. An analysis of the structure of the compound biological effectiveness factor. *J. Radiat. Res.* **57**, 83 – 89 (2016). DOI 10.1093/jrr/rrw022.

18. Gabel, D., Philipp, K. H. I., Wheeler, F. J., Huiskamp, R. & Huiskamp, R. The compound factor of the 10 b(n,α) 7 li reaction from borocaptate sodium and the relative biological effectiveness of recoil protons for induction of brain damage in boron neutron capture therapy. *Radiat. Res.* **149**, 378 (1998). DOI 10.2307/3579701.

19. Stasio, G. D. *et al.* Are gadolinium contrast agents suitable for gadolinium neutron capture therapy? *Neurol. Res.* **27**, 387–398 (2005). DOI 10.1179/016164105x17206.

20. Ghosh, A. & Heston, W. D. Tumor target prostate specific membrane antigen (PSMA) and its regulation in prostate cancer. *J. Cell. Biochem.* **91**, 528–539 (2004). DOI 10.1002/jcb.10661.

21. Pound, C. R. Natural history of progression after PSA elevation following radical prostatectomy. *JAMA* **281**, 1591 (1999). DOI 10.1001/jama.281.17.1591.

22. Brawer, M. K. Update on the Treatment of Prostate Cancer: The Role of Adjuvant Hormonal Therapy. *Rev. Urol.* **6**, 6–7 (2004).

23. American Cancer Society. American Cancer Society. http://cancer.org (2017). Accessed: 2017-12-12.

24. Gandaglia, G. *et al.* Adjuvant and salvage radiotherapy after radical prostatectomy in prostate cancer patients. *Eur. Urol.* **72**, 689–709 (2017). DOI 10.1016/j.eururo.2017.01.039.

25. Franken, N. *et al.* Gadolinium enhances the sensitivity of SW-1573 cells for thermal neutron irradiation. *Oncol. Reports* (2006). DOI 10.3892/or.15.3.715.

26. Tokuuye, K. *et al.* Comparison of radiation effects of gadolinium and boron neutron capture reactions. *Strahlentherapie und Onkologie* **176**, 81–83 (2000). DOI 10.1007/pl00002332.

27. Hofmann, B., Fischer, C.-O., Lawaczeck, R., Platzek, J. & Semmler, W. Gadolinium neutron capture therapy (GdNCT) of melanoma cells and solid tumors with the magnetic resonance imaging contrast agent gadobutrol. *Investig. Radiol.* **34**, 126–133 (1999). DOI 10.1097/00004424-199902000-00005.

28. Akine, Y., Tokita, N., Matsumoto, T., Oyama, H. & Aizawa, O. Gadolinium-neutron capture reactions: A radiobiological assay. In *Progress in Neutron Capture Therapy for Cancer*, 361–363 (Springer US, 1992). DOI 10.1007/978-1-4615-3384-9_79.

29. Goorley, T., Zamenhof, R. & Nikjoo, H. Calculated DNA damage from gadolinium auger electrons and relation to dose distributions in a head phantom. *Int. J. Radiat. Biol.* **80**, 933–940 (2004). DOI 10.1080/09553000400017564.

30. Howell, R. W., Narra, V. R., Sastry, K. S. R. & Rao, D. V. On the equivalent dose for auger electron emitters. *Radiat. Res.* **134**, 71 (1993). DOI 10.2307/3578503.

31. Balagurumoorthy, P., Xu, X., Wang, K., Adelstein, S. J. & Kassis, A. I. Effect of distance between decaying125i and DNA on auger-electron induced double-strand break yield. *Int. J. Radiat. Biol.* **88**, 998–1008 (2012). DOI 10.3109/09553002.2012.706360.

32. Bishayee, A., Rao, D. V., Bouchet, L. G., Bolch, W. E. & Howell, R. W. Protection by DMSO against cell death caused by intracellularly localized iodine-125, iodine-131 and polonium-210. *Radiat. Res.* **153**, 416–427 (2000). DOI 0033-7587(2000)153[0416:PBDACD]2.0.CO;2.

33. Sathekge, M. *et al.* 213bi-PSMA-617 targeted alpha-radionuclide therapy in metastatic castration-resistant prostate cancer. *Eur. J. Nucl. Medicine Mol. Imaging* **44**, 1099–1100 (2017). DOI 10.1007/s00259-017-3657-9.

34. Baum, R. P. *et al.* 177lu-labeled prostate-specific membrane antigen radioligand therapy of metastatic castration-resistant prostate cancer: Safety and efficacy. *J. Nucl. Medicine* **57**, 1006–1013 (2016). DOI 10.2967/jnumed.115.168443.

35. Prasad, V. *et al.* Biodistribution of [68ga]PSMA-HBED-CC in patients with prostate cancer: Characterization of uptake in normal organs and tumour lesions. *Mol. Imaging Biol.* **18**, 428–436 (2016). DOI 10.1007/s11307-016-0945-x.

36. Kulkarni, H. R. *et al.* PSMA-based radioligand therapy for metastatic castration-resistant prostate cancer: The bad berka experience since 2013. *J. Nucl. Medicine* **57**, 97S–104S (2016). DOI 10.2967/jnumed.115.170167.

37. Fendler, W. P., Rahbar, K., Herrmann, K., Kratochwil, C. & Eiber, M. 177lu-PSMA radioligand therapy for prostate cancer. *J. Nucl. Medicine* **58**, 1196–1200 (2017). DOI 10.2967/jnumed.117.191023.

38. Dewi, N. *et al.* Tumor growth suppression by gadolinium-neutron capture therapy using gadolinium-entrapped liposome as gadolinium delivery agent. *Biomed. & Pharmacother.* **67**, 451–457 (2013). DOI 10.1016/j.biopha.2012.11.010.

39. Dewi, N. *et al.* In vivo evaluation of neutron capture therapy effectivity using calcium phosphate-based nanoparticles as Gd-DTPA delivery agent. *J. Cancer Res. Clin. Oncol.* **142**, 767–775 (2015). DOI 10.1007/s00432-015-2085-0.

40. Ramos, R., Gonçalves-Carralves, M. S. & Cantargi, F. Bioneutronics: Thermal scattering in organics tissues and its impact on BNCT dosimetry. *Appl. Radiat. Isot.* **104**, 55–59 (2015). DOI 10.1016/j.apradiso.2015.06.019.

41. Goorley, J. T. *A Comparison of Three Gadolinium Based Approaches to Cancer Therapy*. Ph.D. thesis (2002).

42. Gierga, D. P., Yanch, J. C. & Shefer, R. E. An investigation of the feasibility of gadolinium for neutron capture synovectomy. *Med. Phys.* **27**, 1685–1692 (2000). DOI 10.1118/1.599037.